View metadata, citation and similar papers at core.ac.uk

brought to you by CORE

provided by UNH Scholars' Repository

University of New Hampshire
University of New Hampshire Scholars' Repository

Doctoral Dissertations | Student Scholarship

Fall 2009

Hadron -hadron scattering in lattice quantum chromodynamics

Aaron M. Torok
University of New Hampshire, Durham

Follow this and additional works at: https://scholars.unh.edu/dissertation

Recommended Citation
Torok, Aaron M., "Hadron -hadron scattering in lattice quantum chromodynamics" (2009). *Doctoral Dissertations*. 506.
https://scholars.unh.edu/dissertation/506

This Dissertation is brought to you for free and open access by the Student Scholarship at University of New Hampshire Scholars' Repository. It has been accepted for inclusion in Doctoral Dissertations by an authorized administrator of University of New Hampshire Scholars' Repository. For more information, please contact nicole.hentz@unh.edu.

HADRON-HADRON SCATTERING IN LATTICE QUANTUM CHROMODYNAMICS

BY

AARON M. TOROK

B.S. Electrical Engineering, University of Connecticut (1994)

DISSERTATION

Submitted to the University of New Hampshire

in Partial Fulfillment of

the Requirements for the Degree of

Doctor of Philosophy

in

Physics

September, 2009

UMI Number: 3383329

INFORMATION TO USERS

The quality of this reproduction is dependent upon the quality of the copy submitted. Broken or indistinct print, colored or poor quality illustrations and photographs, print bleed-through, substandard margins, and improper alignment can adversely affect reproduction.
In the unlikely event that the author did not send a complete manuscript and there are missing pages, these will be noted. Also, if unauthorized copyright material had to be removed, a note will indicate the deletion.

UMI®

UMI Microform 3383329
Copyright 2009 by ProQuest LLC
All rights reserved. This microform edition is protected against unauthorized copying under Title 17, United States Code.

ProQuest LLC
789 East Eisenhower Parkway
P.O. Box 1346
Ann Arbor, MI 48106-1346

This dissertation has been examined and approved.

Thesis Director, Silas R. Beane

Associate Professor, Department of Physics

Per Berglund

Associate Professor, Department of Physics

John Calarco

Professor, Department of Physics

James Harper

Professor, Department of Physics

Maurik Holtrop

Associate Professor, Department of Physics

July 17, 2009

Date

DEDICATION

To Jenny, Otto, and Ava.

ACKNOWLEDGMENTS

Thanks to the NPLQCD collaboration, who are: Silas Beane, William Detmold, Tom Luu, Kostas Orginos, Assumpta Parreño, Martin Savage, and Andre Walker-Loud. This dissertation exists as a result of their work and efforts. Thanks to R. Edwards and B. Joo for help with the QDP++/Chroma programming environment [1] with which the calculations discussed here were performed. I gratefully acknowledge the computational time provided by NERSC, the Institute for Nuclear Theory, Centro Nacional de Supercomputación (Barcelona, Spain), Lawrence Livermore National Laboratory, and the National Science Foundation through Teragrid resources provided by the National Center for Supercomputing Applications and the Texas Advanced Computing Center. Computational support at Thomas Jefferson National Accelerator Facility and Fermi National Accelerator Laboratory was provided by the USQCD collaboration under *The Secret Life of a Quark*, a U.S. Department of Energy SciDAC project (`http://www.scidac.gov/physics/quarks.html`). Thanks also to the US DOE, the University of California, and Lawrence Livermore National Laboratory.

TABLE OF CONTENTS

DEDICATION iii

ACKNOWLEDGMENTS iv

LIST OF TABLES vii

LIST OF FIGURES ix

ABSTRACT xii

INTRODUCTION 1

1 THEORY 4

1.1 QCD 4

1.2 Lattice QCD 6

1.2.1 Lattice Gauge Action 6

1.2.2 Lattice Fermions 7

1.2.3 Mixed Action Tuning 10

1.2.4 Contractions 10

1.3 Chiral Perturbation Theory 11

1.3.1 The Chiral Symmetry-Breaking Scale 12

1.3.2 $SU(2)$ and $SU(3)$ χ-PT 13

1.4 Scattering 14

1.4.1 Scattering in Quantum Mechanics 14

1.4.2 Scattering in a Finite Volume 15

2 LATTICE CALCULATION METHODOLOGY **18**

2.1 Computational Details 18

2.1.1 Correlation Functions 19

2.2 Signal Extraction 20

2.2.1 Generalized Effective Functions 21

2.2.2 Digital Filters 21

2.2.3 Linear Combination of Correlators 25

2.2.4 Effective Mass Function as an Overdetermined System of Linear Equations 26

3 LATTICE RESULTS **28**

3.1 Calculation of the $I = 2$ $\pi^+\pi^+$ scattering length 28

3.2 Calculation of the $I = 1$ K^+K^+ Scattering Length 31

3.3 Calculation of Multi-Pion States 33

3.4 Meson Baryon Scattering 35

3.4.1 Overview 35

3.4.2 Meson-Baryon Scattering Processes 39

3.4.3 Finite-Volume Calculation of Scattering Amplitudes 40

3.4.4 Lattice Calculation and Data Analysis 40

3.4.5 The Mixed Channel 43

3.4.6 SU(3) HBχPT Extrapolation 47

3.4.7 SU(2) HBχPT Extrapolation 54

3.4.8 Discussion of Results 59

CONCLUSION **61**

LIST OF REFERENCES **63**

A EFFECTIVE PLOTS **69**

LIST OF TABLES

2.1 The parameters of the MILC gauge configurations and domain-wall propagators used in this work. The subscript l denotes light quark (up and down), and s denotes the strange quark. The superscript dwf denotes the bare-quark mass for the domain-wall fermion propagator calculation. The last column is the number of configurations times the number of sources per configuration. Ensembles (i)-(iv) have $L \sim 2.5$ fm and $b \sim 0.125$ fm; Ensemble (v) has $L \sim 3.5$ fm and $b \sim 0.125$ fm; Ensembles (vi),(vii) have $L \sim 2.5$ fm and $b \sim 0.09$ fm. 19

3.1 A compilation of the various calculations and predictions for the $I = 2$ $\pi\pi$ scattering length. The prediction made in the paper [2] is labeled NPLQCD (2007). Also included are the experimental value from Ref. [3] (E 865 (2003)), the previous determination by NPLQCD [4] (NPLQCD (2005)), two indirect lattice results from MILC [5, 6] (the stars on the MILC results indicate that these are not lattice calculations of the $I = 2$ $\pi\pi$ scattering length but rather a hybrid prediction which uses MILC's determination of various low-energy constants together with the Roy equations), and the Roy equation determination of Ref. [7] (CGL (2001)). 30

3.2 Particle content, isospin, and valence quark structure of the meson-baryon states calculated in this work. As is clear from the valence quark content, these meson-baryon states have no annihilation diagrams. 40

3.3 Lattice calculation results from the four coarse MILC ensembles which enter the analysis of the meson-baryon scattering lengths. The first uncertainty is statistical and the second uncertainty is systematic due to fitting. All quantities are in lattice units. 44

3.4 $SU(3)$ LECs fit from each process at NLO, and from $\pi^+\Sigma^+$, and $\pi^+\Xi^0$ at NNLO. The first uncertainty in parentheses is statistical, and the second is the statistical and systematic uncertainty added in quadrature. 51

3.5 $SU(3)$ extrapolated scattering lengths using the LECs from Table 3.4. The first uncertainty in parentheses is statistical, and the second is the statistical and systematic uncertainty added in quadrature. Note that the NLO (NNLO fit) column is using C_1, C_{01} from the NNLO fit to $\pi^+\Sigma^+$,$\pi^+\Xi^0$. 51

3.6 $SU(2)$ LECs fit from each process at NLO and at NNLO. The first uncertainty in parentheses is statistical, and the second is the statistical and systematic uncertainty added in quadrature. 56

3.7 $SU(2)$ extrapolated scattering lengths using the LECs from Table 3.6. The first uncertainty in parentheses is statistical, and the second is the statistical and systematic uncertainty added in quadrature. 56

3.8 $SU(2)$ LECs fit from each process at NLO and at NNLO. The first uncertainty in parentheses is statistical, and the second is the statistical and systematic uncertainty added in quadrature. 57

3.9 $SU(2)$ extrapolated scattering lengths using the LECs from Table 3.8. The first uncertainty in parentheses is statistical, and the second is the statistical and systematic uncertainty added in quadrature. 58

LIST OF FIGURES

1-1 pi-pi scattering Feynman diagram 12

1-2 The function $p \cot \delta$ of Eq. (1.45) for values of the regulation parameter, Λ. The shaded band is the value of $p \cot \delta$, or $1/a$, calculated with Eq. (1.48) . 17

2-1 Block diagram of the operations involved to generate correlators. 19

2-2 First-order, digitally low-pass filtered correlators for MILC Ensemble (*ii*) of Table 2.1, with a filter of the type described by Eq. (2.6). 23

2-3 The SS and SP effective mass plots for the pion of MILC Ensemble (*v*) of Table 2.1, and the SS (labeled as cosh in the figure) after applying Eq. (2.10). The backwards propagating state, $\sim \exp(m_\pi t)$ is eliminated. 24

3-1 $m_\pi \, a_{\pi\pi}^{I=2}$ vs. m_π / f_π (ovals) with statistical (dark bars) and systematic (light bars) uncertainties. Also shown are the experimental value from Ref. [3] (diamond) and the lowest quark mass result of the $n_f = 2$ dynamical calculation of CP-PACS [8] (square). The blue band corresponds to a weighted fit to the lightest three data points (fit B) using the one-loop MAχ-PT formula in Eq. (3.2) (the shaded region corresponds only to the statistical uncertainty). The red line is the tree-level χ-PT result. The experimental data is not used in the chiral extrapolation fits. 30

3-2 Bar chart of the various determinations of the $I = 2$ $\pi\pi$ scattering length tabulated in Table 3.1. The stars on the MILC results indicate that these are not lattice calculations of the $I = 2$ $\pi\pi$ scattering length but rather a hybrid prediction which uses MILC's determination of various low-energy constants together with the Roy equations. 31

3-3 $m_{K^+} a_{K^+K^+}$ versus m_{K^+}/f_{K^+}. The points with error-bars are the results of this lattice calculation (not extrapolated to the continuum) on both the coarse and (one) fine MILC lattices. The solid curve corresponds to the tree-level prediction of χ-PT, and the point denoted by a star and its associated uncertainty is the value extrapolated to the physical meson masses and to the continuum. The smaller uncertainty associated with each point is statistical, while the larger uncertainty is the statistical and fitting systematic combined in quadrature. 33

3-4 Effective $\Delta E_{\pi^+\Sigma^+}$ plot for coarse MILC ensemble (*ii*) from correlation functions $C^{(\mathrm{SS})}$, $C^{(\mathrm{SP})}$ and $C^{(\mathrm{SS})} - \alpha C^{(\mathrm{SP})}$. By taking the linear combination with α tuned to remove the first excited state, earlier time slices are gained for fitting. 45

3-5 Effective energy plots of the six meson-baryon processes shown in Table 3.2. The plots are from MILC ensemble (*ii*), $n_J = 2$, and the linear combination $C^{(\mathrm{SS})} - \alpha C^{(\mathrm{SP})}$ is plotted. The dashed line is the sum of the meson and baryon masses for each process, while the error bars represent the jackknife uncertainty. Note that the bE axis of (e) is a factor of two larger in span than the other plots to encompass the dashed line at $m_\pi + m_\Xi = 1.124$. . . 46

3-6 $p\cot\delta/m_\pi$ versus $\Delta E_{\phi B}/m_\pi$ for the five elastic scattering processes from coarse MILC ensemble (*ii*). The curve shown is $p\cot\delta/m_\pi$ for the case of $m_\phi = m_K$, and $m_B = m_p$. 47

3-7 Plots of Γ_{NLO} versus the Goldstone masses for the five meson-baryon processes. All lattice data is included. 52

3-8 Plots of Γ_{NLO} and Γ_{NNLO} versus the Goldstone masses. The line at $\Gamma = 1$ is the leading order curve, and dotted line is the physical meson mass. The innermost error bar is the statistical uncertainty and the outermost error bar is the statistical and systematic uncertainty added in quadrature. The inner and outer filled bands correspond to the statistical and systematic uncertainty, respectively, of the fits to the LECs at NLO and NNLO using $\pi^+\Sigma^+$, and $\pi^+\Xi^0$ *only*, for the SU(3) case. 53

3-9 Γ_{NLO}, Γ_{NNLO} plots for the $\pi^+\Sigma^+$, and $\pi^+\Xi^0$ processes versus the pion mass. The line at $\Gamma = 1$ is the leading order curve, and the dotted line is the physical pion mass. The innermost error bar is the statistical uncertainty and the outermost error bar is the statistical and systematic uncertainty added in quadrature. The inner and outer filled bands correspond to the statistical and systematic uncertainty, respectively, of the fits to the LECs at NLO and NNLO using $\pi^+\Sigma^+$, and $\pi^+\Xi^0$ for the SU(2) case. 55

3-10 The 68% (light) and 95% (dark) confidence interval error ellipses for fits for the $\pi^+\Sigma^+$ (left), and $\pi^+\Xi^0$ (right) processes using Eqs. (3.40) and (3.41). . 57

3-11 The 68% (light) and 95% (dark) confidence interval error ellipses for fits for the $\pi^+\Sigma^+$ (left), and $\pi^+\Xi^0$ (right) processes using Eqs. (3.47) and (3.48). . 58

3-12 $\overline{a}$ plots for the $\pi^+\Sigma^+$, and $\pi^+\Xi^0$ processes versus the pion mass. The diagonal line is the leading order curve, and the dotted line is the physical pion mass. The innermost error bar is the statistical uncertainty and the outermost error bar is the statistical and systematic uncertainty added in quadrature. The filled bands are the fits to the LECs in the SU(2) case at NNLO as in Eqs. (3.51), and (3.52). 59

A-1 Single particle effective mass plots for coarse MILC ensemble (*i*). Here, $n_J = 2$, and the linear combination $C^{(\mathrm{SS})} - \alpha C^{(\mathrm{SP})}$ is plotted. The inner shaded bands are the jackknife uncertainties of the fits to the effective masses, and the outer bands are the jackknife uncertainty and systematic uncertainty added in quadrature over the indicated window of time slices. 70

A-2 Meson-baryon effective energy difference plots for coarse MILC ensemble (*i*). Here, $n_J = 2$, and the linear combination $C^{(\mathrm{SS})} - \alpha C^{(\mathrm{SP})}$ is plotted. The inner shaded bands are the jackknife uncertainties of the fits to the effective energy differences, and the outer bands are the jackknife uncertainty and systematic uncertainty added in quadrature over the indicated window of time slices. . 71

A-3 Single particle effective mass plots for coarse MILC ensemble (*ii*). Here, $n_J = 2$, and the linear combination $C^{(\mathrm{SS})} - \alpha C^{(\mathrm{SP})}$ is plotted. The inner shaded bands are the jackknife uncertainties of the fits to the effective masses, and the outer bands are the jackknife uncertainty and systematic uncertainty added in quadrature over the indicated window of time slices. 72

A-4 Meson-baryon effective energy difference plots for coarse MILC ensemble (*ii*). Here, $n_J = 2$, and the linear combination $C^{(\mathrm{SS})} - \alpha C^{(\mathrm{SP})}$ is plotted. The inner shaded bands are the jackknife uncertainties of the fits to the effective energy differences, and the outer bands are the jackknife uncertainty and systematic uncertainty added in quadrature over the indicated window of time slices. . 73

A-5 Single particle effective mass plots for coarse MILC ensemble (*iii*). Here, $n_J = 2$, and the linear combination $C^{(\mathrm{SS})} - \alpha C^{(\mathrm{SP})}$ is plotted. The inner shaded bands are the jackknife uncertainties of the fits to the effective masses, and the outer bands are the jackknife uncertainty and systematic uncertainty added in quadrature over the indicated window of time slices. 74

A-6 Meson-baryon effective energy difference plots for coarse MILC ensemble (*iii*). Here, $n_J = 2$, and the linear combination $C^{(\mathrm{SS})} - \alpha C^{(\mathrm{SP})}$ is plotted. The inner shaded bands are the jackknife uncertainties of the fits to the effective energy differences, and the outer bands are the jackknife uncertainty and systematic uncertainty added in quadrature over the indicated window of time slices. . 75

A-7 Single particle effective mass plots for coarse MILC ensemble (*iv*). Here, $n_J = 2$, and the linear combination $C^{(\mathrm{SS})} - \alpha C^{(\mathrm{SP})}$ is plotted. The inner shaded bands are the jackknife uncertainties of the fits to the effective masses, and the outer bands are the jackknife uncertainty and systematic uncertainty added in quadrature over the indicated window of time slices. 76

A-8 Meson-baryon effective energy difference plots for coarse MILC ensemble (*iv*). Here, $n_J = 2$, and the linear combination $C^{(\mathrm{SS})} - \alpha C^{(\mathrm{SP})}$ is plotted. The inner shaded bands are the jackknife uncertainties of the fits to the effective energy differences, and the outer bands are the jackknife uncertainty and systematic uncertainty added in quadrature over the indicated window of time slices. . 77

ABSTRACT

HADRON-HADRON SCATTERING IN LATTICE QUANTUM CHROMODYNAMICS

by

Aaron M. Torok
University of New Hampshire, September, 2009

Hadron-hadron and multi-hadron scattering calculations in fully dynamical, mixed-action Lattice Quantum Chromodynamics using the MILC gauge ensembles in a non-perturbative simulation are discussed. In particular, calculations of the $\pi^+\Sigma^+$, $\pi^+\Xi^0$, K^+p, K^+n, and $\overline{K}^0\Xi^0$ scattering lengths are presented, and are the main subject of this dissertation. Using the two-flavor chiral expansion for extrapolation, the pion-hyperon scattering lengths are found to be $a_{\pi^+\Sigma^+} = -0.197 \pm 0.017$ fm, and $a_{\pi^+\Xi^0} = -0.098 \pm 0.017$ fm, where the comprehensive error includes statistical and systematic uncertainties. Meson-meson and multi-meson lattice calculations by the NPLQCD collaboration are reviewed, and presented for completeness.

INTRODUCTION

The Scattering Problem has been studied in many different contexts and spans several fields of physics. There is classical scattering, quantum mechanical scattering, and scattering of quantum fields. The subject of this dissertation is hadron-hadron scattering calculations in Lattice Quantum Chromodynamics (LQCD), and the objects considered are formally quantum fields.

Heuristically, scattering provides information about the potential in the classical and quantum mechanical cases, and in the case of quantum field theory, about the interaction of two or more quantum fields. This is one reason for the ubiquity of scattering in physics; it is a tool that yields the interaction between objects being studied, and in effect defines their interactions.

Experimentally, scattering studies are the main driving force behind all of the accelerator physics in the world. On the cutting edge are Jefferson National Laboratory (JLAB), Fermilab, as well as many others, and soon to come on-line, the single largest scientific endeavour in human history, the Large Hadron Collider (LHC). All of these programs are primarily focused on studying inelastic scattering, where the initial and final states of the particles being scattered are often very different. In the work presented here, elastic scattering of hadrons by other hadrons is considered, and the energies are lower as compared to most accelerator physics by many orders of magnitude. Naively, this low-energy problem would seem trivial, since at low energies the assumption might be that the problem becomes simpler, as relativistic effects would not be important, however, this is not necessarily the case.

The success of Quantum Electrodynamics (QED) in calculating quantities relevant to atomic physics to extremely high-precision is dependent on the Feynman path integral approach, and is a perturbative method. The coupling constant of QED that is raised to

the next integer power at each successive order in perturbation theory, is $\approx 1/137$, so a second order correction in QED is suppressed by a factor of $< 10^4$.

Quantum Chromodynamics (QCD) is also perturbative, but at energies $\gtrsim 1$ GeV. When the momentum transfer is large enough, the degrees of freedom are those that appear in the QCD Lagrangian, quarks and gluons. However, in the regime of energies $<< 1$ GeV, the observed degrees of freedom are the mesons and baryons, which are understood to be bound states of quarks, confined to a region $\sim$1 fm by the gauge fields of QCD, the gluons. The failure of perturbation theory at energies $<< \Lambda$, where $\Lambda \sim 1$ GeV, was the subject of the Nobel prize in physics in 2004, "for the discovery of asymptotic freedom in the theory of the strong interaction," by Gross, Politzer, and Wilczek. Ultimately, this is the motivation for using Lattice QCD to probe the regime of non-perturbative QCD.

Wilson invented LQCD [9] as a regularization scheme, to provide a non-perturbative cutoff for QCD. A minimum wavelength exists due to the lattice formulation through the lattice spacing, b, where there is a maximum momentum of $\sim \pi/b$ [10] that can propagate on the lattice. As a result of the lattice formulation, Feynman path integrals become well-defined ordinary integrals, and the convergence problems associated with perturbation theory are avoided in favor of the rigorous definition of the lattice field theory. Lattice gauge theory is particularly amenable to calculation with computers due to its discrete formulation, which seems serendipitous considering that both lattice gauge theory and digital computers have developed over approximately the same time period.

The use of largely parallel computing clusters and supercomputers has created explosive growth of LQCD. The evolution of the field of from the 1980s to the present is largely a result of the development of sophisticated optimization algorithms and machines. Many have doubted that Moore's law would have been predictive for so long, and with the multi-core architectures that are currently employed, it may continue still.

With regard to scattering in LQCD, there are theoretical underpinnings not associated with QCD itself. One is the formulation of the scattering problem in a Euclidean spacetime. The Maini-Testa theorem states that S-matrix elements cannot be calculated

from Euclidean space correlators at infinite volume, except at kinematic thresholds [11]. Lüscher's formulation of scattering in a finite volume, that relates an expansion in discrete modes in the box to the phase shifts circumvents this issue. Another theoretical challenge currently associated with LQCD is the issue of the connection of the calculations done at unphysically large pion (quark) masses to the physical point. These issues are addressed, and calculable using Chiral Perturbation Theory (χ-PT), the low energy effective theory of QCD, which is the theoretical tool that is utilized to use LQCD calculations to extract physical observables. Eventually, these issues may be moot, as calculations move toward the physical pion mass, however, they currently exist and hence, χ-PT is essentially coupled to LQCD. Additionally, there are specific formulations of χ-PT that address the finite volume, and finite lattice spacing effects, and quantify them in order to improve the accuracy and precision of LQCD extrapolations to the physical point.

In this dissertation, calculations of scattering observables for several systems of hadrons are discussed. Calculations that involve mesons exclusively have reached a high level of precision. Calculations with baryons are more challenging, and the calculation of meson-baryon scattering lengths represents an intermediate step toward nuclear physics calculations using LQCD. In this work, the $\pi^+\Sigma^+$, $\pi^+\Xi^0$, K^+n, K^+p, $\overline{K}^0\Sigma^+$, and $\overline{K}^0\Xi^0$systems are analyzed by calculating the masses and energies associated with these states in mixed-action LQCD using 4 sets of the coarse MILC gauge configurations [12]. Additionally, $\pi^+\pi^+$, K^+K^+, and multi-pion calculations are reviewed.

Chapter 1

THEORY

The theory of the strong interactions is QCD, and the low energy effective theory of QCD is χ-PT. Wilson created LQCD [9], and proved that it is a renormalizable gauge theory. Using LQCD and χ-PTtogether, one is able to extract physical observables, such as the masses and decay constants of the mesons. With the addition of Lüscher's method for calculating scattering states in a finite volume, scattering observables are calculable using LQCD, currently at unphysical values of the quark masses. Using χ-PT, extrapolation to the physical point is done ideally with the particular type of χ-PT that correctly accounts for lattice artifacts.

1.1 QCD

QCD is the theory of color $SU(3)$, meaning that it is an $SU(3)$ gauge theory, where the gauge fields, the gluons, carry color charge, and couple to the color charge in the quarks. Following Georgi [13], the quarks are composed of 3 colors

$$q = \begin{bmatrix} q_{\text{red}} \\ q_{\text{blue}} \\ q_{\text{green}} \end{bmatrix} . \tag{1.1}$$

There are 8 gluon fields, denoted $G_a^{\mu\nu}$. The QCD Lagrangian is

$$\mathcal{L} = -\frac{1}{4} G_a^{\mu\nu} G_{a\mu\nu} + \sum_{flavors} \left(i\bar{q} \not{D} / q - m_q \bar{q} q \right) , \tag{1.2}$$

$$D^\mu = \partial^\mu + igT_a G_a^{\mu\nu} \ , \qquad igT_a G_a^{\mu\nu} = [D^\mu, D^\nu] \ . \tag{1.3}$$

The T_a are the Gell-Mann matrices. They are Hermitian, and satisfy

$$\mathrm{Tr}[T_a T_b] = \frac{1}{2}\delta_{ab} \ . \tag{1.4}$$

The T_a are the color charges, and the quarks form two kinds of bound states, bound by exchange of the gluons; the mesons, and the baryons. Their structure is

$$\phi \rightarrow \overline{q}q \ , \qquad B \rightarrow \epsilon_{jkl} q_j q_k q_l \ , \tag{1.5}$$

where ϕ is a meson, and B is a baryon.

QCD is perturbative at momentum transfers, $Q > \Lambda_{QCD}$. As Q increases, the coupling constant decreases, and perturbation theory gets better. This is what is meant by Asymptotic Freedom: the quarks are not confined at energies $>> \Lambda_{QCD}$, and this is the perturbative regime. This is illustrated by the Beta function of QCD, and the running coupling constant [14]

$$\beta(g) = \mu \frac{\partial g}{\partial \mu} = \frac{g^3}{16\pi^2}\left[\frac{11}{3}N_c - \frac{2}{3}N_f\right] \ , \tag{1.6}$$

$$\frac{g^2(Q^2)}{4\pi} = \frac{4\pi}{(11N_c/3 - 2N_f/3)\log(Q^2/\Lambda_{QCD}^2)} \ . \tag{1.7}$$

Given that the strong coupling constant becomes larger at low energies, it is impossible to do perturbative calculations using the QCD degrees of freedom, quarks and gluons. According to Creutz, before the development of Lattice QCD, meson-nucleon field theory was failing due to the fact that the coupling constant analogous to $\alpha_{em} \approx 1/137$, was instead 15, and the so-called perturbative calculations were failing completely [10].

1.2 Lattice QCD

Kenneth Wilson invented Lattice QCD in 1974 [9]. His original approach and aim was to regularize QCD by introducing a finite cutoff for the maximum momentum that can propagate. Lattice QCD places the quarks at the points of a spacetime lattice, and the gluons occupy the links between lattice sites. With the introduction of this regularization method, the Feynman path integral for QCD becomes an ordinary integral, of very large dimension on the lattice [14].

Despite the fact that the lattice regularization renders the path integrals ordinary, and of finite-dimension, the scale of the numerical problem at hand lends itself to a statistical treatment. Therefore, Monte-Carlo methods are used in order to compute the integrals in question [10].

1.2.1 Lattice Gauge Action

The links between lattice sites are the gauge fields on the lattice. The lattice representation of the fundamental representation of $SU(3)$, is related to the vector potential, A_μ, through [14]

$$U_{x,\mu} = \exp(igaA^c_\mu \lambda^c/2) \ . \tag{1.8}$$

And the plaquette, a closed-loop is given by [14]

$$U_{x,\mu\nu} = \mathrm{Tr}(U_{x,\hat{\mu}} U_{x+\hat{\mu},\nu} U^\dagger_{x+\hat{\nu},\mu} U^\dagger_{x,\nu}) \ , \tag{1.9}$$

where the $\hat{\mu}$ is a unit vector in the μ-direction. The Wilson action is [14]

$$S_{G-SU(3)} = \frac{1}{g^2} \sum_x \sum_{\mu \neq \nu} (3 - \mathrm{Re} U_{x,\mu\nu}) \ . \tag{1.10}$$

Expanding $U_{x,\mu\nu}$, in Eq. (1.10), and taking the limit $b \to 0$, yields the continuum $SU(3)$ gauge action up to $\mathcal{O}(b^2)$ corrections [14]

$$S_{G-SU(3)} = \int_0^\beta d\tau \int d\mathbf{x} \frac{1}{4} (F^c_{\mu\nu})^2 + \mathcal{O}(b^2) \ , \tag{1.11}$$

where

$$F^c_{\mu\nu} = \partial_\mu A^c_\nu - \partial_\nu A^c_\mu - g f_{abc} A^a_\mu A^b_\nu \ . \tag{1.12}$$

1.2.2 Lattice Fermions

Fermions on the lattice present difficulties due to the fact that the derivative in the continuum becomes a finite difference on the lattice, and this leads to species doubling. Additionally, one of the most fundamental, and important properties of the free fermionic theory is chiral symmetry. Lattice fermions with chiral symmetry are essential for hadronic calculations because of the fundamental role chiral symmetry plays with regard to the existence of Goldstone bosons.

Staggered Fermions

There are several discretization schemes for lattice fermions, but in this work only staggered and domain-wall fermions will be discussed since they are used in the calculations. Naive fermions on the lattice result in 16-fold degeneracy as a result of the fact that the lattice propagator has a $\sin^2(bp_\mu)$ in the denominator, which renders contributions for $p_\mu = (0,0,0,0)$ equivalent to $p_\mu = (p_1, p_2, p_3, p_4)$, with any element of the 4-vector $p_\mu = \pi$. There are thus 2^4 combinations which correspond to 16 fermions [14].

One formulation that addresses this degeneracy, and is the formulation of the fermion action used in the calculations in this work is the staggered fermion formulation [15, 16, 17, 18]. The fermion fields are [12]

$$\psi(x) = \Gamma_x \chi(x) \quad , \ \bar{\psi}(x) = \bar{\chi}(x)\Gamma^\dagger_x \ , \tag{1.13}$$

with

$$\Gamma_x = \gamma_1^{(x_1/a)} \ \gamma_2^{(x_2/a)} \ \gamma_3^{(x_3/a)} \ \gamma_4^{(x_4/a)} \ . \tag{1.14}$$

Using $\Gamma^\dagger_x \Gamma_x = 1$ and

$$\Gamma^\dagger_x \gamma_\mu \Gamma_{x+a\mu} = (-1)^{(x_1+\cdots+x_{\mu-1})/a} \equiv \eta_\mu(x) \ , \tag{1.15}$$

the naive fermion action can be written as [12]

$$S_{KS} = \sum_x \bar{\chi}(x) \left\{ \sum_\mu \eta_\mu(x) \, \nabla_\mu \, \chi(x) + m\chi(x) \right\} \equiv \bar{\chi} \, (D_{KS} + m) \, \chi \, , \tag{1.16}$$

In the final expression matrix multiplication is implicit. It is possible to restrict the fermion field, $\chi(x)$, to a single component, reducing the original 16-fold degeneracy to four, where each $\chi(x)$ has four "tastes", which is a new and unwanted quantum number that can be removed by another method, that involves taking the fourth root of the fermion determinant [19, 20, 21, 22, 23, 24, 25, 26].

Domain Wall Fermions

For the valence sector, the five dimensional Shamir domain wall fermion action is used [27, 28, 29]

$$\begin{aligned} S_{DW} &= -\sum_{x,x'} \sum_{s=0}^{L_s-1} \left[\bar{\Psi}(x,s) \left[D_w(x,x') + 1 \right] \Psi(x',s) \right] - \\ &- \left[\bar{\Psi}(x,s) \frac{1-\gamma_5}{2} \Psi(x',s+1) + \bar{\Psi}(x,s) \frac{1+\gamma_5}{2} \Psi(x',s-1) \right] + \\ &+ m \left[\bar{\Psi}(x,0) \frac{1+\gamma_5}{2} \Psi(x',L_s-1) + \bar{\Psi}(x,L_s-1) \frac{1-\gamma_5}{2} \Psi(x',0) \right] \, , \end{aligned} \tag{1.17}$$

with $D_w(x,x')$ the regular four dimensional Wilson fermion action [29],

$$D_w(x,x') = (4+M_5)\delta_{x,x'} - \sum_\mu \left[\frac{1-\gamma_\mu}{2} U_\mu(x) \delta_{x+\hat{\mu},x'} + \frac{1+\gamma_\mu}{2} U_\mu^\dagger(x') \delta_{x,x'+\hat{\mu}} \right] \, , \tag{1.18}$$

where L_s is the length of the 5th dimension. Hypercubic-smeared (HYP-smeared) [30, 31, 32, 33] gauge links were used in Eq. (1.17) and (1.18) which reduces lattice artifacts. The physical four dimensional quark fields appear as boundary modes at the surface of the five dimensional space when M_5 lies in the interval $(-2,0)$. The physical quark fields ($\bar{q}(x)$ and $q(x)$ are related to the underlying 5D fermions by [29]

$$\begin{aligned} q(x) &= \frac{1-\gamma_5}{2} \Psi(x,0) + \frac{1+\gamma_5}{2} \Psi(x,L_s-1) \\ \bar{q}(x) &= \bar{\Psi}(x,L_s-1) \frac{1-\gamma_5}{2} + \bar{\Psi}(x,0) \frac{1+\gamma_5}{2} \, . \end{aligned} \tag{1.19}$$

The parameter m in Eq. (1.17) is related to the physical quark mass as it introduces in the effective action a $m\bar{q}q$ term. Domain wall fermions in the infinite L_s limit poses an exact

chiral symmetry when m vanishes. This symmetry transformation is [29]

$$\Psi(x,s) \rightarrow e^{i\Gamma_5(s)\theta(x)}\Psi(x,s) \tag{1.20}$$

$$\bar{\Psi}(x,s) \rightarrow \bar{\Psi}(x,s)e^{-i\Gamma_5(s)\theta(x)} \tag{1.21}$$

where $\Gamma_5(s) = sign(\frac{L_s-1}{2} - s)$.

However, at finite L_s this chiral symmetry is explicitly broken by the coupling of left handed and right handed modes in the middle of the 5th dimension. As a result one can construct the following partially conserved axial vector current [29]

$$\mathcal{A}_\mu(x) = -\sum_{s=0}^{L_s-1} \Gamma_5(s) j_\mu(x,s) \tag{1.22}$$

where j_μ is the four dimensional conserved vector current that corresponds to the 4D Wilson fermion action. This current satisfies a Ward-Takahashi identity which in the flavor non-singlet case takes the form [28]:

$$\begin{aligned}\Delta_\mu\langle\mathcal{A}^a_\mu(x)O(y)\rangle &= 2m\langle\bar{q}(x)\tau^a\gamma_5 q(x)O(y)\rangle + \\ &+ 2\langle\bar{q}_{mp}(x)\tau^a\gamma_5 q_{mp}(x)O(y)\rangle + i\langle\delta^a O(y)\rangle\end{aligned} \tag{1.23}$$

where [29]

$$\begin{aligned}q_{mp}(x) &= \frac{1-\gamma_5}{2}\Psi(x,\frac{L_s}{2}) + \frac{1+\gamma_5}{2}\Psi(x,\frac{L_s}{2}-1) \\ \bar{q}_{mp}(x) &= \bar{\Psi}(x,\frac{L_s}{2}-1)\frac{1-\gamma_5}{2} + \bar{\Psi}(x,\frac{L_s}{2})\frac{1+\gamma_5}{2}\end{aligned} \tag{1.24}$$

are four dimensional fields constructed at the midpoint of the the 5th dimension. The Ward-Takahashi identity of Eq. (1.23) is the same as the continuum counterpart with just an additional term $2\langle\bar{q}_{mp}(x)\tau^a\gamma_5 q_{mp}(x)O(y)\rangle$. This term is there only at finite L_s [1] and it is a measure of the explicit chiral symmetry breaking. At long distances this term is proportional to $2\langle\bar{q}(x)\tau^a\gamma_5 q(x)O(y)\rangle$. Using the pseudo-scalar density as a probe operator $O(y)$ the residual mass is defined as [29]

$$\mathrm{m}_{res} = \frac{1}{t_{max}-t_0}\sum_{t_0}^{t_{max}} \frac{\langle\bar{q}_{mp}(t)\tau^a\gamma_5 q_{mp}(t)\bar{q}(0)\tau^a\gamma_5 q(0)\rangle}{\langle\bar{q}(t)\tau^a\gamma_5 q(t)\bar{q}(0)\tau^a\gamma_5 q(0)\rangle}, \tag{1.25}$$

[1] For the flavor singlet current this term survives the infinite L_s limit and gives rise to the anomaly.

where t_0, t_{max} is the time interval where only the ground state pion contributes to the two correlators in the ratio.

1.2.3 Mixed Action Tuning

The valence and sea quark actions are different, and the calculation is inherently partially quenched, which means that it violates unitarity. Unlike conventional partially quenched calculations, which become unitary when the valence quark mass is tuned to the sea quark mass, unitarity cannot be restored by tuning the valence quark mass [29]. The valence quark mass is tuned in such a way that the resulting domain-wall pions have the same mass as those made of the sea Kogut-Susskind fermions. In this case unitarity should be restored in the continuum limit, where the $n_f = 2$ staggered action has an $SU(8)_L \otimes SU(8)_R \otimes U(1)_V$ chiral symmetry due to the four-fold taste degeneracy of each flavor, and each pion has 15 degenerate additional partners [29]. At finite lattice spacing this symmetry is broken and the taste multiplets are no longer degenerate, but have splittings that are $\mathcal{O}(a^2b^2)$ [34, 35, 36, 37, 38]. The domain wall fermion mass is tuned to give valence pions that match the Goldstone Kogut-Susskind pion [2] . This choice gives pions that are as light as possible, resulting in better convergence of the χ-PT needed to extrapolate the lattice results to the physical quark mass point. This tuning was also done by LHPC collaboration [39, 40, 41, 42, 43, 44].

1.2.4 Contractions

Gauge invariant Gaussian smeared quark propagators centered around a single point were used. In order to facilitate the complicated Wick contractions of the interpolating fields, all the contractions at the annihilation operator point (sink) were performed and all the color and spin indices were left open at the creation operator point (source). The resulting data are Fourier transformed (space indices at the annihilation operator point) and saved on disk as $q\bar{q}$ and qqq blocks. All the two-body (and N-body) correlation functions can

[2]This is the only Goldstone boson that becomes massless in the chiral limit at finite lattice spacing.

then be constructed by appropriate contractions of the source spin and color indices. These operations are typically less expensive than the propagator and block generation, but as the contractions become more complicated, e.g. for multi-baryon systems, the nested loops that are required to implement the Wick contractions make parallelization of the contraction code necessary as well [29].

Code was constructed to automatically perform all permutations, keeping track of the signs associated with fermion exchanges, allowing the construction of complicated diagrams in a relatively simple and efficient manner. This approach works well when quark annihilation diagrams are absent. For this reason, processes such as the $I = 0$ $\pi\pi$ channel and pion-nucleon scattering, which require the all to all propagator method [45, 29] have not been calculated yet.

1.3 Chiral Perturbation Theory

Chiral Perturbation Theory is the low energy effective field theory of QCD. For energies below the ρ mass, the only hadrons that can be produced are the Goldstone bosons. Weinberg stated that a perturbative description in terms of the most general effective Lagrangian containing all possible terms compatible with the assumed symmetry principles yields the most general S matrix consistent with the fundamental principles of quantum field theory and the assumed symmetry principles [46, 47].

The six quark flavors are commonly divided into the three light quarks u, d, and s and the three heavy flavors c, b, and t,

$$\begin{pmatrix} m_u = 0.005\,\text{GeV} \\ m_d = 0.009\,\text{GeV} \\ m_s = 0.175\,\text{GeV} \end{pmatrix} \ll 1\,\text{GeV} \leq \begin{pmatrix} m_c = (1.15 - 1.35)\,\text{GeV} \\ m_b = (4.0 - 4.4)\,\text{GeV} \\ m_t = 174\,\text{GeV} \end{pmatrix}, \tag{1.26}$$

where the scale of 1 GeV is associated with the masses of the lightest hadrons containing light quarks, e.g., m_ρ= 770 MeV, which are not Goldstone bosons resulting from spontaneous symmetry breaking. The scale associated with spontaneous symmetry breaking, $4\pi f \sim 1$ GeV, is of the same order of magnitude [48, 13, 47].

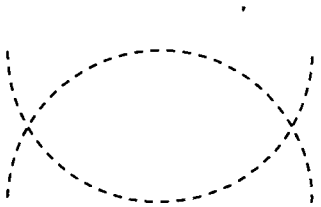

Figure 1-1: pi-pi scattering Feynman diagram

1.3.1 The Chiral Symmetry-Breaking Scale

The most general Lagrangian with $SU(3)_L \times SU(3)_R$ symmetry is of the form

$$\frac{f^2}{4}\mathrm{Tr}(\partial^\mu \Sigma^\dagger \partial_\mu \Sigma) \ , \qquad \Sigma = e^{2i\pi/f} \ . \tag{1.27}$$

Where the π in Eq. (1.27) is a matrix of Goldstone boson fields. Eq. (1.27) describes massless Goldstone bosons. Including the quark masses, the Lagrangian takes the form

$$\mathcal{L}(\pi) = f^4 \left[\frac{1}{4}\mathrm{Tr}(\partial^\mu \Sigma^\dagger \partial_\mu \Sigma) + \frac{1}{2}\mathrm{Tr}(\Sigma^\dagger \mu M) + \frac{1}{2}\mathrm{Tr}(\Sigma \mu M)\right] \ . \tag{1.28}$$

Eq. (1.28) is an effective Lagrangian, and in calculating the effective action, there will be terms that are non-renormalizable with arbitrarily high dimension. In order for this expansion to converge, there must be a dimensionful parameter to suppress the non-renormalizable terms [48].

Expanding Eq. (1.27) in powers of π/f, leads to a four point function of the form

$$\frac{p^2\pi^4}{f^2} \ . \tag{1.29}$$

Where factors of 1.29 occur at the vertices, and the p^2 comes from the derivatives acting on the π fields. There is one case where the derivatives act on the external lines, and the amplitude is

$$\mathcal{F} = \frac{p^4\pi^4}{f^4}\int \frac{d^4k}{(2\pi)^4}\frac{1}{(k^2)^2} = \frac{p^4\pi^4}{f^4}\frac{1}{(4\pi)^2}\log\frac{\Lambda^2_{\chi SB}}{\kappa^2} \ . \tag{1.30}$$

where $\Lambda_{\chi SB}$ is an ultraviolet cutoff, and κ is a renormalization point [48]. The result in Eq. (1.30) can also result from a higher dimensional operator such as

$$\frac{f^2}{\Lambda_{\chi SB}^2}\mathrm{Tr}(\partial^\mu\Sigma\partial^\nu\Sigma^\dagger\partial_\mu\Sigma\partial_\nu\Sigma^\dagger) \ , \tag{1.31}$$

where the factor of $1/\Lambda_{\chi SB}^2$ makes the operator in Eq. (1.31) dimension 4. Changes in the renormalization point κ can be absorbed by redefining the coefficient of Eq. (1.31), and this coefficient should be at least as large as a change in the coefficient introduced by a rescaling of $\mathcal{O}(1)$ in the renormalization point κ for the $\pi\pi$ scattering diagram. This then implies that [48]

$$\frac{f^2}{\Lambda_{\chi SB}^2} \gtrsim \frac{1}{(4\pi)^2} \ , \qquad \Lambda_{\chi SB} \lesssim 4\pi f \ . \tag{1.32}$$

Therefore, the chiral symmetry breaking scale is assumed to be $\Lambda_{\chi SB} \lesssim 4\pi f$. At the physical pion mass, and with $f \approx 93$MeV, $\Lambda_{\chi SB} \sim 1$GeV.

1.3.2 $SU(2)$ and $SU(3)$ χ-PT

In Eq. (1.27), the Goldstone boson fields are matrices. In the $SU(2)$ case they are

$$\pi \ = \ \frac{1}{\sqrt{2}}\begin{pmatrix} \frac{1}{\sqrt{2}}\pi^0 & \pi^+ \\ \pi^- & -\frac{1}{\sqrt{2}}\pi^0 \end{pmatrix} , \tag{1.33}$$

and for the $SU(3)$ case, the Goldstone fields are

$$\pi = \frac{1}{\sqrt{2}}\begin{pmatrix} \frac{1}{\sqrt{2}}\pi^0 + \frac{1}{\sqrt{6}}\eta & \pi^+ & K^+ \\ \pi^- & -\frac{1}{\sqrt{2}}\pi^0 + \frac{1}{\sqrt{6}}\eta & K^0 \\ K^- & \bar{K}^0 & -\frac{2}{\sqrt{6}}\eta \end{pmatrix} , \tag{1.34}$$

In addition to the $SU(3)$ gauge symmetry of QCD, there is an approximate $SU(3)$ flavor symmetry. At very low energies, the only particles in the theory are contained in Eq. (1.34). These are the pseudo-Goldstone bosons, and their mass would be zero, except for the fact that the quark masses explicitly break the symmetry. The consensus is generally that due to the relatively large mass of the s quark, the convergence in the $SU(3)$ sector is somewhat slower as compared with the $SU(2)$ version [47]. This may be the case, however, Ref. [49] shows that the relative size of the strange quark may not necessarily be the reason for slower-convergence in all cases [47].

1.4 Scattering

1.4.1 Scattering in Quantum Mechanics

Quantum mechanical scattering problems are well known, and have been solved in a variety of ways. The main point is that the energy of the two scattering states can be related to a quantity called the phase shift of the wavefunction of the outgoing state. At very low energies, the potential is assumed to be spherically symmetric, and the effective range expansion is a valid approximation. Lüscher's equation that relates the energy of the particles in a finite volume to the phase shift, provides a methodology to circumvent the Maiani-Testa theorem, and extract scattering observables in a finite volume Euclidean spacetime.

In quantum mechanics, the scattering problem is to solve the Schroedinger equation in 3 dimensions, and here considering the case of a central potential

$$-\frac{\hbar^2}{2\mu}\nabla^2\psi(\vec{r}) + V(r)\psi(\vec{r}) = E\psi(\vec{r}) \ , \tag{1.35}$$

then using the well known form of the plane wave solution

$$\psi(\vec{r}) \approx e^{ikz} + f(\theta)\frac{e^{ikr}}{r} \ , \qquad r \to \infty \ , \tag{1.36}$$

expanding in partial waves

$$\psi(\vec{r}) = \sum_{l=0}^{\infty} \psi_l(\vec{r}) Y_{l,0}(\theta) \ , \tag{1.37}$$

and then projecting onto the s-wave ($l = 0$), leads to

$$\psi_0(r) = \frac{i\pi^{1/2}}{kr}(e^{-ikr} - e^{ikr}) + (4\pi)^{1/2}\, \overline{f}\frac{e^{ikr}}{r} \ , \qquad r \to \infty \ . \tag{1.38}$$

By making a change of variable due to spherically-symmetric potentials

$$\psi = \frac{u(r)}{r} \ , \qquad \frac{d^2u}{dr^2} + \kappa(r)u(r) = 0 \ , \qquad \kappa(r) = \pm\frac{[2\mu(E - V(r))]^{1/2}}{\hbar} \ , \tag{1.39}$$

where $r\psi_0$ is a solution to Eq. (1.39), and as $r \to \infty$, $u(r)$ is

$$u(r) = C\sin(kr + \delta) \ . \tag{1.40}$$

Choosing a different normalization for C,

$$u(r) \to v(r) = \frac{\sin(kr + \delta)}{\sin(\delta)} \ , \tag{1.41}$$

then the solution as $r \to \infty$, $E = 0$, is

$$\frac{d^2u_0}{dr^2} = 0 \ , \qquad u_0(r) = C(r - a) \ , \qquad u_0(r) \to v_0(r) = 1 - \frac{r}{a} \ . \tag{1.42}$$

For $kr \to 0$, Eq. (1.41), $v \to v_0$, and

$$v_0 = 1 + kr\cot(\delta) \ , \tag{1.43}$$

which reduces to the familiar relation for the scattering length for an s-wave at zero energy

$$p\cot(\delta) = -\frac{1}{a} \ , \qquad \text{for } \hbar = 1 \ . \tag{1.44}$$

1.4.2 Scattering in a Finite Volume

From Eq. (1.44), the physical observable, the scattering length, is related to $p\cot\delta(p)$. The energy shift from Eq. (1.47) relates the square of the center-of-mass momentum, p, which

is inserted into [50, 51, 52, 53]

$$p \cot \delta(p) \;=\; \frac{1}{\pi L}\, \mathbf{S}(\eta), \qquad \text{where } \eta = \left(\frac{pL}{2\pi}\right)^2 \tag{1.45}$$

which is valid below the inelastic threshold. The regulated three-dimensional sum is [54]

$$\mathbf{S}\,(\eta) \;\equiv\; \sum_{\mathbf{j}}^{|\mathbf{j}|<\Lambda} \frac{1}{|\mathbf{j}|^2 - \eta} \;-\; 4\pi\Lambda \quad , \tag{1.46}$$

where the summation is over all triplets of integers $\mathbf{j}$ such that $|\mathbf{j}| < \Lambda$ and the limit $\Lambda \to \infty$ is implicit [29].

The energy eigenvalue E_n and its deviation from the sum of the rest masses of the particle, ΔE_n, are related to the center-of-mass momentum p_n, a solution of Eq. (1.45), by

$$\begin{aligned} \Delta E_n \;&\equiv\; E_n \;-\; m_1 \;-\; m_2 \;=\; \sqrt{p_n^2 \;+\; m_1^2} \;+\; \sqrt{p_n^2 \;+\; m_2^2} \;-\; m_1 \;-\; m_2 \\ &=\; \frac{p_n^2}{2\mu_{12}} \;+\; \ldots \quad , \end{aligned} \tag{1.47}$$

$$\Delta E_0 \;=\; -\frac{2\pi a}{\mu_{12} L^3}\left[\, 1 \;+\; c_1 \frac{a}{L} \;+\; c_2 \left(\frac{a}{L}\right)^2 \right] \;+\; \mathcal{O}\left(\frac{1}{L^6}\right) \quad , \tag{1.48}$$

with

$$c_1 = \frac{1}{\pi} \sum_{\mathbf{j}\neq\mathbf{0}}^{|\mathbf{j}|<\Lambda} \frac{1}{|\mathbf{j}|^2} \;-\; 4\Lambda \;=\; -2.837297 \;, \tag{1.49}$$

$$c_2 = c_1^2 \;-\; \frac{1}{\pi^2} \sum_{\mathbf{j}\neq\mathbf{0}} \cdot \frac{1}{|\mathbf{j}|^4} \;=\; 6.375183 \tag{1.50}$$

The scattering length, a [3] , is defined by

$$a \;=\; \lim_{p\to 0} \frac{\tan \delta(p)}{p} \;, \tag{1.51}$$

and to illustrate the accuracy of the perturbative formulation of $p \cot \delta$, Eqs. (1.45), and (1.48), are shown in Fig. 1.4.2. Here, a, the scattering length is calculated with Eqs. (1.45), and (1.48), with the regulator Λ_j going from 1 to 101 in steps of 10. This calculation is for the $\pi^+\Sigma^+$case of MILC Ensemble (*ii*) of Table 2.1. The error bars are the jackknife errors for that ensemble, and the band is the value of a using Eq. (1.48).

[3]In the literature, the lattice spacing is often referred to as "a". Throughout this dissertation, the lattice spacing will be referred to as "b", in order to eliminate possible confusion with the scattering length, which is referred to herein as "a"

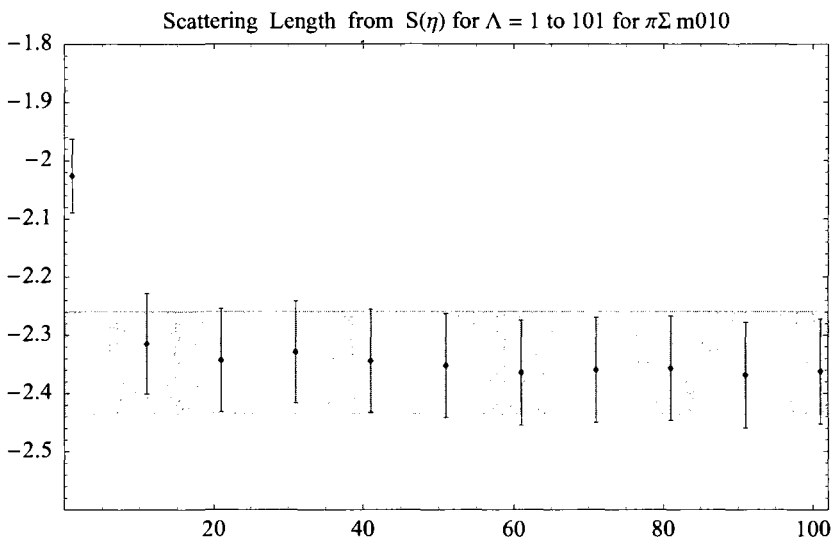

Figure 1-2: The function $p \cot \delta$ of Eq. (1.45) for values of the regulation parameter, Λ. The shaded band is the value of $p \cot \delta$, or $1/a$, calculated with Eq. (1.48)

Chapter 2

LATTICE CALCULATION METHODOLOGY

There are several steps in the calculation of the scattering length using LQCD. Using the MILC gauge configurations [12], and the Chroma software suite [1], the NPLQCD collaboration generated two light and one strange domain wall valence quark propagator for each gauge configuration. Table 2.1 shows the ensembles, and their associated statistics. Using the Chroma software suite, the propagators are calculated, and then blocks are formed. The propagators and blocks are binary files, where the blocks are $q\overline{q}$, and qqq objects, that already have been Wick-contracted at the sink. The remaining operation to extract $C(t)$, the correlator, is the contraction of the spin and color indices at the source, which creates the one-, two-, or N-particle correlator. The correlator is considered "data", and is the part that is analyzed, with the masses and energies extracted from it. With the extracted masses and energies, the scattering length is calculated using Lüscher's method. Part of this process is illustrated in Fig. 2.

2.1 Computational Details

The propagators are gauge invariant gaussian-smeared at the source, meaning that the interpolating operator at the source is constructed from gauge-invariantly-smeared quark field operators, while at the sink, the interpolating operator is constructed from either local quark field operators, or from the same smeared quark field operators used at the source.

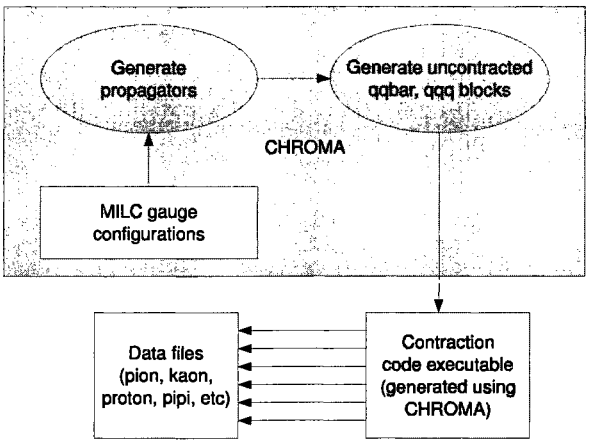

Figure 2-1: Block diagram of the operations involved to generate correlators.

Ensemble	bm_l	bm_s	bm_l^{dwf}	bm_s^{dwf}	$10^3 \times bm_{res}$ [1]	# of propagators
(*i*) 2064f21b676m007m050	0.007	0.050	0.0081	0.081	1.604 ± 0.038	1039×24
(*ii*) 2064f21b676m010m050	0.010	0.050	0.0138	0.081	1.552 ± 0.027	769×24
(*iii*) 2064f21b679m020m050	0.020	0.050	0.0313	0.081	1.239 ± 0.028	486×24
(*iv*) 2064f21b681m030m050	0.030	0.050	0.0478	0.081	0.982 ± 0.030	564×24
(*v*) 2864f21b676m010m050	0.010	0.050	0.0138	0.081	1.552 ± 0.027	128×8
(*vi*) 2896f21b709m0062m031	0.0062	0.031	0.0080	0.0423	0.380 ± 0.006	1001×8
(*vii*) 2896f21b709m0124m031	0.0124	0.031	0.0080	0.0423	0.380 ± 0.006	513×3

Table 2.1: The parameters of the MILC gauge configurations and domain-wall propagators used in this work. The subscript l denotes light quark (up and down), and s denotes the strange quark. The superscript dwf denotes the bare-quark mass for the domain-wall fermion propagator calculation. The last column is the number of configurations times the number of sources per configuration. Ensembles (*i*)-(*iv*) have $L \sim 2.5$ fm and $b \sim 0.125$ fm; Ensemble (*v*) has $L \sim 3.5$ fm and $b \sim 0.125$ fm; Ensembles (*vi*),(*vii*) have $L \sim 2.5$ fm and $b \sim 0.09$ fm.

This method creates two sets of correlation functions. These two sets of correlation functions that result from these source and sink operators are referred to as smeared-point (SP) and smeared-smeared (SS) correlation functions, respectively [55].

2.1.1 Correlation Functions

In the continuum limit, the Fourier transformed Euclidean space correlation functions are sums of exponential functions. A generalized correlation function is [14]

$$C(t) = \langle O(t)O(0)\rangle \ , \qquad O(t) = \sum_{\vec{x}} O(\vec{x},t) \ . \tag{2.1}$$

Using $O(\vec{x},t) = e^{Ht}O(\vec{x},0)e^{-Ht}$, leads to

$$C(t) = \sum_n |\langle 0|O|n\rangle|^2 \mathcal{A}_n e^{-m_n t} \ . \tag{2.2}$$

At large times, the correlation function is dominated by a single exponential dictated by the ground state energy and the overlap of the source and sink with the ground state. Specifically, the pion two-point function, $C_{\pi^+}(t)$ generated by a source (and sink) of the form $\pi^+(\mathbf{x},t) = \overline{u}(\mathbf{x},t)\gamma_5 d(\mathbf{x},t)$,

$$C_{\pi^+}(t) \ = \ \sum_{\mathbf{x}} \langle 0| \ \pi^-(\mathbf{x},t) \ \pi^+(\mathbf{0},0) \ |0\rangle \ = \ \sum_{\mathbf{x}} \langle \pi^-(\mathbf{x},t) \ \pi^+(\mathbf{0},0)\rangle \ . \tag{2.3}$$

The sum over all lattice sites at each time-slice, t, projects onto the three-momenta $\mathbf{p} = \mathbf{0}$ states. The source $\pi^+(\mathbf{x},t)$ couples to all possible states with the same quantum numbers as a single pion, including excited states. The source and sink are smeared over lattice sites in the vicinity of $(\mathbf{x},t)$ to increase the overlap onto the ground state and the lowest-lying excited states. Again, by using time translation, $\pi^+(\mathbf{x},t) = e^{\hat{H}t}\pi^+(\mathbf{x},0)e^{-\hat{H}t}$ yields [55]

$$C_{\pi^+}(t) \ = \ \sum_n \frac{e^{-E_n t}}{2E_n} \sum_{\mathbf{x}} \langle 0| \ \pi^-(\mathbf{x},0)|n\rangle\langle n|\pi^+(\mathbf{0},0)|0\rangle \ \rightarrow \ A_0 \ \frac{e^{-m_\pi t}}{2m_\pi} \ . \tag{2.4}$$

2.2 Signal Extraction

The signal obtained from the correlation functions calculated on the lattice is extracted using standard chi-square minimization fits to one or more functions of the form Ae^{-mt}. Another way to extract the masses and energies is by forming the effective mass plot, and fitting to the function that is produced by generating such a plot, which in essence, linearizes the correlation function. Since the lattice is Euclidean, the time direction has been Wick-rotated, $t \rightarrow it_E$, so the eigenvalues of the Hamiltonian will be decaying exponentials,

rather than oscillatory functions. This is of fundamental importance in terms of the lattice calculation itself, since oscillatory functions in the integrals would not converge, while decaying exponential functions converge quickly. Since the correlators are assumed to be sums of multiple exponential functions, there are challenges with regard to data analysis, some of which are addressed in this section.

2.2.1 Generalized Effective Functions

Effective plots are a useful way to represent the data from a LQCD calculation since the signal is the form of a sum of decaying exponentials. The generalized effective function is defined by Juge, et. al. [56, 57] as

$$m^{\text{eff}}(t) = \frac{1}{n_J} \log \frac{C(t)}{C(t+n_J)} \ . \tag{2.5}$$

Eq. (2.5) assumes that the form of the correlator is dominated by a single exponential decay over some range of time. If there is such behavior, then this will be the effective mass. Additionally, excited state signals are appreciably large in the lower time region, and in the effective plot this appears as curvature in the early time slices.

2.2.2 Digital Filters

Digital Signal Processing of the correlators potentially can increase the signal to noise ratio. Given that the correlators used in the lattice calculations in this work have inherent noise, and since they are a sum of multiple exponentials, it is possible that a digital filter can improve the signal extraction.

Recursive Digital Filters

The ground state signal to be extracted decreases exponentially as a function of time, and there is noise that decreases more slowly, and is an oscillatory signal. A simple, recursive digital filter of the form that follows was used on the correlators to see if the signal to noise ratio could be increased. The form of the digital filter is

$$C(t)_{\text{filtered}} = C(t-1)_{\text{filtered}} + \alpha \left[C(t) - C(t-1)_{\text{filtered}} \right] \ , \tag{2.6}$$

where $C(0)_{\text{filtered}} = C(0)$, and

$$\alpha = \frac{\Delta t}{\tau + \Delta t} \ . \tag{2.7}$$

In a simple analog Resistor-Capacitor (RC) low-pass filter, $\tau = RC$, is the time constant. Fig. 2-2 shows the proton effective mass plots for the low-pass filtered correlators, for several values of α, where α is defined in Eq. (2.7). Note that the $\alpha = 1$ case reduces to the original, unfiltered correlator.

This method requires more study to quantify the systematic error introduced by using it. However, the results shown in Fig. 2-2 (d) are tantalizing, with regard to what appears to be a well-defined plateau.

Non-Recursive Digital Filters

A non-recursive filter appears to be the type of filter that is appropriate for filtering a signal that is expected to be the sum of multiple exponentials. This type of digital filter does not modify the arguments (rate constants) of the exponentials at all, which is essential for accurate determination of energy levels and masses from correlation functions. The form of this type of filter is discussed in [58], and with regard to specific applications to Lattice QCD, in [55].

Inverse Function

In principle, the operators that create the state that overlaps the energy eigenvalue of interest create the particle travelling forward in time, and also travelling backward due to the periodic boundary conditions in time. In the case of the mesons the ground state function looks like

$$C_\phi(t) = \mathcal{A} \cosh(m_\phi t) \ , \tag{2.8}$$

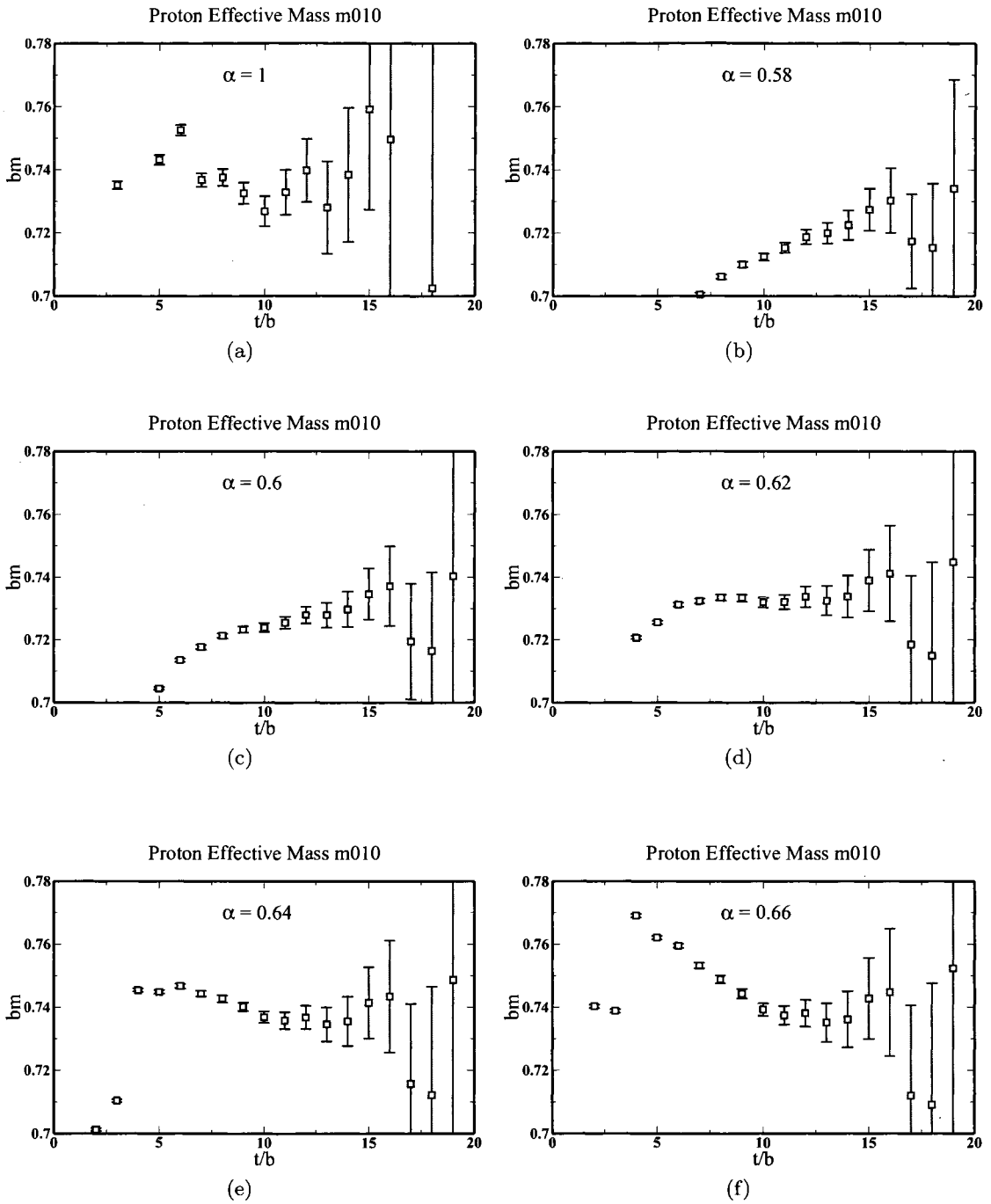

Figure 2-2: First-order, digitally low-pass filtered correlators for MILC Ensemble (*ii*) of Table 2.1, with a filter of the type described by Eq. (2.6).

and the backward-propagating state is visible, i.e. the exponentially-increasing part of Eq. (2.8). By normalizing Eq. (2.8) at each timeslice, t

$$\frac{C(t)}{C(t = L_t/2)} = \cosh[m(t - L_t/2)] \ , \tag{2.9}$$

then, in principle, the original correlator becomes $\cosh(mt)$ with an amplitude of 1. Now, the inverse can be taken and then defining a transformed correlator

$$C'(t) \equiv \exp\left\{ -\cosh^{-1}\left[\frac{C(t)}{C(t = L_t/2)}\right]\right\} = e^{-m(t-L_t/2)} \ . \tag{2.10}$$

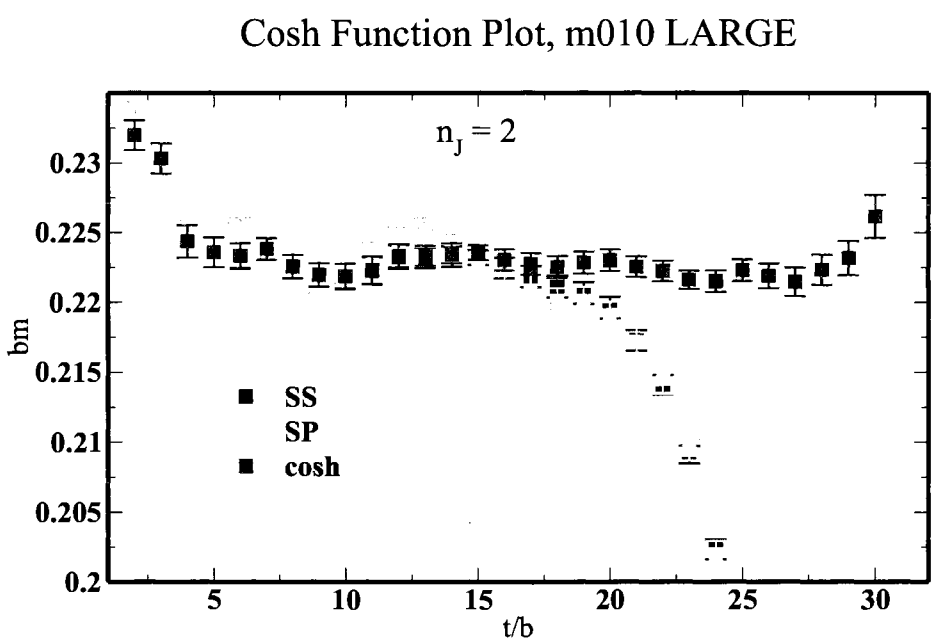

Figure 2-3: The SS and SP effective mass plots for the pion of MILC Ensemble (v) of Table 2.1, and the SS (labeled as cosh in the figure) after applying Eq. (2.10). The backwards propagating state, $\sim \exp(m_\pi t)$ is eliminated.

Eq. (2.10) can be used to construct the effective mass plot. Figure 2-3 illustrates this procedure for the pion correlator of MILC Ensemble (v). It is clear from the plot that the two sets denoted "SS" and "SP" show the effects of the backwards-propagating state. After transforming one of them, in this case "SS", the set labeled by "cosh", the plateau extends

much further in time. Whereas in the cases where the cosh function was not applied, the single particle signal appears viable out to $t \sim 15$, and after applying the cosh, the single particle signal appears viable to $t \sim 28$. It is not yet clear if this will prove beneficial to extracting the ground state, however, if one considers the way that this is usually done for the 2 particle case in order to extract the interaction energy

$$G_{12}(t) = \frac{C_{12}(t)}{C_1(t)C_2(t)} \ , \tag{2.11}$$

Eq. (2.11) assumes that all of the correlation functions decay as a single exponential. By applying Eq. (2.11) to the correlation function, many more time slices are gained in the case of the mesons. This may not be relevant for the baryons right now, because the noise is much greater that the amplitude of the backwards propagating state, but it could be important as statistics keep improving.

2.2.3 Linear Combination of Correlators

The assumed form of single-particle correlators is

$$C(t) = \sum_{n=0}^{\infty} \mathcal{A}_n e^{-m_n t} \ , \tag{2.12}$$

where m_0 is the ground state, and each successive state is an excited state with the same quantum numbers, and for $n > 0$, $m_n > m_0$. By forming a linear combination of the SS and SP correlators, in principle one state can be removed from the correlator as in

$$C^{\mathrm{SS}}(t) - \alpha C^{\mathrm{SP}}(t) = (A - \alpha B)e^{-m_0 t} + (C - \alpha D)e^{-m_1 t} + \dots \ . \tag{2.13}$$

By tuning the parameter α in Eq. (2.13), the first excited state, $e^{-m_1 t}$, can be eliminated. Additionally, this method can be used to eliminate the ground state, in order to extract the first excited state, the utility of this is extensively outlined in [55, 59].

2.2.4 Effective Mass Function as an Overdetermined System of Linear Equations

The generalized effective mass in Eq. (2.5) can be used to form a system of linear equations in order to fit the masses or energies from the lattice data. Once a range of time is identified from the effective plot, then a system of equations can be formed from the effective mass at each time, t, for every n_J that falls within the range. If the range of time is of length N, then there are $N-1+N-2+\ldots+1$ equations for m^{eff}. For example, if $N=4$, and the range of time goes from some t to $t+3$, the system of equations is as follows

$$\Lambda \mathbf{x} = \mathbf{d} \ , \tag{2.14}$$

$$\Lambda = \begin{bmatrix} 1 \\ 1 \\ 1 \\ 2 \\ 2 \\ 3 \end{bmatrix}, \qquad \mathbf{x} = m^{\text{eff}}, \qquad \mathbf{d} = \begin{bmatrix} \log \frac{C(t)}{C(t+1)} \\ \log \frac{C(t+1)}{C(t+2)} \\ \log \frac{C(t+2)}{C(t+3)} \\ \log \frac{C(t)}{C(t+2)} \\ \log \frac{C(t+1)}{C(t+3)} \\ \log \frac{C(t)}{C(t+3)} \end{bmatrix} . \tag{2.15}$$

These equations are not guaranteed to have a unique solution m^{eff}. One can solve a reduced set of equations that correspond to minimizing the squares of the residuals which is the normal equation [60]

$$\Lambda^{\mathrm{T}} \mathbf{d} = \Lambda^{\mathrm{T}} \Lambda \mathbf{x} \ , \tag{2.16}$$

and in the current example becomes

$$\begin{aligned} 20 m^{\text{eff}} &= \log \frac{C(t)}{C(t+1)} + \log \frac{C(t+1)}{C(t+2)} + \log \frac{C(t+2)}{C(t+3)} \\ &\quad + 2 \log \frac{C(t)}{C(t+2)} + 2 \log \frac{C(t+1)}{C(t+3)} + 3 \log \frac{C(t)}{C(t+3)} \ , \end{aligned} \tag{2.17}$$

which is a weighted average. From Eq. (2.17), m^{eff} is calculated. This method is faster than chi-squared minimization, and takes into account non-adjacent timeslices.

Chapter 3

LATTICE RESULTS

3.1 Calculation of the $I = 2$ $\pi^+\pi^+$ scattering length

At the physical charged pion mass, the results of a mixed-action lattice calculation, using the methodology of Sec. 2, the $I = 2$ $\pi\pi$ scattering length was calculated to be $m_\pi a_{\pi\pi}^{I=2} = -0.04330 \pm 0.00042$, where the error bar combines the statistical and systematic uncertainties in quadrature [2].

Pion-pion $\pi\pi$ scattering is one of the best-understood hadronic scattering processes due to the fact that the pions are constrained by chiral symmetry at the maximum level since they are Goldstone bosons, and they have the smallest mass of any hadron. The $I = 2$ channel does not contain any annihilation diagrams which renders it less expensive in terms of computational resources compared to the $I = 0$ channel for a lattice calculation.

The prediction of $m_\pi a_{\pi\pi}^{I=2}$ the from current algebra (Weinberg) [61] and from leading order in χ-PT is

$$m_\pi a_{\pi\pi}^{I=0} = 0.1588 \ ; \ m_\pi a_{\pi\pi}^{I=2} = -0.04537 \ , \tag{3.1}$$

at the charged pion mass.

$\pi\pi$ scattering has been computed with Mixed-Action χ-PT(MAχ-PT) at next-to-leading order (NLO) [62, 63] both for two and three flavors of light quarks. In principle, the fact that this mixed-action theory exists, means that the physical extrapolation is more accurate and precise due to correct calculation of lattice effects due to the mixed valence-sea quark actions.

Using the Roy equations [64, 65, 66], a precise calculation of $m_\pi a_{\pi\pi}^{I=0}$ and $m_\pi a_{\pi\pi}^{I=2}$ is possible, using dispersion theory to relate scattering data at high energies to the scattering amplitude near threshold. Several low-energy constants of one-loop χ-PT are critical inputs to this Roy equation analysis. One can take the values of these low-energy constants computed with lattice QCD by the MILC collaboration [5, 6] as inputs to the Roy equations, and obtain results for the scattering lengths consistent with the analysis of Ref. [7].

In this mixed-action LQCD calculation, MILC ensembles (i)-(iv) are used. At each pion mass, the quantities m_π, f_π, and $\Delta E_{\pi\pi}$ are calculated leading to the extraction of $m_\pi a_{\pi\pi}$ at each pion mass. Fig. 3-1 shows the calculated values of $m_\pi a_{\pi\pi}$ and the result of the $SU(2)$ mixed-action analysis. The $SU(3)$ mixed action corrections have been calculated using three-flavor MAχ-PT [62, 63], and An $SU(3)$ analysis was also performed as a check on the systematic error associated with the chiral expansion.

In two-flavor MAχ-PT(i.e. including finite lattice-spacing corrections) the chiral expansion of the scattering length at NLO takes the form [63]

$$m_\pi \; a_{\pi\pi}^{I=2}(b \neq 0) = -\frac{m_\pi^2}{8\pi f_\pi^2}\left\{1 + \frac{m_\pi^2}{16\pi^2 f_\pi^2}\left[3\log\left(\frac{m_\pi^2}{\mu^2}\right) \; - \; 1 \; - \; l_{\pi\pi}^{I=2}(\mu) \; - \; \frac{\tilde{\Delta}_{ju}^4}{6m_\pi^4}\right]\right\}, \quad (3.2)$$

where it is understood that m_π and f_π are the lattice-physical parameters [63] and

$$\tilde{\Delta}_{ju}^2 \;\; \equiv \tilde{m}_{jj}^2 - m_{uu}^2 = 2B_0(m_j - m_u) + b^2\Delta_I + \ldots, \quad (3.3)$$

where u denotes a valence quark and j denotes a sea-quark, and isospin-symmetric sea and valence quarks are used. $\tilde{m}_{jj}$ (m_{uu}) is the mass of a meson composed of two sea (valence) quarks of mass m_j (m_u) and the dots denote higher-order corrections to the meson masses.

The extrapolated values of the scattering length and a comparison to previous calculations and experiments are in Table 3.1, and Fig. 3-2 is a visual representation of the calculated and measured values of the $I = 2$ $\pi\pi$ scattering length in Table 3.1.

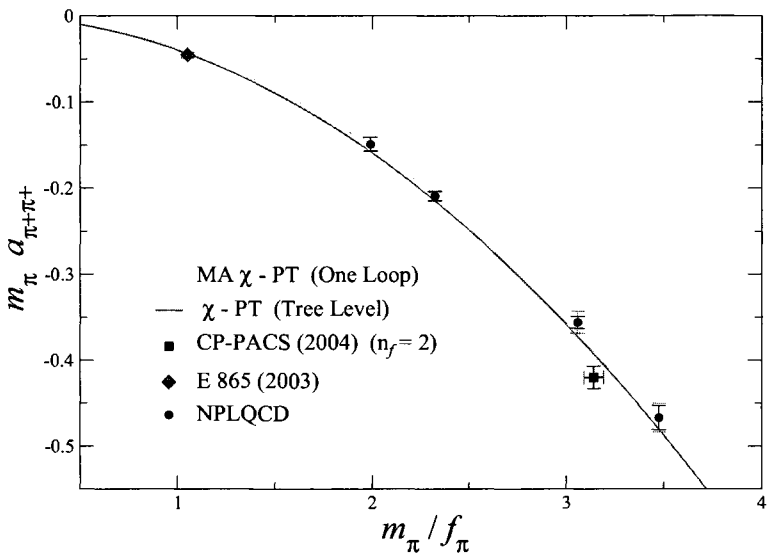

Figure 3-1: $m_\pi\ a_{\pi\pi}^{I=2}$ vs. m_π/f_π (ovals) with statistical (dark bars) and systematic (light bars) uncertainties. Also shown are the experimental value from Ref. [3] (diamond) and the lowest quark mass result of the $n_f = 2$ dynamical calculation of CP-PACS [8] (square). The blue band corresponds to a weighted fit to the lightest three data points (fit B) using the one-loop MAχ-PT formula in Eq. (3.2) (the shaded region corresponds only to the statistical uncertainty). The red line is the tree-level χ-PT result. The experimental data is not used in the chiral extrapolation fits.

	$m_\pi\ a_{\pi\pi}^{I=2}$
χPT (Tree Level)	-0.04438
NPLQCD (2007)	-0.04330 ± 0.00042
E 865 (2003)	$-0.0454 \pm 0.0031 \pm 0.0010 \pm 0.0008$
NPLQCD (2005)	$-0.0426 \pm 0.0006 \pm 0.0003 \pm 0.0018$
MILC (2006)*	-0.0432 ± 0.0006
MILC (2004)*	-0.0433 ± 0.0009
CGL (2001)	-0.0444 ± 0.0010

Table 3.1: A compilation of the various calculations and predictions for the $I = 2$ $\pi\pi$ scattering length. The prediction made in the paper [2] is labeled NPLQCD (2007). Also included are the experimental value from Ref. [3] (E 865 (2003)), the previous determination by NPLQCD [4] (NPLQCD (2005)), two indirect lattice results from MILC [5, 6] (the stars on the MILC results indicate that these are not lattice calculations of the $I = 2$ $\pi\pi$ scattering length but rather a hybrid prediction which uses MILC's determination of various low-energy constants together with the Roy equations), and the Roy equation determination of Ref. [7] (CGL (2001)).

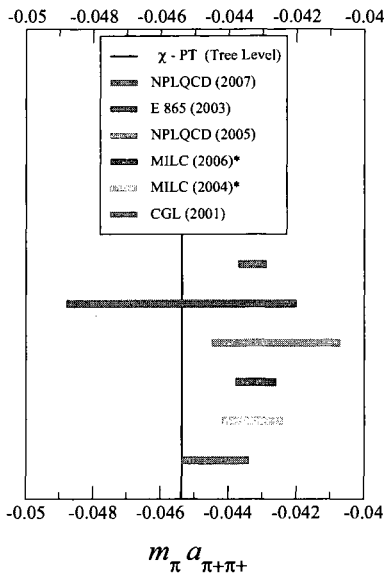

Figure 3-2: Bar chart of the various determinations of the $I = 2$ $\pi\pi$ scattering length tabulated in Table 3.1. The stars on the MILC results indicate that these are not lattice calculations of the $I = 2$ $\pi\pi$ scattering length but rather a hybrid prediction which uses MILC's determination of various low-energy constants together with the Roy equations.

3.2 Calculation of the $I = 1$ K^+K^+ Scattering Length

In Ref. [63], the expression for the $I = 1$ KK scattering length was determined to NLO in χ-PT, including corrections due to mixed-action lattice artifacts. As with the $I = 2$ $\pi\pi$ scattering length [62], it was demonstrated that when the mixed-action extrapolation formula is expressed in terms of the parameters computed on the lattice, m_π, m_K and f_K, there are no lattice-spacing-dependent counterterms at $\mathcal{O}(b^2)$, $\mathcal{O}(b^2 m_K^2)$ or $\mathcal{O}(b^4)$ [67]. There are finite lattice-spacing-dependent corrections, proportional to $b^2\Delta_{\rm I}$, and therefore entirely determined to this order in MAχ-PT. As with the $I = 2$ $\pi\pi$ system, the NLO MA formula for $m_K a_{KK}^{I=1}$ does not depend upon the mixed valence-sea meson masses, and therefore does not require knowledge of the mixed-meson masses [68, 67]. This allows for a precise determination of the predicted MA corrections to the scattering length. At NLO in MAχ-PT,

the scattering length takes the form[67]

$$m_K a_{KK}^{I=1}(b \neq 0) = -\frac{m_K^2}{8\pi f_K^2}\left\{1 + \frac{m_K^2}{(4\pi f_K)^2}\left[C_\pi \ln\left(\frac{m_\pi^2}{\mu^2}\right) + C_K \ln\left(\frac{m_K^2}{\mu^2}\right)\right.\right.$$
$$\left.\left. + C_X \ln\left(\frac{\tilde{m}_X^2}{\mu^2}\right) + C_{ss} \ln\left(\frac{m_{ss}^2}{\mu^2}\right) + C_0 - 32(4\pi)^2 L_{KK}^{I=1}(\mu)\right]\right\}, \quad (3.4)$$

where the various coefficients, C_i, along with $\tilde{m}_X^2$ and m_{ss}^2, can be found in Appendix E of Ref. [63]. To account for the predicted MA corrections, one can either use eq. 3.4 to directly fit the results of the lattice calculation or one can determine the quantity

$$\Delta_{MA}\left(m_K a_{KK}^{I=1}\right) = m_K a_{KK}^{I=1}\Big|_{MA} - m_K a_{KK}^{I=1}\Big|_{\chi-PT}, \quad (3.5)$$

subtract this from the results of the lattice calculation and use the NLO χ-PT expression for the scattering length,

$$m_K a_{KK}^{I=1} = -\frac{m_K^2}{8\pi f_K^2}\left\{1 + \frac{m_K^2}{(4\pi f_K)^2}\left[2\ln\left(\frac{m_K^2}{\mu^2}\right) - \frac{2m_\pi^2}{3(m_\eta^2 - m_\pi^2)}\ln\left(\frac{m_\pi^2}{\mu^2}\right)\right.\right.$$
$$\left.\left. + \frac{2(20m_K^2 - 11m_\pi^2)}{27(m_\eta^2 - m_\pi^2)}\ln\left(\frac{m_\eta^2}{\mu^2}\right) - \frac{14}{9} - 32(4\pi)^2 L_{KK}^{I=1}(\mu)\right]\right\}. \quad (3.6)$$

There is only one counterterm at NLO, and it can be determined on each MILC ensemble. The results of this analysis are illustrated in Fig. 3.2, including the extrapolation to the physical point.

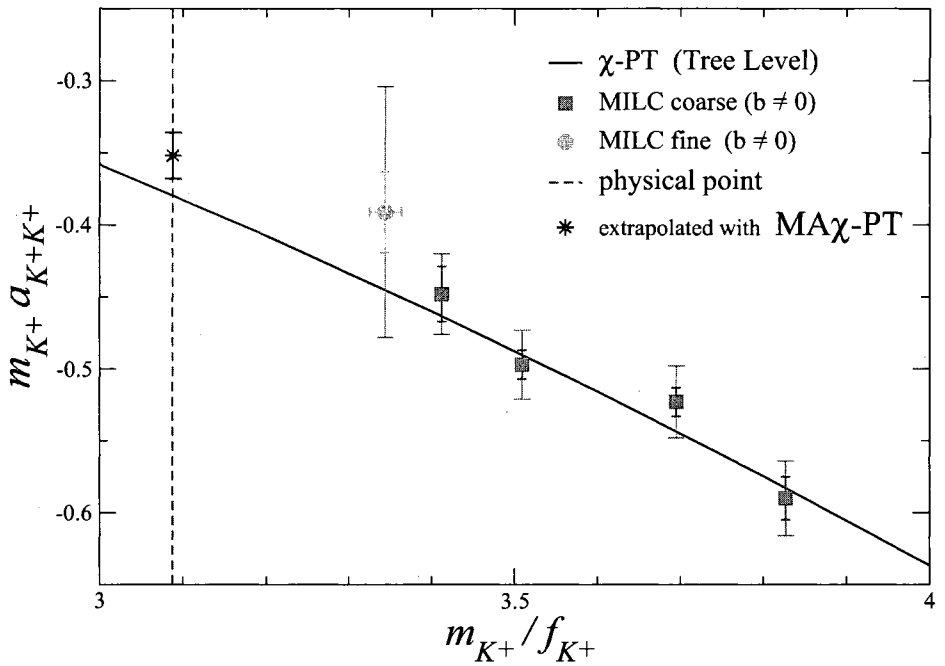

Figure 3-3: $m_{K^+}a_{K^+K^+}$ versus m_{K^+}/f_{K^+}. The points with error-bars are the results of this lattice calculation (not extrapolated to the continuum) on both the coarse and (one) fine MILC lattices. The solid curve corresponds to the tree-level prediction of χ-PT, and the point denoted by a star and its associated uncertainty is the value extrapolated to the physical meson masses and to the continuum. The smaller uncertainty associated with each point is statistical, while the larger uncertainty is the statistical and fitting systematic combined in quadrature.

3.3 Calculation of Multi-Pion States

The NPLQCD collaboration has studied the interactions of multi-meson systems, and extracted a three body interaction from these systems, as well as shown that it is possible to extract the two-body scattering lengths with greater accuracy using these systems. In recent works [69, 70, 71], the analytic volume dependence of the energy of n identical bosons in a periodic volume has been computed to $\mathcal{O}(L^{-7})$, extending the classic results of Bogoliubov [72] and Lee, Huang and Yang [73]. The resulting shift in energy of n particles of mass M due to their interactions is [70]

$$
\begin{aligned}
\Delta E_n \;=\; & \frac{4\pi\,\overline{a}}{M\,L^3}\,{}^nC_2\Bigg\{1-\left(\frac{\overline{a}}{\pi\,L}\right)\mathcal{I}+\left(\frac{\overline{a}}{\pi\,L}\right)^2\left[\mathcal{I}^2+(2n-5)\mathcal{J}\right] \\
& -\left(\frac{\overline{a}}{\pi\,L}\right)^3\left[\mathcal{I}^3+(2n-7)\mathcal{I}\mathcal{J}+\left(5n^2-41n+63\right)\mathcal{K}\right] \\
& +\left(\frac{\overline{a}}{\pi\,L}\right)^4\Big[\mathcal{I}^4-6\mathcal{I}^2\mathcal{J}+(4+n-n^2)\mathcal{J}^2+4(27-15n+n^2)\mathcal{I}\,\mathcal{K} \\
& \qquad +(14n^3-227n^2+919n-1043)\mathcal{L}\,\Big]\Bigg\} \\
& +\,{}^nC_3\left[\frac{192\,\overline{a}^5}{M\pi^3L^7}\left(\mathcal{T}_0\;+\;\mathcal{T}_1\,n\right)\;+\;\frac{6\pi\overline{a}^3}{M^3L^7}\,(n+3)\,\mathcal{I}\right] \\
& +\,{}^nC_3\,\frac{1}{L^6}\,\overline{\overline{\eta}}_3^{\,L}\;\;+\;\mathcal{O}\left(L^{-8}\right)\quad ,
\end{aligned}
\tag{3.7}
$$

where the parameter $\overline{a}$ is related to the scattering length[1] , a, and the effective range, r, by

$$
a \;=\; \overline{a}\;-\;\frac{2\pi}{L^3}\overline{a}^3 r\left(\,1\;-\;\left(\frac{\overline{a}}{\pi L}\right)\,\mathcal{I}\right)\quad . \tag{3.8}
$$

The geometric constants that enter into eq. (3.7) are

$$
\begin{aligned}
\mathcal{I} \;&=\; -8.9136329\,, & \mathcal{J} \;&=\; 16.532316\,, & \mathcal{K} \;&=\; 8.4019240\,, \\
\mathcal{L} \;&=\; 6.9458079\,, & \mathcal{T}_0 \;&=\; -4116.2338\,, & \mathcal{T}_1 \;&=\; 450.6392\,,
\end{aligned}
\tag{3.9}
$$

and ${}^nC_m \;=\; n!/m!/(n-m)!$. The three-body contribution to the energy-shift given in eq. (3.7) is represented by the parameter $\overline{\overline{\eta}}_3^{\,L}$, which is a combination of the volume-dependent, renormalization group invariant quantity, $\overline{\eta}_3^{\,L}$, and contributions from the two-body scattering length and effective range,

$$
\overline{\overline{\eta}}_3^{\,L} \;=\; \overline{\eta}_3^{\,L}\left(\,1\;-\;6\left(\frac{\overline{a}}{\pi L}\right)\,\mathcal{I}\right)\;+\;\frac{72\pi\overline{a}^4 r}{ML}\,\mathcal{I}\quad , \tag{3.10}
$$

where

$$
\overline{\eta}_3^{\,L} = \eta_3(\mu)\;+\;\frac{64\pi a^4}{M}\left(3\sqrt{3}-4\pi\right)\,\log\left(\mu L\right)\;-\;\frac{96a^4}{\pi^2 M}\mathcal{S}_{\rm MS}\quad . \tag{3.11}
$$

The quantity $\eta_3(\mu)$ is the coefficient of the three-π^+ interaction that appears in the effective Hamiltonian density describing the system [70]. It is renormalization scale, μ, dependent.

[1]In this section the Nuclear Physics sign convention for the scattering length is used, which is opposite to that of the Particle Physics sign convention. In this convention, the $\pi^+\pi^+$ scattering length is positive.

The quantity $\mathcal{S}$ is renormalization scheme dependent and its value is given in the minimal subtraction (MS) scheme, $\mathcal{S}_{\rm MS} = -185.12506$.

For $n = 2$, the last two terms in eq. (3.7) vanish and the remaining terms constitute the small $\overline{a}/L$ expansion of the exact eigenvalue equation derived by Lüscher [51, 52]:

The energies of n pion states are dominated by the n single-pion energies, with the interactions contributing a small fraction of the total energy. To extract the resulting energy shifts, ΔE_n, the ratios of correlators

$$G_n(t) = \frac{C_n(t)}{[C_1(t)]^n} \stackrel{t\to\infty}{\longrightarrow} Ae^{-\Delta E_n t}, \tag{3.12}$$

are formed, where the second relation holds in the limit of infinite temporal extent and infinite number of gauge configurations.

The computational aspect of the study of the multi-pion correlators required greater that 64-bit precision in order to compute the contractions up to $N = 13$ pions. In order to accomplish this, the contractions use arbitrary precision arithmetic based on the `ARPREC` library [74] which was extended for the particular operations needed here, matrix multiplications and traces. For the correlators studied, 64 decimal digit precision (approximately octupule precision) in internal operations is sufficient to give results accurate to sixteen digits.

3.4 Meson Baryon Scattering

3.4.1 Overview

In the previous sections it was shown that LQCD calculations of meson-meson interactions have yielded predictions for physical scattering lengths at the few percent level [2, 75, 67]. Several reasons underlie this striking accuracy. Firstly, at the level of the lattice calculation, Euclidean-space correlation functions involving pseudoscalar mesons have signal/noise ratios[2] that do not degrade, or only slowly degrade with time. Therefore, highly accu-

[2]Here the signal is the Monte Carlo estimate of the quantum correlation function evaluated on the lattice, while the noise represents the statistical fluctuations in the correlation function.

rate fits of both single- and multi-meson properties are possible with currently available supercomputer resources. Secondly, and perhaps more importantly, QCD correlation functions involving Goldstone bosons are subject to powerful chiral symmetry constraints. Since current lattice calculations are carried out at unphysical quark masses, these constraints play an essential role in extrapolating the lattice data to the physical quark masses, as well as to the infinite volume, and continuum limits. Chiral perturbation theory (χ-PT) is the optimal method for implementing QCD constraints due to chiral symmetry, and in essence, provides an expansion of low-energy S-matrix elements in quark masses and powers of momentum [76], as in Eq. 1.29.

In contrast to the purely mesonic sector, recent studies of baryon-baryon interactions, have demonstrated the fundamental difficulty faced in making predictions for baryons and their interactions [77, 78]. Unlike the mesons, correlation functions involving baryons suffer an exponential degradation of signal/noise at large times [3] and therefore pose a fundamentally different kind of challenge in extracting signal from data [79]. While baryon interactions are constrained by QCD symmetries like chiral symmetry, the constraints are not nearly as powerful as when there is at least one pion or kaon in the initial or final state. For instance, there is no expectation that the baryon-baryon scattering lengths vanish in the chiral limit as they do in the purely mesonic sector. In nucleon-nucleon scattering, the s-wave interactions are enhanced due to the close proximity of a non-trivial fixed point of the renormalization group, which drives the scattering lengths to infinity, thus rendering the effective field theory description of the interaction highly non-perturbative [80].

Given the contrast in difficulty between the purely mesonic and purely baryonic sectors described above, it is clearly of great interest to perform a lattice QCD investigation of the simplest scattering process involving at least one baryon: meson-baryon scattering. While pion-nucleon scattering is the best-studied process, both theoretically and experimentally, its determination on the lattice is computationally prohibitive since it involves annihilation

[3] A recent high-statistics study of baryon correlation functions on anisotropic clover lattices has found that the exponential decay with time of signal/noise occurs only *asymptotically* in time, and therefore, the signal/noise problem in baryon correlation functions is not nearly as severe as previously thought [55].

diagrams. At present only a few limiting cases that involve these diagrams are being investigated [81]. Combining the lowest-lying $SU(3)$ meson and baryon octets, one can form five meson-baryon elastic scattering processes that do not involve annihilation diagrams. Three of these involve kaons and therefore are, in principle, amenable to an $SU(3)$ heavy-baryon χ-PT (HBχ-PT) analysis [82] for extrapolation. The remaining two processes involve pions interacting with hyperons and therefore can be analyzed in conjunction with the kaon processes in $SU(3)$ HBχ-PT, or independently using $SU(2)$ HBχ-PT.

Meson-baryon scattering has been developed to several non-trivial orders in the $SU(3)$ HBχ-PT expansion in Refs. [83, 84], extending earlier work on kaon-nucleon scattering in Ref. [85]. A very-recent paper [86] has reconsidered the $SU(3)$ HBχ-PT results using a different regularization scheme, and also derived results for pion-hyperon scattering in the $SU(2)$ HBχ-PT expansion. These works make clear that the dearth of experimental data make it is very difficult to assess the convergence of the chiral expansion in the three-flavor case. In the pion-hyperon system, the complete lack of experimental data precludes a separate analysis in the chiral two-flavor expansion. A lattice calculation of meson-baryon scattering analyzed using χ-PT is therefore useful not only in making predictions for low-energy scattering at the physical point, but also for assessing the convergence of the chiral expansion for a range of quark masses at which present-day lattice calculations are being performed.

Meson-baryon scattering is also of interest for several indirect reasons. The K^-n interaction is important for the description of kaon condensation in the interior of neutron stars [87, 88, 89, 90, 91], and meson-baryon interactions are essential input in determining the final-state interactions of various decays that are interesting for standard-model phenomenology (See Ref. [92] for an example). Finally, in determining baryon excited states on the lattice, it is clear that the energy levels that represent meson-baryon scattering on the finite-volume lattice must be resolved before progress can be made regarding the extraction of single-particle excitations.

The experimental input to existing χ-PT analyses of meson-baryon scattering is exten-

sively discussed in Refs. [85, 83, 84, 86]. Threshold pion-nucleon scattering information is taken from experiments with pionic hydrogen and deuterium [93, 94], and the kaon-nucleon scattering lengths are taken from model-dependent extractions from kaon-nucleon scattering data [95]. There is essentially no experimental information available on the pion-hyperon and kaon-hyperon scattering lengths. There have been two quenched lattice QCD studies of meson-baryon scattering parameters: the pioneering work of Ref. [96] calculated pion-nucleon and kaon-nucleon scattering lengths at heavy pion masses without any serious attempt to extrapolate to the physical point, and Ref. [97] calculated the $I = 1$ KN scattering length and found a result consistent with the current algebra prediction.

The lowest-lying energy levels for five meson-baryon processes that have no annihilation diagrams are calculated. These processes are: $\pi^+\Sigma^+$, $\pi^+\Xi^0$, K^+p, K^+n, and $\overline{K}^0\Xi^0$. The calculation uses mixed-action Lattice QCD with domain-wall valence quarks on the asqtad-improved coarse MILC configurations with $b \sim 0.125$ fm at four light-quark masses ($m_\pi \sim$ 291, 352, 491 and 591 MeV), and at two light quark masses ($m_\pi \sim 320$ and 441 MeV) on the fine MILC configurations with $b \sim 0.09$ fm, with substantially less statistics on the fine ensembles. The s-wave scattering lengths from the two-particle energies are extracted, and the five processes are analyzed using $SU(3)$ HBχ-PT. There is a rather conclusive lack of convergence in the three-flavor chiral expansion. Then, considering $\pi^+\Sigma^+$ and $\pi^+\Xi^0$ with $SU(2)$ HBχ-PT reliable predictions of the scattering lengths at the physical point are made. These are

$$a_{\pi^+\Sigma^+} = -0.197 \pm 0.017 \text{ fm} ; \tag{3.13}$$

$$a_{\pi^+\Xi^0} = -0.098 \pm 0.017 \text{ fm} , \tag{3.14}$$

where the errors encompass statistical and systematic uncertainties. The leading order χ-PT (current algebra) predictions for the scattering lengths are given by [61]:

$$a_{\pi^+\Sigma^+} = -0.2294 \text{ fm} ; \tag{3.15}$$

$$a_{\pi^+\Xi^0} = -0.1158 \text{ fm} . \tag{3.16}$$

Ultimately, either the chiral extrapolation should be performed after a continuum limit

has been taken, or one should use the mixed-action extension of HBχ-PT to perform the chiral extrapolations [98, 99]. However, the results on the fine MILC configurations are statistics-limited and not yet sufficiently accurate to make this a useful exercise. Further, the explicit extrapolation formulas for the meson-baryon scattering lengths have not yet been determined in mixed-action χ-PT. Despite these limitations, one expects the corrections from finite lattice spacing to be small for two principle reasons. Firstly, the meson-baryon scattering lengths are protected by chiral symmetry and therefore the (approximate) chiral symmetry of the domain wall valence fermions used in this work protects the scattering lengths from additive renormalization, which can be explicitly seen in the construction of the mixed-action baryon Lagrangian in Ref. [99]. The mixed-action corrections do not appear until next-to-next-to leading order in the chiral expansion of the meson-baryon scattering lengths. Secondly, previous calculations with the mesons using this mixed-action lattice QCD program suggest that discretization effects will be well-encompassed within the overall errors. In the precise calculation of meson-meson scattering, the predicted mixed-action corrections [62, 63] were smaller than the uncertainties on a given ensemble [2, 67].

3.4.2 Meson-Baryon Scattering Processes

The six scattering channels involving the lowest-lying octet mesons and baryons that do not have annihilation diagrams, [4] as well as the particle content, isospin, and valence quark content of these meson-baryon states are shown in Table 3.2.

The notation of Ref. [83] is adopted, denoting the threshold T-matrix in the isospin basis as $T^{(I)}_{\phi B}$, where I is the isospin of the meson-baryon combination, ϕ is the meson, and B is the baryon. The five elastic meson-baryon scattering processes that considered here

[4]The $\pi^+\Xi^0$ and $\overline{K}^0\Sigma^+$ systems have the same quantum numbers, and therefore require a mixed channel analysis in order to extract the $\overline{K}^0\Sigma^+$ scattering length. This is discussed in Section 3.4.5.

Particles	Isospin	Quark Content
$\pi^+\Sigma^+$	2	$uu\bar{u}d\bar{s}$
$\pi^+\Xi^0$	3/2	$uu\bar{d}ss$
K^+p	1	$uuud\bar{s}$
K^+n	0 *and* 1	$uudd\bar{s}$
$\overline{K}^0\Sigma^+$	3/2	$uu\bar{d}ss$
$\overline{K}^0\Xi^0$	1	$u\bar{d}sss$

Table 3.2: Particle content, isospin, and valence quark structure of the meson-baryon states calculated in this work. As is clear from the valence quark content, these meson-baryon states have no annihilation diagrams.

are then in correspondence with the isospin amplitudes according to

$$T_{\pi^+\Sigma^+} = T^{(2)}_{\pi\Sigma} \quad ; \qquad T_{\pi^+\Xi^0} = T^{(3/2)}_{\pi\Xi} \; ;$$
$$T_{K^+p} = T^{(1)}_{KN} \; ; \qquad T_{K^+n} \;=\; \frac{1}{2}(T^{(1)}_{KN} + T^{(0)}_{KN}) \; ; \qquad T_{\overline{K}^0\Xi^0} = T^{(1)}_{\overline{K}\Xi} \; . \tag{3.17}$$

These threshold T-matrices are related to the scattering lengths $a_{\phi B}$ through

$$T_{\phi B} = 4\pi \left(1 + \frac{m_\phi}{m_B}\right) a_{\phi B} \; , \tag{3.18}$$

where m_ϕ is the meson mass and m_B is the baryon mass.

3.4.3 Finite-Volume Calculation of Scattering Amplitudes

The s-wave scattering amplitude for two particles below inelastic thresholds can be determined using either Eq. (1.45), or Eq. (1.48). As the finite-volume lattice calculation cannot achieve $p = 0$ (except in the absence of interactions), in quoting a lattice value for the scattering length extracted from the ground-state energy level, it is important to determine the error associated with higher-order range corrections.

3.4.4 Lattice Calculation and Data Analysis

In calculating the meson-baryon scattering lengths, the mixed-action lattice QCD scheme was used in which domain-wall quark [100, 101, 27, 102, 28] propagators are generated from

a smeared source on $n_f = 2+1$ asqtad-improved [34, 35] rooted, staggered sea quarks [103]. To improve the chiral symmetry properties of the domain-wall quarks, hypercubic-smearing (HYP-smearing) [30, 31, 32] was used in the gauge links of the valence-quark action. In the sea-quark sector, there has been significant debate regarding the validity of taking the fourth root of the staggered fermion determinant at finite lattice spacing [33, 19, 20, 104, 21, 105, 24, 106, 107, 105, 22, 23, 25, 26]. While there is no proof, there are arguments to suggest that taking the fourth root of the fermion determinant recovers the contribution from a single Dirac fermion. The results of this paper assume that the fourth-root trick recovers the correct continuum limit of QCD.

The present calculations were performed predominantly with the coarse MILC lattices with a lattice spacing of $b \sim 0.125$ fm, and a spatial extent of $L \sim 2.5$ fm. On these configurations, the strange quark was held fixed near its physical value while the degenerate light quarks were varied over a range of masses corresponding to the pion masses shown in Table 2.1. See Ref. [29] for further details. Results were also obtained on a coarse MILC ensemble with a spatial extent of $L \sim 3.5$ fm. However, this data is statistics limited. In addition, calculations were performed on two fine MILC ensembles at $L \sim 2.5$ fm with $b \sim 0.09$ fm. On the coarse MILC lattices, Dirichlet boundary conditions were implemented to reduce the original time extent of 64 down to 32, which saved a nominal factor of two in computational time. While this procedure leads to minimal degradation of a nucleon signal, it does limit the number of time slices available for fitting meson properties. By contrast, on the fine MILC ensembles, anti-periodic boundary conditions were implemented and all time slices are available.

The correlation function that projects onto the zero momentum state for the meson-baryon system is

$$C_{\phi B}(t) = \mathcal{P}_{ij} \sum_{\mathbf{x},\mathbf{y}} \langle \phi^\dagger(t,\mathbf{x}) \overline{B_i}(t,\mathbf{y}) \phi(0,\mathbf{0}) B_j(0,\mathbf{0}) \rangle \ , \tag{3.19}$$

where $\mathcal{P}_{ij}$ is a positive-energy projector. For instance, in the case of K^+p, the interpolating

operators for the K^+ and the proton are

$$\begin{aligned} \phi(t,\mathbf{x}) &= K^+(t,\mathbf{x}) = \overline{s}(t,\mathbf{x})\gamma_5 u(t,\mathbf{x}) \ ; \\ B_i(t,\mathbf{x}) &= p_i(t,\mathbf{x}) = \epsilon_{abc} u_i^a(t,\mathbf{x}) \left(u^{b\mathrm{T}}(t,\mathbf{x}) C\gamma_5 d^c(t,\mathbf{x}) \right) \ . \end{aligned} \tag{3.20}$$

The masses of the mesons and baryons are extracted using the assumed form of the large-time behavior of the single particle correlators as a function of time. As $t \to \infty$, the ground state dominates; however, fluctuations of the correlator increase with respect to the ground state. The meson and baryon two-point correlators, $C_\phi(t)$ and $C_B(t)$, behave as

$$C_\phi(t) \ \to \ \mathcal{A}_1 \ e^{-m_\phi \ t}, \qquad C_B(t) \ \to \ \mathcal{A}_2 \ e^{-m_B \ t} \ , \tag{3.21}$$

respectively, in the limits $t \to \infty$ and $L \to \infty$. In relatively large lattice volumes the energy difference between the interacting and non-interacting meson-baryon states is a small fraction of the total energy, which is dominated by the masses of the mesons and baryons [2]. In order to extract this energy difference the ratio of correlation functions, $G_{\phi B}(t)$, is formed

$$G_{\phi B}(t) \equiv \frac{C_{\phi B}(t)}{C_\phi(t) C_B(t)} \ = \ \sum_{n=0}^{\infty} \mathcal{D}_n \ e^{-\Delta E_n \ t} \ , \tag{3.22}$$

where $\Delta E \equiv \Delta E_0$ is the desired energy shift. With ΔE, and the extracted masses of the meson and baryon, the scattering length can be calculated using Eqs. (1.45) and (1.47), or, if $a << L$, from Eq. (1.48). For the meson-baryon scattering lengths calculated in this work, the difference between the exact and perturbative eigen-equations is negligible.

A variety of fitting methods have been used, including standard chi-square minimization fits to one and two exponentials. Generalized effective energy plots, as discussed in 2.2.1, are particularly useful for analyzing the lattice data and for estimating systematic errors [55]. In the meson-baryon case, the functions take the forms

$$m_{\phi,B}^{\mathrm{eff}} = \frac{1}{n_J} \log \left(\frac{C_{\phi,B}(t)}{C_{\phi,B}(t+n_J)} \right), \qquad \Delta E_{\phi B}^{\mathrm{eff}} = \frac{1}{n_J} \log \left(\frac{G_{\phi B}(t)}{G_{\phi B}(t+n_J)} \right) \ . \tag{3.23}$$

With $n_J = 1$, the standard effective mass and energy plots are recovered. Additional details regarding the utility of generalized effective mass and energy plots can be found in Ref. [59].

The interpolating operator at the source is constructed from gauge-invariantly-smeared quark field operators, while at the sink, the interpolating operator is constructed from either local quark field operators, or from the same smeared quark field operators used at the source, leading to two sets of correlation functions. For brevity, the two sets of correlation functions that result from these source and sink operators are referred to as *smeared-point* (SP) and *smeared-smeared* (SS) correlation functions, respectively. By forming a linear combination of the SP and SS correlation functions, $C^{(\mathrm{SS})} - \alpha C^{(\mathrm{SP})}$, one is able to remove the first excited state, thus gaining early time slices for fitting [59]. This effect is illustrated in Fig. 3-4, which is the effective $\Delta E_{\pi^+\Sigma^+}$ plot for coarse MILC ensemble (*ii*), plotting $C^{(\mathrm{SS})}$, $C^{(\mathrm{SP})}$, and $C^{(\mathrm{SS})} - \alpha C^{(\mathrm{SP})}$ with α tuned to remove the first excited state. The effective energies, for coarse MILC ensemble (*ii*) are plotted in Fig. 3-5. The effective masses and energy splittings for coarse MILC ensembles (*i*)-(*iv*) are plotted in Appendix A. All of the necessary quantities needed for extraction of the scattering lengths are contained in Table 3.3, which also contains the sum of meson and baryon masses at each quark mass. Fig. 3-6 shows the results for all five processes, and the behavior of Eq. (1.45), versus the interaction energy, presented in terms of the dimensionless quantities $p\cot\delta/m_\pi$ and $\Delta E/m_\pi$. The curve shown in Fig. 3-6 is $p\cot\delta/m_\pi$ for the case of $m_\phi = m_K$, and $m_B = m_p$, as $\Delta E/m_\pi$ is varied. $\mathbf{S}(\eta)$ in Eq. (1.46) is a function of the meson and baryon masses, so there will be a unique curve for each combination of m_ϕ and m_B. Consequently, the K^+p, and K^+n data points fall on this curve.

3.4.5 The Mixed Channel

As is clear from Table I, the $\pi^+\Xi^0$ and $\overline{K}^0\Sigma^+$ states carry the same global quantum numbers, and therefore couple to the same energy-eigenstates in the finite lattice volume. For energies above both kinematic thresholds, a determination of the three scattering parameters associated with these states (two phases and one mixing-angle) requires a coupled-channel analysis. Therefore, three energy levels above both kinematic thresholds must be determined in the lattice calculation to fully characterize scattering in this kinematic regime.

Quantity	m007 (*i*)	m010 (*ii*)	m020 (*iii*)	m030 (*iv*)
m_π	0.18384(31)(03)	0.22305(25)(08)	0.31031(38)(95)	0.37513(44)(13)
m_k	0.36783(32)(42)	0.37816(26)(11)	0.40510(33)(37)	0.43091(66)(16)
m_p	0.6978(61)(08)	0.7324(31)(10)	0.8069(22)(14)	0.8741(16)(05)
m_Σ	0.8390(22)(03)	0.8531(19)(08)	0.8830(18)(17)	0.9213(13)(03)
m_Ξ	0.8872(13)(16)	0.9009(13)(10)	0.9233(18)(04)	0.9461(14)(08)
f_π	0.09257(16)	0.09600(14)	0.10208(14)	0.10763(32)
f_K	0.10734(10)	0.10781(18)	0.10976(17)	0.11253(31)
$\Delta E_{\pi\Sigma}$	0.0150(14)(08)	0.0148(08)(13)	0.0111(10)(08)	0.0100(10)(11)
$\Delta E_{\pi\Xi}$	0.00646(64)(98)	0.0062(05)(12)	0.00431(68)(43)	0.00421(76)(60)
ΔE_{Kp}	0.0140(22)(30)	0.0146(15)(13)	0.0092(10)(51)	0.0087(16)(16)
ΔE_{Kn}	0.0057(18)(16)	0.0051(14)(09)	0.0036(09)(12)	0.0028(10)(11)
$\Delta E_{K\Xi}$	0.0118(08)(13)	0.0125(05)(14)	0.0085(08)(31)	0.0086(16)(16)
$a_{\pi\Sigma}$	-2.12(16)(09)	-2.36(09)(15)	-2.30(15)(13)	-2.36(18)(19)
$a_{\pi\Xi}$	-1.08(09)(14)	-1.19(09)(20)	-1.08(15)(09)	-1.20(18)(15)
a_{Kp}	-2.80(32)(44)	-2.95(21)(19)	-2.3(0.2)(1.0)	-2.27(31)(32)
a_{Kn}	-1.41(37)(34)	-1.33(30)(21)	-1.05(22)(30)	-0.89(27)(31)
$a_{K\Xi}$	-2.62(13)(21)	-2.77(08)(23)	-2.18(15)(63)	-2.29(30)(32)
$m_\pi + m_p$	0.8817(61)	0.9555(31)	1.1172(23)	1.2492(18)
$m_\pi + m_\Sigma$	1.0229(23)	1.0761(20)	1.1933(19)	1.2964(15)
$m_\pi + m_\Xi$	1.0710(14)	1.1240(14)	1.2336(19)	1.3212(16)
$m_K + m_p$	1.0657(61)	1.1106(31)	1.2119(23)	1.3050(19)
$m_K + m_\Sigma$	1.2069(23)	1.2312(20)	1.2881(19)	1.3522(16)
$m_K + m_\Xi$	1.2550(14)	1.2791(15)	1.3284(19)	1.3770(17)

Table 3.3: Lattice calculation results from the four coarse MILC ensembles which enter the analysis of the meson-baryon scattering lengths. The first uncertainty is statistical and the second uncertainty is systematic due to fitting. All quantities are in lattice units.

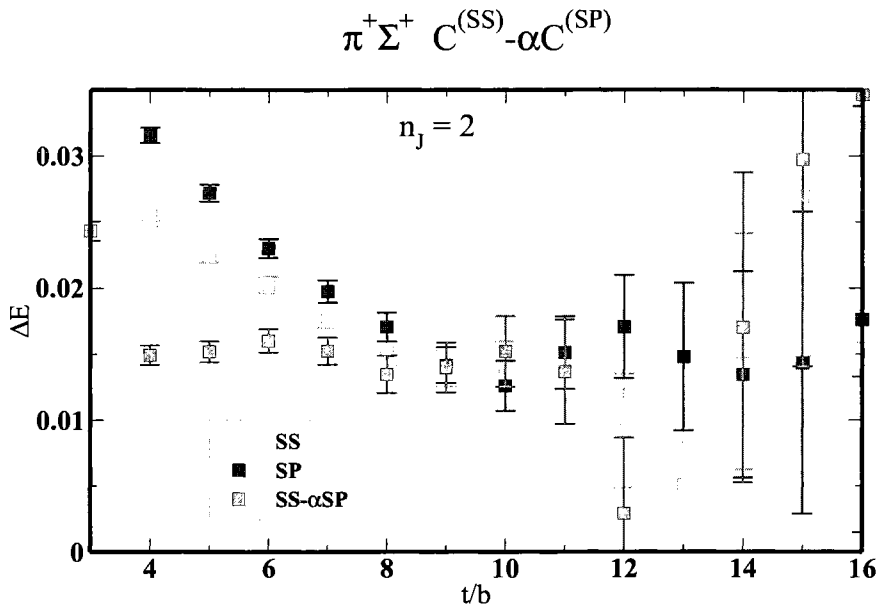

Figure 3-4: Effective $\Delta E_{\pi^+\Sigma^+}$ plot for coarse MILC ensemble (*ii*) from correlation functions $C^{(\mathrm{SS})}$, $C^{(\mathrm{SP})}$ and $C^{(\mathrm{SS})} - \alpha C^{(\mathrm{SP})}$. By taking the linear combination with α tuned to remove the first excited state, earlier time slices are gained for fitting.

In the present lattice volumes, the two-particle energies in these channels are close to the respective kinematic thresholds, and the energy of the lower-lying $\pi^+\Xi^0$ state (which is below the $\overline{K}^0\Sigma^+$ threshold) is determined by the low-energy elastic scattering parameters, making it amenable to analysis using Eqs. (1.45), (1.46), (1.47) and (1.48).

A priori, one would expect both the $\pi^+\Xi^0$ and $\overline{K}^0\Sigma^+$ interpolating operators to couple to a common ground state (dominantly the $\pi^+\Xi^0$ state), with a $\overline{K}^0\Sigma^+$-related level as the first excited state (for the lattice volumes considered here, the non-interacting $\pi^+\Xi^0$ system with two units of relative momentum has an energy considerably above the $\overline{K}^0\Sigma^+$ threshold). Interestingly, within statistical and systematic uncertainties, there are distinct energy levels from the two interpolating operators. This is consistent with strong coupling to the color-singlet constituents of the interpolating operator and only very weak couplings to states that require color rearrangement (see Fig. 3-5). While this is suggestive that mixing between the states is small, a definitive interpretation requires an extraction of three energy levels above the kinematic thresholds of the $\pi^+\Xi^0$ and $\overline{K}^0\Sigma^+$, and below the next kinematic threshold, in order to determine the three scattering parameters. The optimal

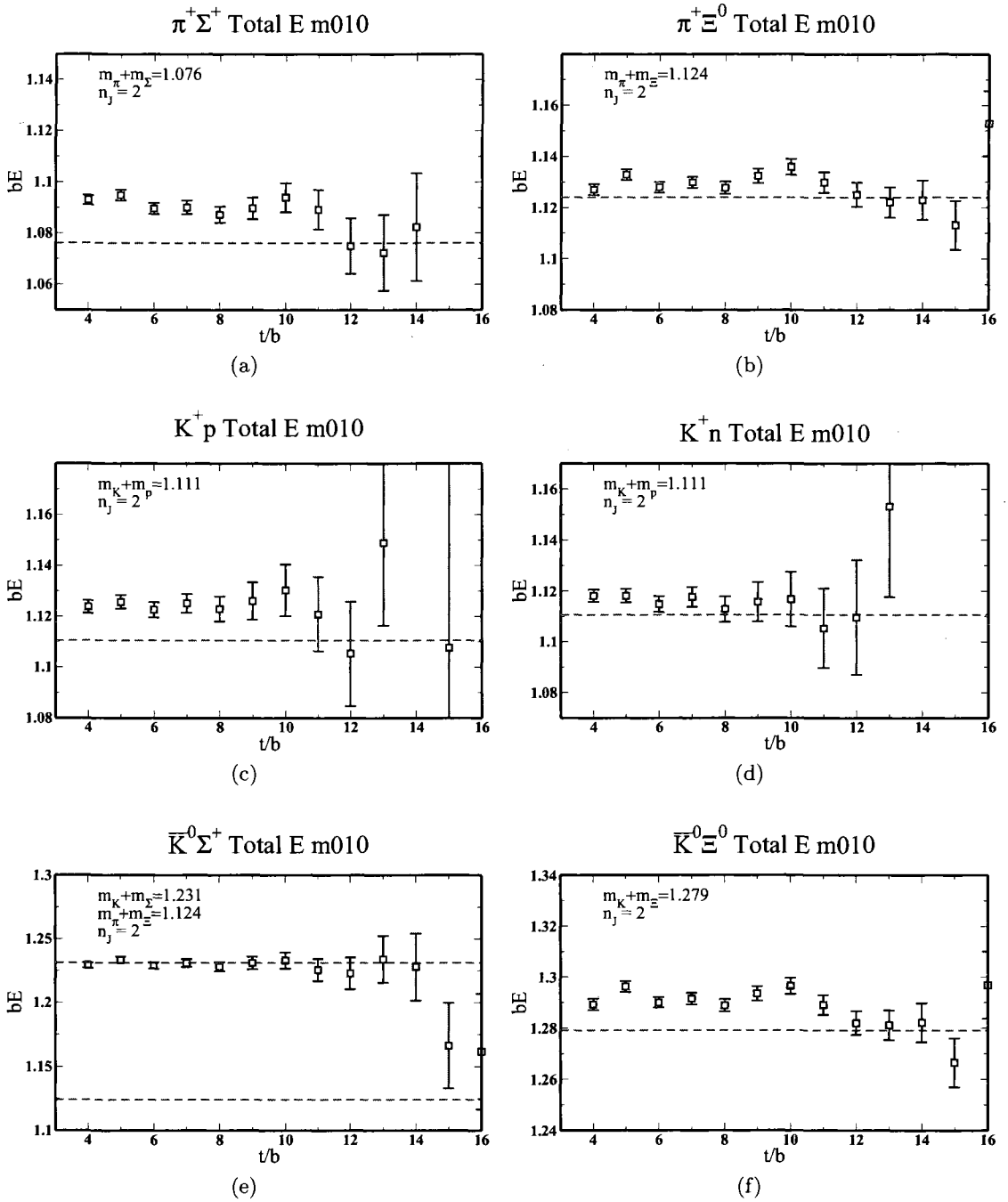

Figure 3-5: Effective energy plots of the six meson-baryon processes shown in Table 3.2. The plots are from MILC ensemble (*ii*), $n_J = 2$, and the linear combination $C^{(\mathrm{SS})} - \alpha C^{(\mathrm{SP})}$ is plotted. The dashed line is the sum of the meson and baryon masses for each process, while the error bars represent the jackknife uncertainty. Note that the bE axis of (e) is a factor of two larger in span than the other plots to encompass the dashed line at $m_\pi + m_\Xi = 1.124$.

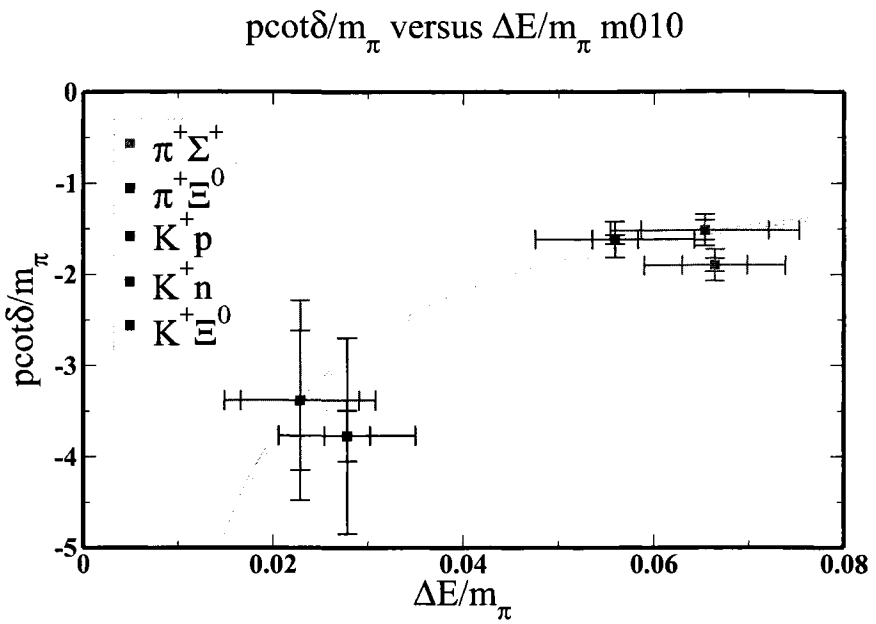

Figure 3-6: $p\cot\delta/m_\pi$ versus $\Delta E_{\phi B}/m_\pi$ for the five elastic scattering processes from coarse MILC ensemble (*ii*). The curve shown is $p\cot\delta/m_\pi$ for the case of $m_\phi = m_K$, and $m_B = m_p$.

way to extract these levels is to use the variational method [108, 109], which requires the full matrix of correlation functions to be calculated, and diagonalized. The extraction of the scattering parameters would then proceed via an extension of the variational method to the coupled-channel scenario [110, 111].

Due to our incomplete knowledge of the three mixed-channel energy levels, no $\overline{K}^0\Sigma^+$ scattering parameters are extracted in this work.

3.4.6 SU(3) HBχPT Extrapolation

Scattering Length Formulas

The scattering lengths of the five meson-baryon processes listed in Eq. (3.17) are, to $\mathcal{O}(m_\pi^3)$ in $SU(3)$ HBχ-PT [83, 84],

$$a_{\pi^+\Sigma^+} = \frac{1}{4\pi}\frac{m_\Sigma}{m_\pi + m_\Sigma}\left[-\frac{2m_\pi}{f_\pi^2} + \frac{2m_\pi^2}{f_\pi^2}C_1 + \mathcal{Y}_{\pi^+\Sigma^+}(\mu) + 8h_{123}(\mu)\frac{m_\pi^3}{f_\pi^2}\right]; \tag{3.24}$$

$$a_{\pi^+\Xi^0} = \frac{1}{4\pi}\frac{m_\Xi}{m_\pi + m_\Xi}\left[-\frac{m_\pi}{f_\pi^2} + \frac{m_\pi^2}{f_\pi^2}C_{01} + \mathcal{Y}_{\pi^+\Xi^0}(\mu) + 8h_1(\mu)\frac{m_\pi^3}{f_\pi^2}\right]; \tag{3.25}$$

$$a_{K^+p} = \frac{1}{4\pi}\frac{m_N}{m_K+m_N}\left[-\frac{2m_K}{f_K^2}+\frac{2m_K^2}{f_K^2}C_1+\mathcal{Y}_{K^+p}(\mu)+8h_{123}(\mu)\frac{m_K^3}{f_K^2}\right]; \tag{3.26}$$

$$a_{K^+n} = \frac{1}{4\pi}\frac{m_N}{m_K+m_N}\left[-\frac{m_K}{f_K^2}+\frac{m_K^2}{f_K^2}C_{01}+\mathcal{Y}_{K^+n}(\mu)+8h_1(\mu)\frac{m_K^3}{f_K^2}\right]; \tag{3.27}$$

$$a_{\overline{K}^0\Xi^0} = \frac{1}{4\pi}\frac{m_\Xi}{m_K+m_\Xi}\left[-\frac{2m_K}{f_K^2}+\frac{2m_K^2}{f_K^2}C_1+\mathcal{Y}_{\overline{K}^0\Xi^0}(\mu)+8h_{123}(\mu)\frac{m_K^3}{f_K^2}\right], \tag{3.28}$$

where we have defined $C_{01} \equiv C_0 + C_1$ and $h_{123} \equiv h_1 - h_2 + h_3$, and the loop functions are given by

$$\begin{aligned}\mathcal{Y}_{\pi^+\Sigma^+}(\mu) &= \frac{m_\pi^2}{2\pi^2 f_\pi^4}\Big\{-m_\pi\left(\frac{3}{2}-2\ln\frac{m_\pi}{\mu}-\ln\frac{m_K}{\mu}\right)\\ &\quad -\sqrt{m_K^2-m_\pi^2}\arccos\frac{m_\pi}{m_K}+\frac{\pi}{2}\left[3F^2m_\pi-\frac{1}{3}D^2m_\eta\right]\Big\};\end{aligned} \tag{3.29}$$

$$\begin{aligned}\mathcal{Y}_{\pi^+\Xi^0}(\mu) &= \frac{m_\pi^2}{4\pi^2 f_\pi^4}\Big\{-m_\pi\left(\frac{3}{2}-2\ln\frac{m_\pi}{\mu}-\ln\frac{m_K}{\mu}\right)-\sqrt{m_K^2-m_\pi^2}\left(\pi+\arccos\frac{m_\pi}{m_K}\right)\\ &\quad +\frac{\pi}{4}\left[3(D-F)^2m_\pi-\frac{1}{3}(D+3F)^2m_\eta\right]\Big\};\end{aligned} \tag{3.30}$$

$$\begin{aligned}\mathcal{Y}_{K^+p}(\mu) &= \frac{m_K^2}{4\pi^2 f_K^4}\Big\{m_K\left(-3+2\ln\frac{m_\pi}{\mu}+\ln\frac{m_K}{\mu}+3\ln\frac{m_\eta}{\mu}\right)\\ &\quad +2\sqrt{m_K^2-m_\pi^2}\ln\frac{m_K+\sqrt{m_K^2-m_\pi^2}}{m_\pi}-3\sqrt{m_\eta^2-m_K^2}\arccos\frac{m_K}{m_\eta}\\ &\quad -\frac{\pi}{6}(D-3F)\left[2(D+F)\frac{m_\pi^2}{m_\eta+m_\pi}+(D+5F)m_\eta\right]\Big\};\end{aligned} \tag{3.31}$$

$$\begin{aligned}\mathcal{Y}_{K^+n}(\mu) &= \frac{\mathcal{Y}_{K^+p}}{2}+\frac{3m_K^2}{8\pi^2 f_K^4}\Big\{m_K\left(\ln\frac{m_\pi}{\mu}-\ln\frac{m_K}{\mu}\right)+\sqrt{m_K^2-m_\pi^2}\ln\frac{m_K+\sqrt{m_K^2-m_\pi^2}}{m_\pi}\\ &\quad +\frac{\pi}{3}(D-3F)\left[(D+F)\frac{m_\pi^2}{m_\eta+m_\pi}+\frac{1}{6}(7D+3F)m_\eta\right]\Big\};\end{aligned} \tag{3.32}$$

$$\begin{aligned}\mathcal{Y}^{(1)}_{\overline{K}^0\Xi^0}(\mu) &= \frac{m_K^2}{4\pi^2 f_K^4}\Big\{m_K\left(-3+2\ln\frac{m_\pi}{\mu}+\ln\frac{m_K}{\mu}+3\ln\frac{m_\eta}{\mu}\right)\\ &\quad +2\sqrt{m_K^2-m_\pi^2}\ln\frac{m_K+\sqrt{m_K^2-m_\pi^2}}{m_\pi}-3\sqrt{m_\eta^2-m_K^2}\arccos\frac{m_K}{m_\eta}\\ &\quad -\frac{\pi}{6}(D+3F)\left[2(D-F)\frac{m_\pi^2}{m_\eta+m_\pi}+(D-5F)m_\eta\right]\Big\}.\end{aligned} \tag{3.33}$$

In what follows, $\mu = \Lambda_\chi = 4\pi f_\pi$ and f_π is evaluated at its lattice physical value [4], and m_η is calculated from the Gell-Mann-Okubo formula. These choices modify the chiral expansion at $\mathcal{O}(m_\pi^4)$ and are therefore consistent to this order. The first mixed-action modification to these HBχ-PT extrapolation formulas appear as corrections to these loop functions, $\mathcal{Y}_{\phi B}$, and to the corresponding counterterms which absorb the scale dependence. Some of the mesons propagating in the loops appear as mixed valence-sea combinations, and thus the corresponding meson masses appearing in these functions are heavier by a known amount [68]. The precise form of the predicted corrections require a computation of the scattering processes with mixed-action/partially quenched χ-PT.

Our physical parameters are consistent with Ref. [86] (note that our decay constant convention differs by $\sqrt{2}$). Namely, $f_\pi = 130.7$ MeV, $m_\pi = 139.57$ MeV, $f_K = 159.8$ MeV, $m_K = 493.68$ MeV, $m_N = 938$ MeV, $m_\Sigma = 1192$ MeV and $m_\Xi = 1314$ MeV. The axial couplings, D and F, for coarse MILC ensembles (ii)-(iv) are taken from the mixed-action calculation of Ref. [112], and extrapolate for coarse MILC ensemble (i) using these values.

Extrapolation to the Physical Point

For the purposes of fitting and visualization, it is useful to construct from the scattering lengths the functions $\Gamma^{(1,2)}$ which are polynomials in m_ϕ. For the $\pi^+\Sigma^+$, K^+p, and $\overline{K}^0\Xi^0$ processes one defines[5]

$$\Gamma^{(1)}_{LO} \equiv -\frac{2\pi a f_\phi^2}{m_\phi}\left(1 + \frac{m_\phi}{m_B}\right) = 1 \; ; \tag{3.34}$$

$$\Gamma^{(1)}_{NLO} \equiv -\frac{2\pi a f_\phi^2}{m_\phi}\left(1 + \frac{m_\phi}{m_B}\right) = 1 - C_1 m_\phi \; ; \tag{3.35}$$

$$\Gamma^{(1)}_{NNLO} \equiv -\frac{2\pi a f_\phi^2}{m_\phi}\left(1 + \frac{m_\phi}{m_B}\right) + \frac{f_\phi^2}{2m_\phi}\mathcal{Y}_{\phi B}(\Lambda_\chi) = 1 - C_1 m_\phi - 4h_{123}(\Lambda_\chi)m_\phi^2 \; , \tag{3.36}$$

and for the $\pi^+\Xi^0$, and K^+n processes one defines

$$\Gamma^{(2)}_{LO} \equiv -\frac{4\pi a f_\phi^2}{m_\phi}\left(1 + \frac{m_\phi}{m_B}\right) = 1 \; ; \tag{3.37}$$

[5]Here the standard notation, LO = leading order, NLO = next-to-leading order and so on is used.

$$\Gamma^{(2)}_{NLO} \equiv -\frac{4\pi a f_\phi^2}{m_\phi}\left(1+\frac{m_\phi}{m_B}\right) = 1 - C_{01} m_\phi \; ; \tag{3.38}$$

$$\Gamma^{(2)}_{NNLO} \equiv -\frac{4\pi a f_\phi^2}{m_\phi}\left(1+\frac{m_\phi}{m_B}\right) + \frac{f_\phi^2}{m_\phi}\mathcal{Y}_{\phi B}(\Lambda_\chi) = 1 - C_{01} m_\phi - 8h_1(\Lambda_\chi) m_\phi^2 \; . \tag{3.39}$$

Notice that the left-hand sides of these equations are given entirely in terms of lattice-determined quantities, all evaluated under Jackknife, whereas the right-hand side provides a convenient polynomial fitting function. Plots of Γ_{NLO} formed from the lattice data (all ensembles listed in Table 2.1) versus the Goldstone masses are given in Fig. 3-7. There is evidence in this plot that the fine and large-volume coarse data are statistically limited as compared to the coarse data. Therefore, only the coarse data is included in the fits. The fine data is, however, indicative that lattice-spacing effects are small.

In the three-flavor chiral expansion, there is an overdetermined system at both NLO and NNLO. While there are five observables, there are two Low Energy Constants (LECs) at NLO, C_0 and C_{01}, and two LECs at NNLO, h_1 and h_{123}. Fits of the LECs from each process at NLO are given in Table 3.4 and the corresponding values of the scattering lengths are given in Table 3.5. At NLO, the LECs are of natural size, and provide a consistent extraction within uncertainties. Correspondingly, the scattering lengths appear to deviate perturbatively from the LO values. The perturbative behavior of the scattering lengths at NLO is evident from the plots of Γ_{NLO} versus the Goldstone masses given in Fig. 3-8. Clearly the deviations of the lattice data from unity are consistent with a perturbative expansion.

At NNLO the situation changes dramatically. This is clear from the plots of Γ_{NNLO} versus the Goldstone masses given in Fig. 3-8. The shift of the value of Γ from NLO to NNLO is dependent on the renormalization scale μ. With the choice $\mu = \Lambda_\chi$ one would expect this shift to be perturbative. However, this is not the case and therefore loop corrections are very large at the scale Λ_χ. There are many strategies that one may take to fit the LECs in the overdetermined system. Here the LECs are fit to the $\pi^+\Sigma^+$ and $\pi^+\Xi^0$ data, and then use these LECs to predict the kaon processes. Therefore, in Fig. 3-8, only (a) and (b) are fits. The fit LECs are given in Table 3.4. While the NNLO LECs h_1

Quantity	NLO fit each process	NNLO fit $\pi^+\Sigma^+$,$\pi^+\Xi^0$
$C_1(\pi^+\Sigma^+)$	0.66(04)(11) GeV^{-1}	3.51(18)(25) GeV^{-1}
$C_{01}(\pi^+\Xi^0)$	0.69(06)(22) GeV^{-1}	7.44(29)(69) GeV^{-1}
$C_1(K^+p)$	0.44(09)(23) GeV^{-1}	-
$C_{01}(K^+n)$	0.56(11)(27) GeV^{-1}	-
$C_1(\overline{K}^0\Xi^0)$	0.50(06)(14) GeV^{-1}	-
h_1	-	-0.59(08)(14) GeV^{-2}
h_{123}	-	-0.42(10)(10) GeV^{-2}

Table 3.4: $SU(3)$ LECs fit from each process at NLO, and from $\pi^+\Sigma^+$, and $\pi^+\Xi^0$ at NNLO. The first uncertainty in parentheses is statistical, and the second is the statistical and systematic uncertainty added in quadrature.

Quantity	LO (fm)	NLO fit (fm)	NLO (NNLO fit) (fm)	NNLO (fm)
$a_{\pi\Sigma}$	-0.2294	-0.208(01)(03)	-0.117(06)(08)	-0.197(06)(08)
$a_{\pi\Xi}$	-0.1158	-0.105(01)(04)	0.004(05)(11)	-0.096(05)(12)
a_{Kp}	-0.3971	-0.311(18)(44)	0.292(35)(48)	-0.154(51)(63)
a_{Kn}	-0.1986	-0.143(10)(27)	0.531(28)(68)	0.128(42)(87)
$a_{K\Xi}$	-0.4406	-0.331(12)(31)	0.324(39)(54)	-0.127(57)(70)

Table 3.5: $SU(3)$ extrapolated scattering lengths using the LECs from Table 3.4. The first uncertainty in parentheses is statistical, and the second is the statistical and systematic uncertainty added in quadrature. Note that the NLO (NNLO fit) column is using C_1, C_{01} from the NNLO fit to $\pi^+\Sigma^+$,$\pi^+\Xi^0$.

and h_{123} appear to be of natural size, the NLO LECs C_0 and C_{01} are unnaturally large and therefore are countering the large loop effects. The extrapolated $\pi^+\Sigma^+$ and $\pi^+\Xi^0$ scattering lengths are given in Table 3.5 and appear to be perturbative. Table 3.5 also gives the extrapolated kaon-baryon scattering lengths with the LECs determined from the $\pi^+\Sigma^+$ and $\pi^+\Xi^0$ data. The resulting NNLO predictions deviate by at least 100% from the LO values. Other fitting strategies lead to this same conclusion: the kaon-baryon scattering lengths are unstable against chiral corrections in the three-flavor chiral expansion, over the range of light-quark masses considered.

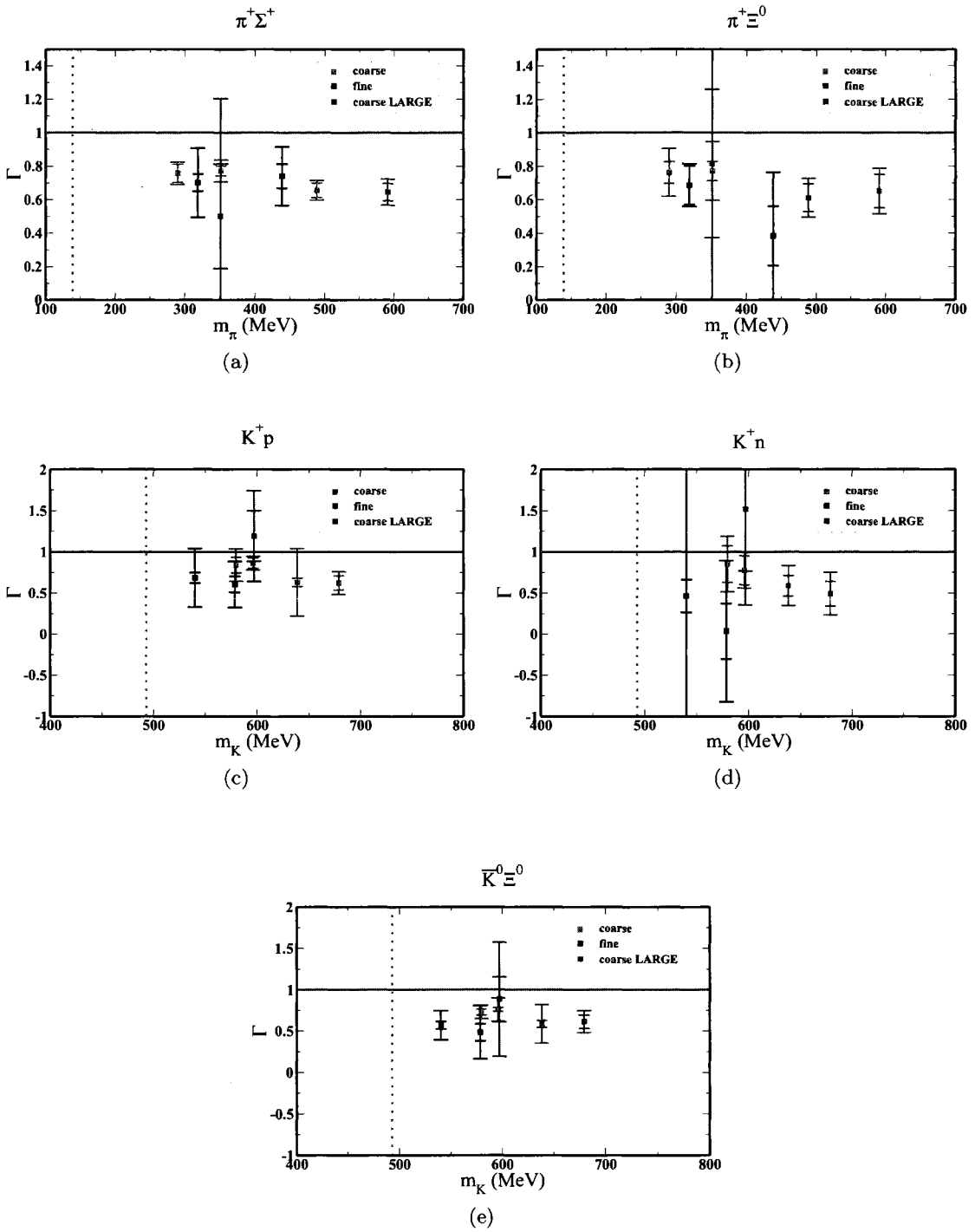

Figure 3-7: Plots of Γ_{NLO} versus the Goldstone masses for the five meson-baryon processes. All lattice data is included.

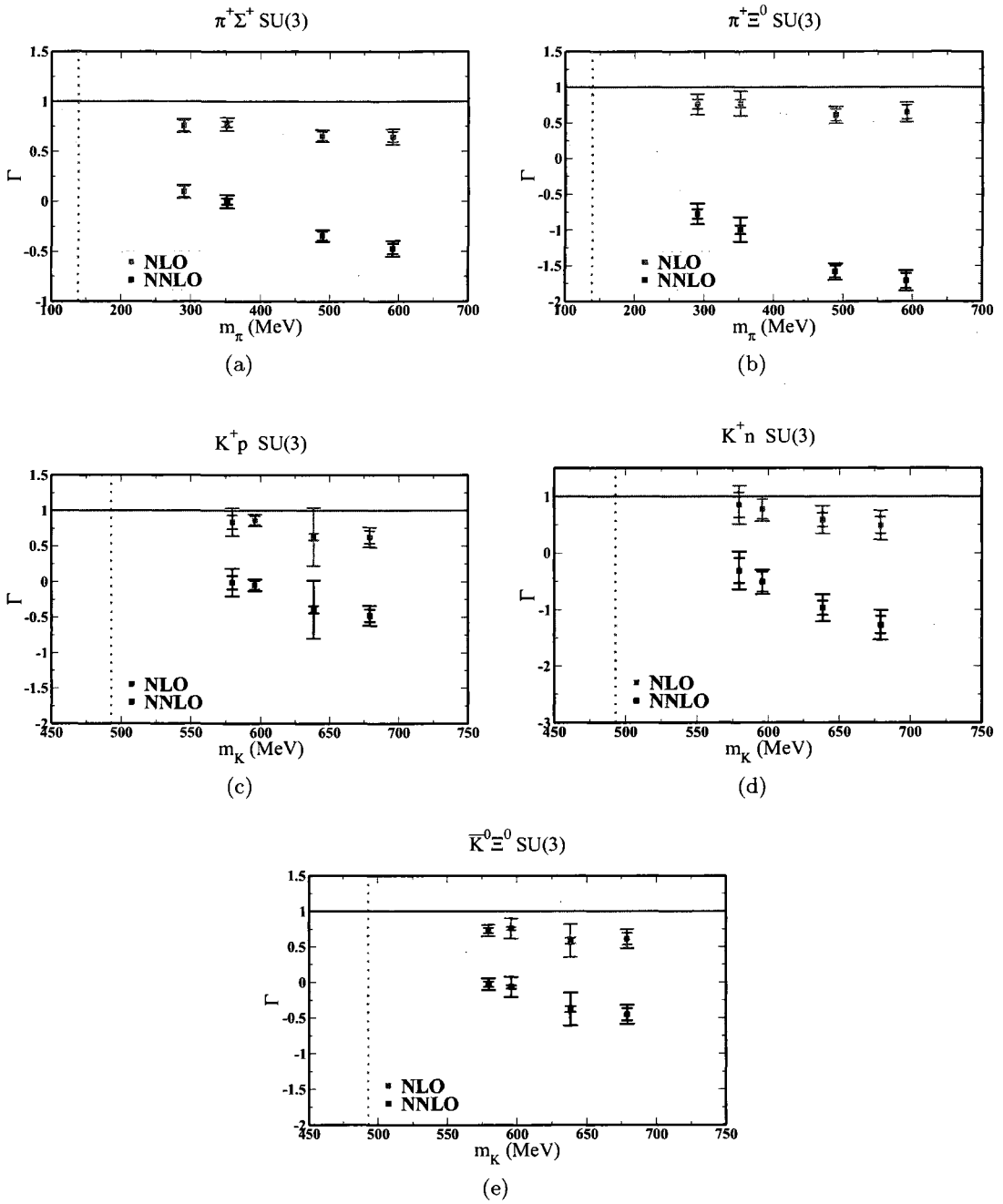

Figure 3-8: Plots of Γ_{NLO} and Γ_{NNLO} versus the Goldstone masses. The line at $\Gamma = 1$ is the leading order curve, and dotted line is the physical meson mass. The innermost error bar is the statistical uncertainty and the outermost error bar is the statistical and systematic uncertainty added in quadrature. The inner and outer filled bands correspond to the statistical and systematic uncertainty, respectively, of the fits to the LECs at NLO and NNLO using $\pi^+\Sigma^+$, and $\pi^+\Xi^0$ *only*, for the SU(3) case.

3.4.7 SU(2) HBχPT Extrapolation

Given the poor convergence seen in the three-flavor chiral expansion due to the large loop corrections, it is natural to consider the two-flavor theory with the strange quark integrated out. In this way, $\pi\Sigma$ and $\pi\Xi$ may be analyzed in an expansion in m_π with no fear of corrections that scale as powers of m_K. The detailed matching of LECs between the three- and two-flavor theories is described in detail in Ref. [86]. The formulation of the $\pi\Sigma$ and $\pi\Xi$ T-matrices from [86] is useful to perform the two-flavor chiral extrapolations for $a_{\pi^+\Sigma^+}$, and $a_{\pi^+\Xi^0}$. As pointed out in Ref. [86], there are two representations of the pion-hyperon scattering lengths that are equivalent up to omitted higher orders in the chiral expansion; one contains a chiral logarithm, and the other is purely a polynomial in m_π. Using both forms provides a useful check on the systematics of the chiral extrapolation.

Scattering Length Formulas I

To $\mathcal{O}(m_\pi^3)$ in the two-flavor chiral expansion, $a_{\pi^+\Sigma^+}$ and $a_{\pi^+\Xi^0}$ are given by [86]

$$a_{\pi^+\Sigma^+} = \frac{1}{4\pi}\frac{m_\Sigma}{m_\pi + m_\Sigma}\left[-\frac{2m_\pi}{f_\pi^2} + \frac{2m_\pi^2}{f_\pi^2}\mathrm{C}_{\pi^+\Sigma^+} + \frac{m_\pi^3}{\pi^2 f_\pi^4}\log\frac{m_\pi}{\mu} + \frac{2m_\pi^3}{f_\pi^2}h_{\pi^+\Sigma^+}(\mu)\right] ; \quad (3.40)$$

$$a_{\pi^+\Xi^0} = \frac{1}{4\pi}\frac{m_\Xi}{m_\pi + m_\Xi}\left[-\frac{m_\pi}{f_\pi^2} + \frac{m_\pi^2}{f_\pi^2}\mathrm{C}_{\pi^+\Xi^0} + \frac{m_\pi^3}{2\pi^2 f_\pi^4}\log\frac{m_\pi}{\mu} + \frac{m_\pi^3}{f_\pi^2}h_{\pi^+\Xi^0}(\mu)\right] , \quad (3.41)$$

where the explicit forms —in terms of Lagrangian parameters— of the LECs $\mathrm{C}_{\pi^+\Sigma^+}$, $h_{\pi^+\Sigma^+}$, $\mathrm{C}_{\pi^+\Xi^0}$ and $h_{\pi^+\Xi^0}$ are given in Ref. [86]. As in the three flavor case, the mixed-action modification to the $SU(2)$ scattering length formula would begin with corrections to the $m_\pi^3\ln(m_\pi)$ terms, with the mixed valence-sea pions having the known additive mass shift [68]. Again, $\mu = \Lambda_\chi = 4\pi f_\pi$ and f_π is evaluated at its lattice physical value. In analogy with the three-flavor case

$$\Gamma_{LO} \equiv 1 ; \quad (3.42)$$

$$\Gamma_{NLO} \equiv 1 - C_{\pi^+B}m_\pi ; \quad (3.43)$$

$$\Gamma_{NNLO} \equiv 1 - C_{\pi+B} m_\pi - h_{\pi+B}(\Lambda_\chi) m_\pi^2 \ , \tag{3.44}$$

where B is either Σ^+ or Ξ^0. In Fig. 3-9 plots of Γ_{NLO} and Γ_{NNLO} versus the pion mass for the two-flavor case are shown. Clearly the deviations of Γ from unity are consistent with a perturbative expansion at both NLO and NNLO, showing that the loop corrections are much smaller at the scale Λ_χ than in the three-flavor case. All extracted LECs are of natural size and given in Table 3.6. The extrapolated $\pi^+\Sigma^+$ and $\pi^+\Xi^0$ scattering lengths are given in Table 3.7. The results are consistent with what was found in the three-flavor extrapolation. The NLO and NNLO LECs are highly correlated in the NNLO fit. Fig. 3-10 shows the 68% and 95% confidence interval error ellipses in the h-C plane for both $\pi^+\Sigma^+$ and $\pi^+\Xi^0$. Exploring the full 95% confidence interval error ellipse in the h-C plane yields

$$a_{\pi+\Sigma^+} = -0.197 \pm 0.017 \text{ fm} \ ; \tag{3.45}$$

$$a_{\pi+\Xi^0} = -0.098 \pm 0.017 \text{ fm} \ . \tag{3.46}$$

These are the numbers that are the best determinations of the pion-hyperon scattering lengths from this calculation.

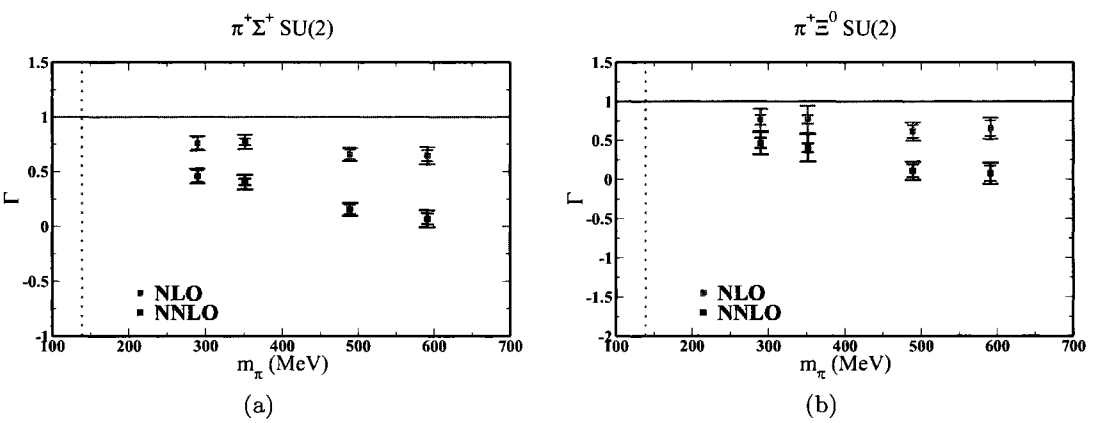

Figure 3-9: Γ_{NLO}, Γ_{NNLO} plots for the $\pi^+\Sigma^+$, and $\pi^+\Xi^0$ processes versus the pion mass. The line at $\Gamma = 1$ is the leading order curve, and the dotted line is the physical pion mass. The innermost error bar is the statistical uncertainty and the outermost error bar is the statistical and systematic uncertainty added in quadrature. The inner and outer filled bands correspond to the statistical and systematic uncertainty, respectively, of the fits to the LECs at NLO and NNLO using $\pi^+\Sigma^+$, and $\pi^+\Xi^0$ for the SU(2) case.

	NLO fit	NNLO fit
$C_{\pi^+\Sigma^+}$	0.66(04)(11) GeV^{-1}	1.98(17)(24) GeV^{-1}
$C_{\pi^+\Xi^0}$	0.69(06)(22) GeV^{-1}	2.01(24)(68) GeV^{-1}
$h_{\pi^+\Sigma^+}$	-	-0.65(36)(40) GeV^{-2}
$h_{\pi^+\Xi^0}$	-	-0.6(0.5)(1.1) GeV^{-2}

Table 3.6: $SU(2)$ LECs fit from each process at NLO and at NNLO. The first uncertainty in parentheses is statistical, and the second is the statistical and systematic uncertainty added in quadrature.

Quantity	LO (fm)	NLO (fm)	NLO (NNLO fit) (fm)	NNLO (fm)
$a_{\pi\Sigma}$	-0.2294	-0.208(01)(03)	-0.166(05)(08)	-0.197(06)(08)
$a_{\pi\Xi}$	-0.1158	-0.105(01)(04)	-0.083(04)(11)	-0.098(05)(12)

Table 3.7: $SU(2)$ extrapolated scattering lengths using the LECs from Table 3.6. The first uncertainty in parentheses is statistical, and the second is the statistical and systematic uncertainty added in quadrature.

Scattering Length Formulas II

Ref. [86] makes the interesting observation that replacing f_π with its chiral limit value, f, yields

$$a_{\pi^+\Sigma^+} = \frac{1}{2\pi}\frac{m_\Sigma}{m_\pi + m_\Sigma}\left[-\frac{m_\pi}{f^2} + \frac{m_\pi^2}{f^2}\mathrm{C}_{\pi^+\Sigma^+} + \frac{m_\pi^3}{f^2}h'_{\pi^+\Sigma^+}\right], \qquad h'_{\pi^+\Sigma^+} = \frac{4}{f^2}\ell_4^r + h_{\pi^+\Sigma^+} \quad (3.47)$$

$$a_{\pi^+\Xi^0} = \frac{1}{4\pi}\frac{m_\Xi}{m_\pi + m_\Xi}\left[-\frac{m_\pi}{f^2} + \frac{m_\pi^2}{f^2}\mathrm{C}_{\pi^+\Xi^0} + \frac{m_\pi^3}{f^2}h'_{\pi^+\Xi^0}\right], \qquad h'_{\pi^+\Xi^0} = \frac{4}{f^2}\ell_4^r + h_{\pi^+\Xi^0} \quad (3.48)$$

where ℓ_4^r is the LEC which governs the pion mass dependence of f_π [7]. Note that the chiral logs have canceled, and in this form, valid to order m_π^3 in the chiral expansion, the scattering lengths have a simple polynomial dependence on m_π. Taking the standard value $f = 122.9$ MeV [7, 86] and refitting the LECs yields the results tabulated in Table 3.8. The extrapolated $\pi^+\Sigma^+$ and $\pi^+\Xi^0$ scattering lengths are given in Table 3.9. These results are clearly consistent with what was found in the two-flavor extrapolation with the chiral logarithm explicit. Fig. 3-11 shows the 68% and 95% confidence interval error ellipses in

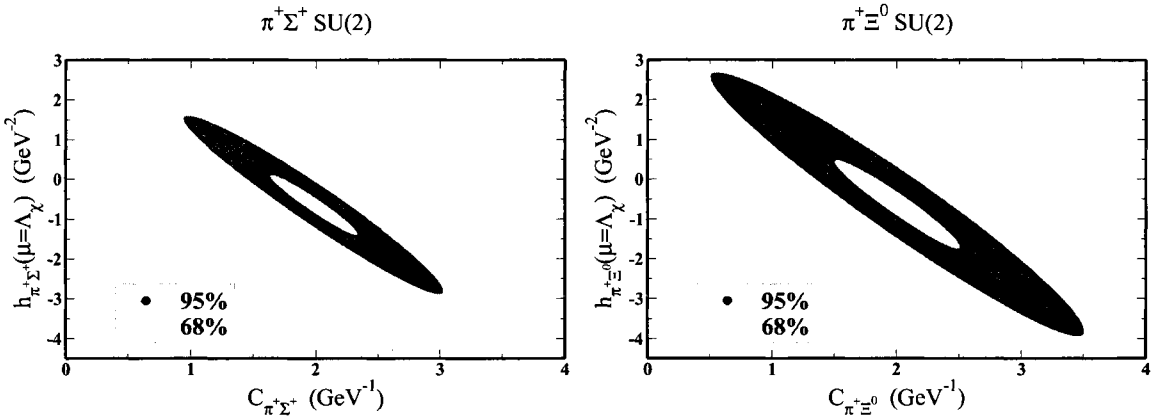

Figure 3-10: The 68% (light) and 95% (dark) confidence interval error ellipses for fits for the $\pi^+\Sigma^+$ (left), and $\pi^+\Xi^0$ (right) processes using Eqs. (3.40) and (3.41).

	NLO fit	NNLO fit
$C_{\pi^+\Sigma^+}$	1.28(09)(11) GeV^{-1}	1.90(10)(17) GeV^{-1}
$C_{\pi^+\Xi^0}$	1.84(23)(25) GeV^{-1}	1.93(12)(48) GeV^{-1}
$h'_{\pi^+\Sigma^+}$	-	-1.33(21)(26) GeV^{-2}
$h_{\pi^+\Xi^0}$	-	-1.36(27)(75) GeV^{-2}

Table 3.8: $SU(2)$ LECs fit from each process at NLO and at NNLO. The first uncertainty in parentheses is statistical, and the second is the statistical and systematic uncertainty added in quadrature.

the h-C plane for both $\pi^+\Sigma^+$ and $\pi^+\Xi^0$. Exploring the full 95% confidence interval error ellipse in the h-C plane yields

$$a_{\pi^+\Sigma^+} = -0.197 \pm 0.011 \text{ fm} ; \tag{3.49}$$

$$a_{\pi^+\Xi^0} = -0.102 \pm 0.004 \text{ fm} . \tag{3.50}$$

Comparison of these determinations with those of Eq. (3.46) give an estimate of the systematic error due to truncation of the chiral expansion at order m_π^3.

In order to plot the scattering length versus m_π, we define

$$\overline{a}_{\pi^+\Sigma^+} = a_{\pi^+\Sigma^+}\left(\frac{m_\pi + m_\Sigma}{m_\Sigma}\right) = \frac{1}{2\pi}\left(-\frac{m_\pi}{f^2} + \frac{m_\pi^2}{f^2}\mathrm{C}_{\pi^+\Sigma^+} + \frac{m_\pi^3}{f^2}h'_{\pi^+\Sigma^+}\right) ; \tag{3.51}$$

$$\overline{a}_{\pi^+\Xi^0} = a_{\pi^+\Xi^0}\left(\frac{m_\pi + m_\Xi}{m_\Xi}\right) = \frac{1}{4\pi}\left(-\frac{m_\pi}{f^2} + \frac{m_\pi^2}{f^2}\mathrm{C}_{\pi^+\Xi^0} + \frac{m_\pi^3}{f^2}h'_{\pi^+\Xi^0}\right) . \tag{3.52}$$

Quantity	LO (fm)	NLO (fm)	NLO (NNLO fit) (fm)	NNLO (fm)
$a_{\pi\Sigma}$	-0.2294	-0.212(03)(04)	-0.190(04)(06)	-0.197(04)(09)
$a_{\pi\Xi}$	-0.1158	-0.106(04)(05)	-0.095(02)(09)	-0.102(02)(09)

Table 3.9: $SU(2)$ extrapolated scattering lengths using the LECs from Table 3.8. The first uncertainty in parentheses is statistical, and the second is the statistical and systematic uncertainty added in quadrature.

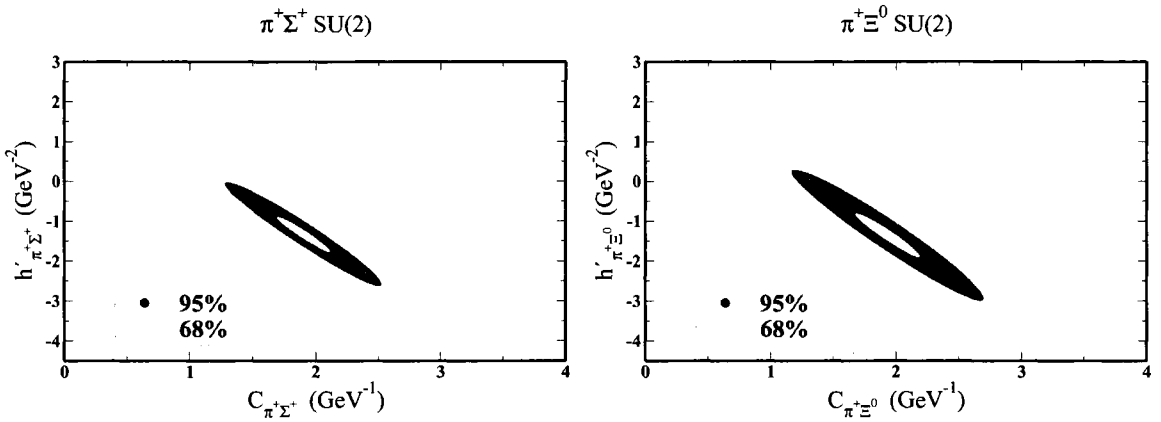

Figure 3-11: The 68% (light) and 95% (dark) confidence interval error ellipses for fits for the $\pi^+\Sigma^+$ (left), and $\pi^+\Xi^0$ (right) processes using Eqs. (3.47) and (3.48).

In Fig. 3-12 the scattering lengths are plotted versus the pion mass. The shaded bands in these plots correspond to the standard error in the determination of the LECs, as given in Table 3.8.

Additional systematic errors arising from the specific lattice formulation that employed are discussed in detail in Ref. [2], and are expected to be well encompassed by our error bars. As discussed in section 3.4.3, there is a systematic error in extracting the scattering length from the phase shift. The range corrections affect the scattering length at the 5% level for $\pi^+\Sigma^+$, and at the 1% level for $\pi^+\Xi^0$. Finally, there are unquantified systematic errors due to finite-volume and lattice-spacing effects, however, these errors are likely encompassed by our quoted errors.

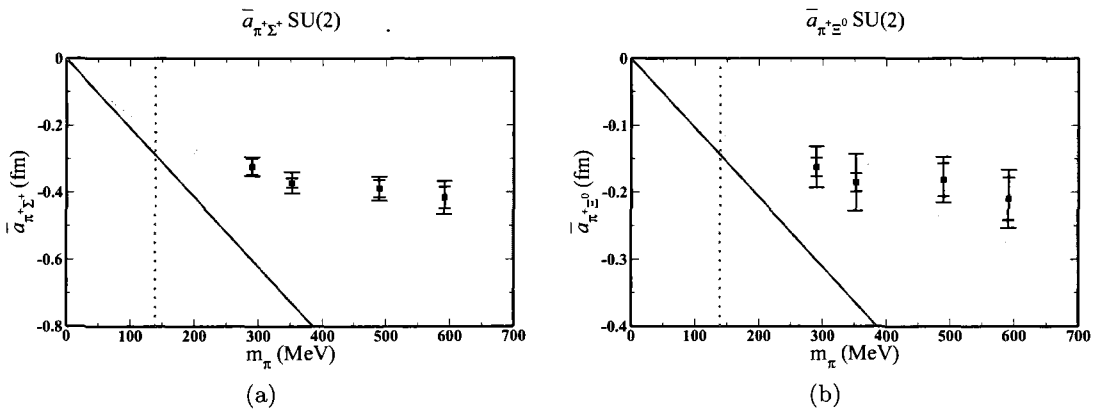

Figure 3-12: $\bar{a}$ plots for the $\pi^+\Sigma^+$, and $\pi^+\Xi^0$ processes versus the pion mass. The diagonal line is the leading order curve, and the dotted line is the physical pion mass. The innermost error bar is the statistical uncertainty and the outermost error bar is the statistical and systematic uncertainty added in quadrature. The filled bands are the fits to the LECs in the SU(2) case at NNLO as in Eqs. (3.51), and (3.52).

3.4.8 Discussion of Results

This study is the first fully-dynamical lattice QCD calculation of meson-baryon scattering. While the phenomenologically most-interesting case of pion-nucleon scattering involves annihilation diagrams, and therefore, requires more resources than those currently have available, the ground-state energies of $\pi^+\Sigma^+$, $\pi^+\Xi^0$, K^+p, K^+n, and $\overline{K}^0\Xi^0$ were calculated, and involve no annihilation diagrams.

The scattering lengths of these two-body systems using HBχPT leads to the conclusion that the three-flavor chiral expansion does not converge over the range of light quark masses used in the calculation. While the kaon-baryon scattering lengths appear perturbative at NLO, a comparison of NNLO with NLO calls into question the convergence of the three-flavor chiral expansion. Therefore, the values for the kaon-baryon scattering lengths at the physical point are not quoted. On the other hand, the $\pi^+\Sigma^+$ and $\pi^+\Xi^0$ scattering lengths appear to have a well-controlled chiral expansion in two-flavor HBχPT. Our results, $a_{\pi^+\Sigma^+} = -0.197 \pm 0.017$ fm, and $a_{\pi^+\Xi^0} = -0.098 \pm 0.017$ fm, deviate from the LO (current algebra) predictions at the one- and two-sigma level, respectively. Hopefully, there will be future experimental data to compare with this calculation.

Regarding the lowest-lying baryon decuplet, which is not considered in this work, one interesting process for future study is the $\pi^-\Omega^-$ system. It does not involve disconnected diagrams since the pions have no valence quarks with the same flavor as the Ω^- constituents. It has been argued that there is a bound state [113] in this channel, and therefore, it would be of interest to determine whether this state appears bound on the lattice at the available quark masses.

CONCLUSION

Calculations of hadron-hadron and multi-hadron scattering states using fully-dynamical Lattice QCD have yielded results for $\pi\pi$, KK, multi-meson, and meson-baryon interactions with physical predictions. Now multi-baryon interactions at one quark mass have been calculated as well [55]. Many of these calculations exist in large part due to the freely available MILC gauge configurations, as outlined in Tab. 2.1.

Calculations of the scattering lengths for the $\pi^+\pi^+$, and K^+K^+ mesonic systems have been presented. Also, the $N = 3$ to $N = 12$ pionic states, and the calculation of the ground-state energies of the $\pi^+\Sigma^+$, $\pi^+\Xi^0$, K^+p, K^+n, and $\overline{K}^0\Xi^0$, with extrapolation of the $\pi^+\Sigma^+$, $\pi^+\Xi^0$ scattering lengths have been discussed in this dissertation. The main result of my research work is the extraction of the $\pi^+\Sigma^+$and $\pi^+\Xi^0$scattering lengths using $SU(2)$ χ-PT. This result at the 95% confidence level is

$$a_{\pi^+\Sigma^+} = -0.197 \pm 0.017 \text{ fm} ; \tag{3.53}$$

$$a_{\pi^+\Xi^0} = -0.098 \pm 0.017 \text{ fm} . \tag{3.54}$$

Additionally, the $\overline{K}^0\Sigma^+$energy levels were calculated, but as detailed in 3.4.5, the scattering length for this channel is not calculated due to the fact that it is a mixed-channel.

An unexpected consequence of the meson-baryon calculations is that the convergence in the three-flavor chiral expansion, at least for the processes studied here, illustrates an interesting dichotomy. As the pion masses considered in this lattice calculation are comparable to the physical kaon mass, the distinct convergence patterns of the two- and three-flavor chiral expansions found in this work are suggestive that the breakdown in the three-flavor case is not due to the relative largeness of the strange-quark mass as compared to the light

quark masses, but rather due to some other enhancement in the coefficients of the loop contributions, possibly related to a scaling with powers of n_f, the number of flavors.

The use of both SS and SP correlators to extract the ground state energies with greater confidence due to the suppression of an excited state as was discussed in Sec. 2.2.3 came about during the meson-baryon analysis. Since the analysis was performed with the coarse MILC ensembles, the available time slices for signal extraction are limited, so the suppression of the first excited state gains early time slices for fitting, and the plateaus on the effective plots are more apparent. Without this method, the signal extraction is more ambiguous, due to the fact that the s/n ratio has usually degraded significantly by the time the effective mass plot starts to show a plateau.

A large part of the research work discussed in this dissertation was dependent on improving the signal extraction which is part of the greater signal to noise issue confronting LQCD calculations. Recently, the NPLQCD collaboration showed that this problem may not be as dire as was previously thought [55]. However, the extraction of excited states remains a challenge both in the mesonic and baryonic sectors, and it is possible that LQCD may profit from the application of Digital Signal Processing, for instance as is discussed in Sec. 2.2.2. Additionally, in Sec. 2.2.2 the application of a naive first-order digital filter seems to yield compelling results when looking at the effective mass plots of Fig. 2-2. This is something that could be studied systematically to determine if it in fact improves extraction of the ground state, or if in fact the systematic error introduced is large.

Given that computing power density is still growing, a logical continuation of the meson baryon calculations discussed here would be pion-nucleon scattering calculation. Much greater resources are required for this calculation, but there is much experimental data for πn scattering, so it would interesting to see if LQCD could benchmark the πn scattering lengths in the near future.

LIST OF REFERENCES

[1] Robert G. Edwards and Balint Joo. The Chroma software system for lattice QCD. *Nucl. Phys. Proc. Suppl.*, 140:832, 2005.

[2] Silas R. Beane et al. Precise Determination of the I=2 pipi Scattering Length from Mixed-Action Lattice QCD. *Phys. Rev.*, D77:014505, 2008.

[3] S. Pislak et al. High statistics measurement of Ke4 decay properties. *Phys. Rev.*, D67:072004, 2003.

[4] Silas R. Beane, Paulo F. Bedaque, Kostas Orginos, and Martin J. Savage. I = 2 pi pi scattering from fully-dynamical mixed-action lattice QCD. *Phys. Rev.*, D73:054503, 2006.

[5] C. Aubin et al. Light pseudoscalar decay constants, quark masses, and low energy constants from three-flavor lattice QCD. *Phys. Rev.*, D70:114501, 2004.

[6] C. Bernard et al. Update on the physics of light pseudoscalar mesons. *PoS*, LAT2006:163, 2006.

[7] G. Colangelo, J. Gasser, and H. Leutwyler. pi pi scattering. *Nucl. Phys.*, B603:125–179, 2001.

[8] T. Yamazaki et al. I = 2 pi pi scattering phase shift with two flavors of O(a) improved dynamical quarks. *Phys. Rev.*, D70:074513, 2004.

[9] Kenneth G. Wilson. CONFINEMENT OF QUARKS. *Phys. Rev.*, D10:2445–2459, 1974.

[10] Michael Creutz. The early days of lattice gauge theory. *AIP Conf. Proc.*, 690:52–60, 2003.

[11] L. Maiani and M. Testa. Final state interactions from Euclidean correlation functions. *Phys. Lett.*, B245:585–590, 1990.

[12] A. Bazavov et al. Full nonperturbative QCD simulations with 2+1 flavors of improved staggered quarks. 2009.

[13] H. Georgi. WEAK INTERACTIONS AND MODERN PARTICLE THEORY. Menlo Park, Usa: Benjamin/cummings (1984) 165p.

[14] Thomas DeGrand and Carleton E. Detar. Lattice methods for quantum chromodynamics. New Jersey, USA: World Scientific (2006) 345 p.

[15] John B. Kogut and Leonard Susskind. Hamiltonian Formulation of Wilson's Lattice Gauge Theories. *Phys. Rev.*, D11:395, 1975.

[16] Tom Banks, Leonard Susskind, and John B. Kogut. Strong Coupling Calculations of Lattice Gauge Theories: (1+1)-Dimensional Exercises. *Phys. Rev.*, D13:1043, 1976.

[17] Tom Banks et al. Strong Coupling Calculations of the Hadron Spectrum of Quantum Chromodynamics. *Phys. Rev.*, D15:1111, 1977.

[18] Leonard Susskind. Lattice Fermions. *Phys. Rev.*, D16:3031–3039, 1977.

[19] Stephan Durr and Christian Hoelbling. Scaling tests with dynamical overlap and rooted staggered fermions. *Phys. Rev.*, D71:054501, 2005.

[20] Michael Creutz. Flavor extrapolations and staggered fermions. 2006.

[21] Claude Bernard, Maarten Golterman, Yigal Shamir, and Stephen R. Sharpe. Comment on 'Chiral anomalies and rooted staggered fermions'. *Phys. Lett.*, B649:235–240, 2007.

[22] Stephan Durr and Christian Hoelbling. Lattice fermions with complex mass. *Phys. Rev.*, D74:014513, 2006.

[23] Anna Hasenfratz and Roland Hoffmann. Validity of the rooted staggered determinant in the continuum limit. *Phys. Rev.*, D74:014511, 2006.

[24] Claude Bernard, Maarten Golterman, and Yigal Shamir. Observations on staggered fermions at non-zero lattice spacing. *Phys. Rev.*, D73:114511, 2006.

[25] Yigal Shamir. Renormalization-group analysis of the validity of staggered-fermion QCD with the fourth-root recipe. *Phys. Rev.*, D75:054503, 2007.

[26] Stephen R. Sharpe. Rooted staggered fermions: Good, bad or ugly? *PoS*, LAT2006:022, 2006.

[27] Yigal Shamir. Chiral fermions from lattice boundaries. *Nucl. Phys.*, B406:90–106, 1993.

[28] Vadim Furman and Yigal Shamir. Axial symmetries in lattice QCD with Kaplan fermions. *Nucl. Phys.*, B439:54–78, 1995.

[29] Silas R. Beane, Kostas Orginos, and Martin J. Savage. Hadronic Interactions from Lattice QCD. *Int. J. Mod. Phys.*, E17:1157–1218, 2008.

[30] Anna Hasenfratz and Francesco Knechtli. Flavor symmetry and the static potential with hypercubic blocking. *Phys. Rev.*, D64:034504, 2001.

[31] Thomas A. DeGrand, Anna Hasenfratz, and Tamas G. Kovacs. Improving the chiral properties of lattice fermions. *Phys. Rev.*, D67:054501, 2003.

[32] Thomas A. DeGrand. Kaon B Parameter in Quenched QCD. *Phys. Rev.*, D69:014504, 2004.

[33] Stephan Durr, Christian Hoelbling, and Urs Wenger. Staggered eigenvalue mimicry. *Phys. Rev.*, D70:094502, 2004.

[34] Kostas Orginos, Doug Toussaint, and R. L. Sugar. Variants of fattening and flavor symmetry restoration. *Phys. Rev.*, D60:054503, 1999.

[35] Kostas Orginos and Doug Toussaint. Testing improved actions for dynamical Kogut-Susskind quarks. *Phys. Rev.*, D59:014501, 1999.

[36] D. Toussaint and K. Orginos. Tests of improved Kogut-Susskind fermion actions. *Nucl. Phys. Proc. Suppl.*, 73:909–911, 1999.

[37] K. Orginos, R. Sugar, and D. Toussaint. Improved flavor symmetry in Kogut-Susskind fermion actions. *Nucl. Phys. Proc. Suppl.*, 83:878–880, 2000.

[38] Weon-Jong Lee and Stephen R. Sharpe. Partial Flavor Symmetry Restoration for Chiral Staggered Fermions. *Phys. Rev.*, D60:114503, 1999.

[39] Dru Bryant Renner et al. Hadronic physics with domain-wall valence and improved staggered sea quarks. *Nucl. Phys. Proc. Suppl.*, 140:255–260, 2005.

[40] Robert G. Edwards et al. Hadron structure with light dynamical quarks. *PoS*, LAT2005:056, 2006.

[41] Robert Glenn Edwards et al. Hadron spectrum with domain-wall valence quarks on an improved staggered sea. *PoS*, LAT2006:195, 2006.

[42] Dru Bryant Renner et al. Generalized parton distributions from domain wall valence quarks and staggered sea quarks. *PoS*, LAT2007:160, 2007.

[43] Ph. Hagler et al. Nucleon Generalized Parton Distributions from Full Lattice QCD. *Phys. Rev.*, D77:094502, 2008.

[44] R. G. Edwards et al. Nucleon structure in the chiral regime with domain wall fermions on an improved staggered sea. *PoS*, LAT2006:121, 2006.

[45] Justin Foley et al. Practical all-to-all propagators for lattice QCD. *Comput. Phys. Commun.*, 172:145–162, 2005.

[46] Steven Weinberg. Phenomenological Lagrangians. *Physica*, A96:327, 1979.

[47] Stefan Scherer. Introduction to chiral perturbation theory. *Adv. Nucl. Phys.*, 27:277, 2003.

[48] Aneesh Manohar and Howard Georgi. Chiral Quarks and the Nonrelativistic Quark Model. *Nucl. Phys.*, B234:189, 1984.

[49] Aaron Torok et al. Meson-Baryon Scattering Lengths from Mixed-Action Lattice QCD. 2009.

[50] Kerson Huang and C. N. Yang. Quantum-mechanical many-body problem with hard-sphere interaction. *Phys. Rev.*, 105:767–775, 1957.

[51] M. Luscher. Volume Dependence of the Energy Spectrum in Massive Quantum Field Theories. 2. Scattering States. *Commun. Math. Phys.*, 105:153–188, 1986.

[52] Martin Luscher. Two particle states on a torus and their relation to the scattering matrix. *Nucl. Phys.*, B354:531–578, 1991.

[53] H. W. Hamber, E. Marinari, G. Parisi, and C. Rebbi. CONSIDERATIONS ON NUMERICAL ANALYSIS OF QCD. *Nucl. Phys.*, B225:475, 1983.

[54] S. R. Beane, P. F. Bedaque, A. Parreno, and M. J. Savage. Two Nucleons on a Lattice. *Phys. Lett.*, B585:106–114, 2004.

[55] Silas R. Beane et al. High Statistics Analysis using Anisotropic Clover Lattices: (I) Single Hadron Correlation Functions. 2009.

[56] John Bulava et al. Hadronic Resonances from Lattice QCD. *AIP Conf. Proc.*, 947:77–84, 2007.

[57] J. Bulava, R. Edwards, K. J. Juge, C. J. Morningstar, and M. J. Peardon. Multi-hadron operators with all-to-all quark propagators. 2008.

[58] Z. D. Popovic. Application of digital filtering to noise reduction in exponential decays. *Journal of Physics E Scientific Instruments*, 19:914–916, November 1986.

[59] Silas R. Beane et al. High Statistics Analysis using Anisotropic Clover Lattices: (II) Three-Baryon Systems. 2009.

[60] Germund Dahlquist and Åke Björck. *Numerical methods.* 2003.

[61] Steven Weinberg. Pion scattering lengths. *Phys. Rev. Lett.*, 17:616–621, 1966.

[62] Jiunn-Wei Chen, Donal O'Connell, Ruth S. Van de Water, and Andre Walker-Loud. Ginsparg-Wilson pions scattering on a staggered sea. *Phys. Rev.*, D73:074510, 2006.

[63] Jiunn-Wei Chen, Donal O'Connell, and Andre Walker-Loud. Two meson systems with Ginsparg-Wilson valence quarks. *Phys. Rev.*, D75:054501, 2007.

[64] S. M. Roy. Exact integral equation for pion pion scattering involving only physical region partial waves. *Phys. Lett.*, B36:353, 1971.

[65] J. L. Basdevant, C. D. Froggatt, and J. L. Petersen. Construction of Phenomenological pi pi Amplitudes. *Nucl. Phys.*, B72:413, 1974.

[66] B. Ananthanarayan, G. Colangelo, J. Gasser, and H. Leutwyler. Roy equation analysis of pi pi scattering. *Phys. Rept.*, 353:207–279, 2001.

[67] Silas R. Beane et al. The K+K+ Scattering Length from Lattice QCD. *Phys. Rev.*, D77:094507, 2008.

[68] Kostas Orginos and Andre Walker-Loud. Mixed meson masses with domain-wall valence and staggered sea fermions. *Phys. Rev.*, D77:094505, 2008.

[69] Silas R. Beane, William Detmold, and Martin J. Savage. n-Boson Energies at Finite Volume and Three-Boson Interactions. *Phys. Rev.*, D76:074507, 2007.

[70] William Detmold and Martin J. Savage. The Energy of n Identical Bosons in a Finite Volume at $O(L^{-7})$. *Phys. Rev.*, D77:057502, 2008.

[71] Shina Tan. Three-boson problem at low energy and Implications for dilute Bose-Einstein condensates. 2007.

[72] N. N. Bogoliubov. *J. Phys. (Moscow)*, 11:23, 1947.

[73] T. D. Lee, K. Huang, and C. N. Yang. *Phys. Rev.*, 106:1135, 1957.

[74] David H. Bailey. High-precision floating-point arithmetic in scientific computation. *Computing in Science and Engineering*, 7(3):54–61, 2005.

[75] Silas R. Beane et al. Pi-K Scattering in Full QCD with Domain-Wall Valence Quarks. *Phys. Rev.*, D74:114503, 2006.

[76] Veronique Bernard. Chiral Perturbation Theory and Baryon Properties. *Prog. Part. Nucl. Phys.*, 60:82–160, 2008.

[77] S. R. Beane, P. F. Bedaque, K. Orginos, and M. J. Savage. Nucleon nucleon scattering from fully-dynamical lattice QCD. *Phys. Rev. Lett.*, 97:012001, 2006.

[78] Silas R. Beane et al. Hyperon nucleon scattering from fully-dynamical lattice QCD. *Nucl. Phys.*, A794:62–72, 2007.

[79] G. Peter Lepage. THE ANALYSIS OF ALGORITHMS FOR LATTICE FIELD THEORY. Invited lectures given at TASI'89 Summer School, Boulder, CO, Jun 4-30, 1989.

[80] David B. Kaplan, Martin J. Savage, and Mark B. Wise. Two-nucleon systems from effective field theory. *Nucl. Phys.*, B534:329–355, 1998.

[81] Ronald Babich et al. Strange quark content of the nucleon. *PoS*, LATTICE2008:160, 2008.

[82] Elizabeth Ellen Jenkins and Aneesh V. Manohar. Baryon chiral perturbation theory using a heavy fermion Lagrangian. *Phys. Lett.*, B255:558–562, 1991.

[83] Yan-Rui Liu and Shi-Lin Zhu. Meson-baryon scattering lengths in HBχPT. *Phys. Rev.*, D75:034003, 2007.

[84] Yan-Rui Liu and Shi-Lin Zhu. Decuplet contribution to the meson baryon scattering lengths. *Eur. Phys. J.*, C52:177–186, 2007.

[85] Norbert Kaiser. Chiral corrections to kaon nucleon scattering lengths. *Phys. Rev.*, C64:045204, 2001.

[86] Maxim Mai, Peter C. Bruns, Bastian Kubis, and Ulf-G. Meissner. Aspects of meson-baryon scattering in three- and two- flavor chiral perturbation theory. 2009.

[87] D. B. Kaplan and A. E. Nelson. KAON CONDENSATION IN DENSE NUCLEONIC MATTER. HUTP-86/A023.

[88] D. B. Kaplan and A. E. Nelson. Strange Goings on in Dense Nucleonic Matter. *Phys. Lett.*, B175:57–63, 1986.

[89] Ann E. Nelson and David B. Kaplan. Strange Condensate Realignment in Relativistic Heavy Ion Collisions. *Phys. Lett.*, B192:193, 1987.

[90] D. B. Kaplan and A. E. Nelson. KAON CONDENSATION IN DENSE MATTER. *Nucl. Phys.*, A479:273, 1988.

[91] A. E. Nelson and D. B. Kaplan. KAON CONDENSATION IN HEAVY ION COLLISIONS. *Nucl. Phys.*, A479:285, 1988.

[92] Ming Lu, Mark B. Wise, and Martin J. Savage. Strong Lambda pi phase shifts for CP violation in weak Xi $\rightarrow$ Lambda pi decay. *Phys. Lett.*, B337:133–136, 1994.

[93] H. C. Schroder et al. Determination of the pi N scattering lengths from pionic hydrogen. *Phys. Lett.*, B469:25–29, 1999.

[94] H. C. Schroder et al. The pion nucleon scattering lengths from pionic hydrogen and deuterium. *Eur. Phys. J.*, C21:473–488, 2001.

[95] Alan D. Martin. Kaon - Nucleon Parameters. *Nucl. Phys.*, B179:33, 1981.

[96] M. Fukugita, Y. Kuramashi, M. Okawa, H. Mino, and A. Ukawa. Hadron scattering lengths in lattice QCD. *Phys. Rev.*, D52:3003–3023, 1995.

[97] Guang-wei Meng, Chuan Miao, Xi-ning Du, and Chuan Liu. Lattice study on kaon nucleon scattering length in the I = 1 channel. *Int. J. Mod. Phys.*, A19:4401–4412, 2004.

[98] Brian C. Tiburzi. Baryons with Ginsparg-Wilson quarks in a staggered sea. *Phys. Rev.*, D72:094501, 2005.

[99] Jiunn-Wei Chen, Donal O'Connell, and Andre Walker-Loud. Universality of Mixed Action Extrapolation Formulae. *JHEP*, 04:090, 2009.

[100] David B. Kaplan. A Method for simulating chiral fermions on the lattice. *Phys. Lett.*, B288:342–347, 1992.

[101] Yigal Shamir. The Euclidean spectrum of Kaplan's lattice chiral fermions. *Phys. Lett.*, B305:357–365, 1993.

[102] Yigal Shamir. Reducing chiral symmetry violations in lattice QCD with domain-wall fermions. *Phys. Rev.*, D59:054506, 1999.

[103] Claude W. Bernard et al. The QCD spectrum with three quark flavors. *Phys. Rev.*, D64:054506, 2001.

[104] C. Bernard. Staggered chiral perturbation theory and the fourth-root trick. *Phys. Rev.*, D73:114503, 2006.

[105] Michael Creutz. The author replies. (Chiral anomalies and rooted staggered fermions). *Phys. Lett.*, B649:241–242, 2007.

[106] Claude Bernard, Maarten Golterman, and Yigal Shamir. Regularizing QCD with staggered fermions and the fourth root trick. *PoS*, LAT2006:205, 2006.

[107] Michael Creutz. The evil that is rooting. *Phys. Lett.*, B649:230–234, 2007.

[108] Christopher Michael. Adjoint Sources in Lattice Gauge Theory. *Nucl. Phys.*, B259:58, 1985.

[109] Martin Luscher and Ulli Wolff. HOW TO CALCULATE THE ELASTIC SCATTERING MATRIX IN TWO- DIMENSIONAL QUANTUM FIELD THEORIES BY NUMERICAL SIMULATION. *Nucl. Phys.*, B339:222–252, 1990.

[110] William Detmold and Martin J. Savage. Electroweak matrix elements in the two-nucleon sector from lattice QCD. *Nucl. Phys.*, A743:170–193, 2004.

[111] Song He, Xu Feng, and Chuan Liu. Two particle states and the S-matrix elements in multi- channel scattering. *JHEP*, 07:011, 2005.

[112] Huey-Wen Lin and Konstantinos Orginos. First Calculation of Hyperon Axial Couplings from Lattice QCD. *Phys. Rev.*, D79:034507, 2009.

[113] W. L. Wang, F. Huang, Z. Y. Zhang, Y. W. Yu, and F. Liu. A possible Omega pi molecular state. *Eur. Phys. J.*, A32:293–297, 2007.

Appendix A

EFFECTIVE PLOTS

The single particle effective mass plots and effective ΔE plots as described in Eq. 3.23 for the meson-baryon systems described in Sec. 3.4 are presented in this appendix for the MILC Ensembles (*i*)-(*iv*) of Table 2.1.

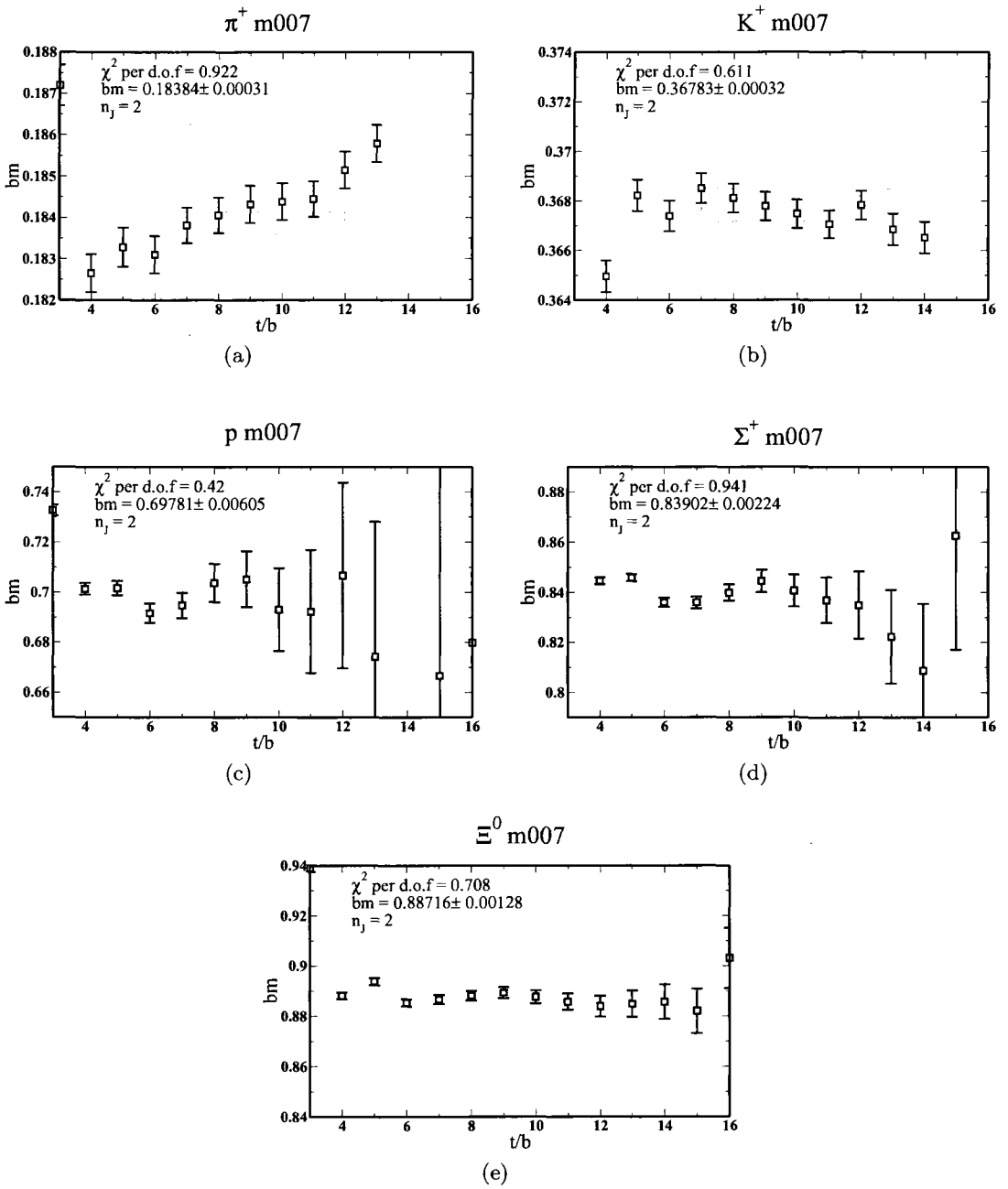

Figure A-1: Single particle effective mass plots for coarse MILC ensemble (i). Here, $n_J = 2$, and the linear combination $C^{(\mathrm{SS})} - \alpha C^{(\mathrm{SP})}$ is plotted. The inner shaded bands are the jackknife uncertainties of the fits to the effective masses, and the outer bands are the jackknife uncertainty and systematic uncertainty added in quadrature over the indicated window of time slices.

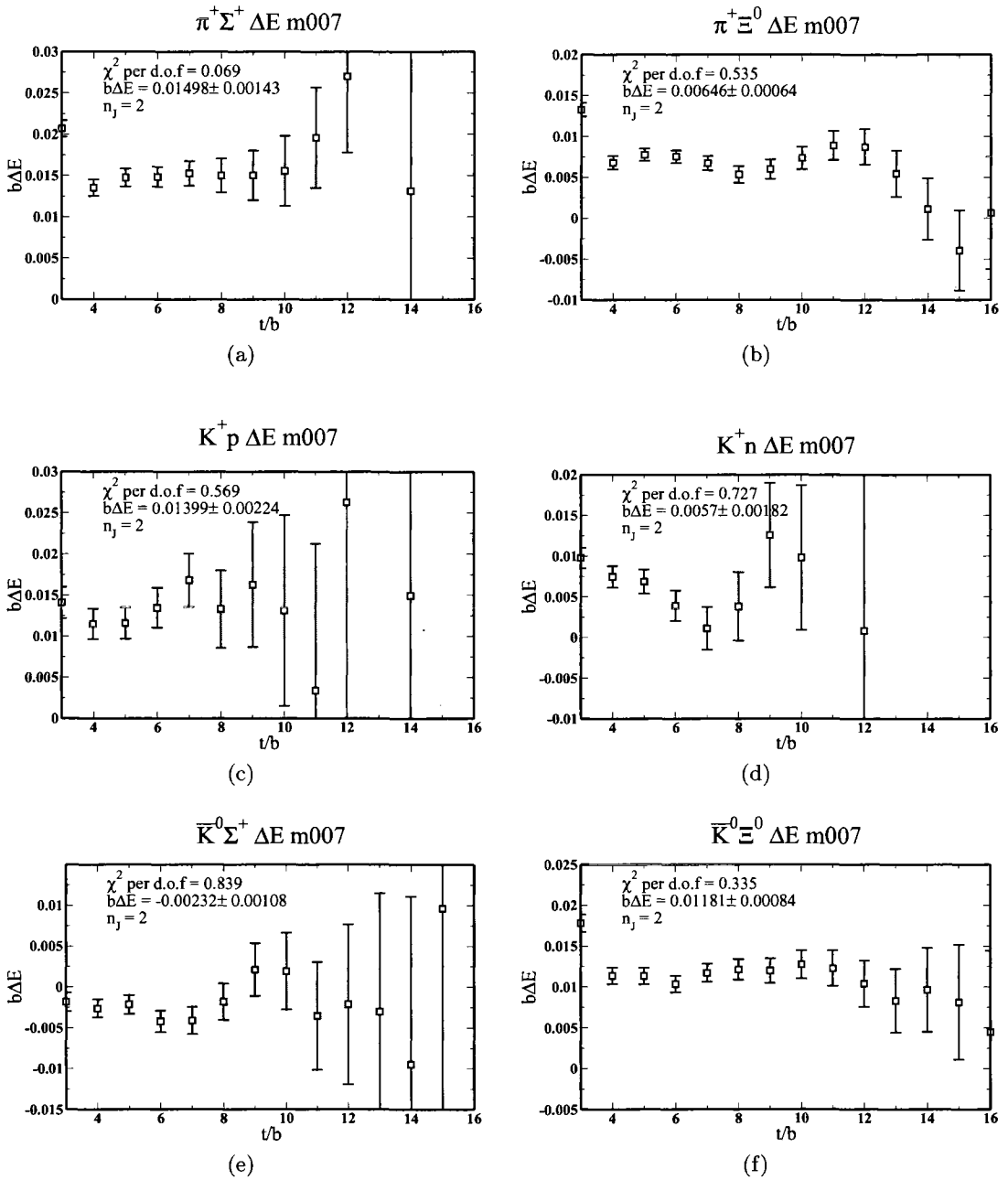

Figure A-2: Meson-baryon effective energy difference plots for coarse MILC ensemble (i). Here, $n_J = 2$, and the linear combination $C^{(\mathrm{SS})} - \alpha C^{(\mathrm{SP})}$ is plotted. The inner shaded bands are the jackknife uncertainties of the fits to the effective energy differences, and the outer bands are the jackknife uncertainty and systematic uncertainty added in quadrature over the indicated window of time slices.

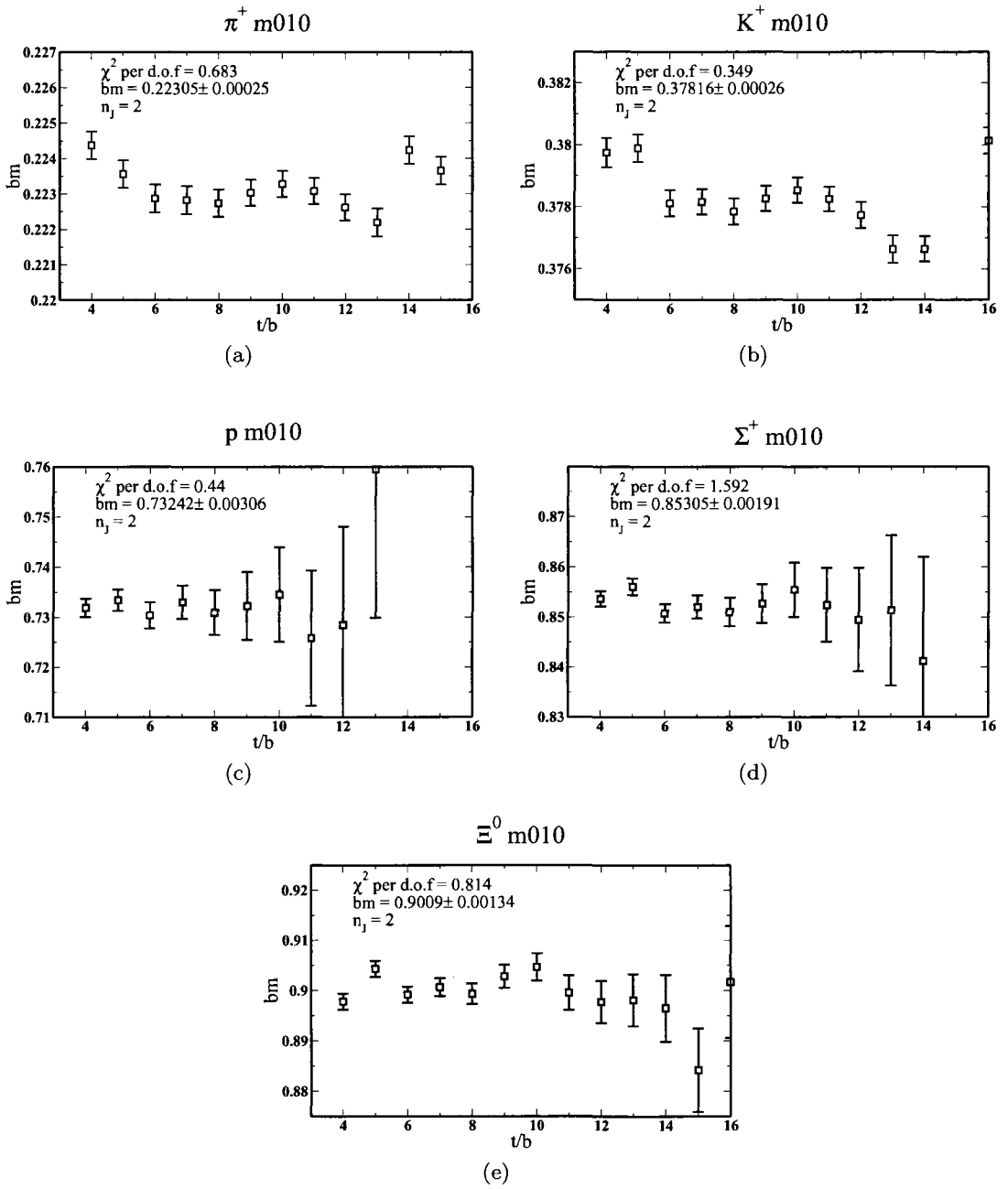

Figure A-3: Single particle effective mass plots for coarse MILC ensemble (*ii*). Here, $n_J = 2$, and the linear combination $C^{(\mathrm{SS})} - \alpha C^{(\mathrm{SP})}$ is plotted. The inner shaded bands are the jackknife uncertainties of the fits to the effective masses, and the outer bands are the jackknife uncertainty and systematic uncertainty added in quadrature over the indicated window of time slices.

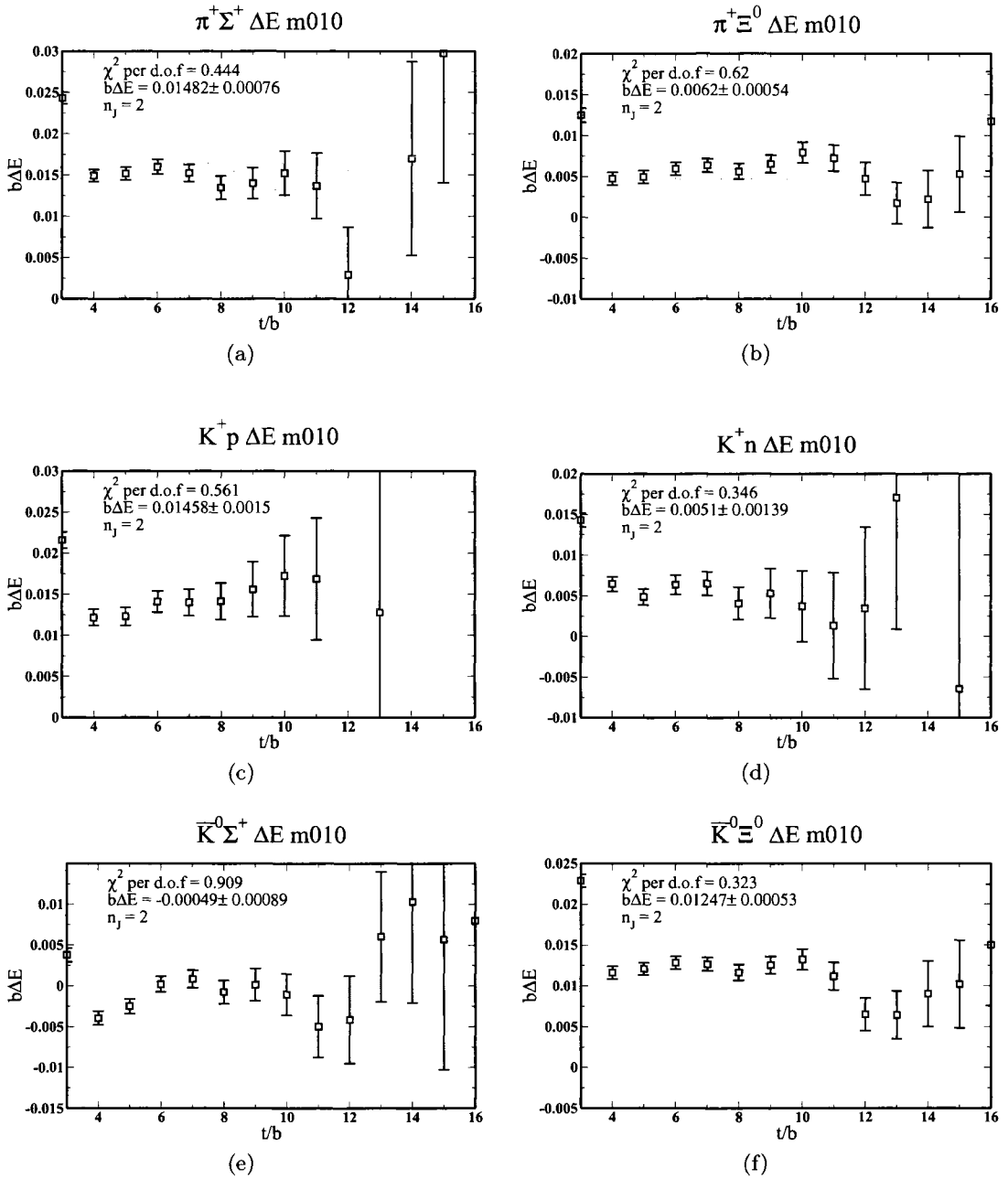

Figure A-4: Meson-baryon effective energy difference plots for coarse MILC ensemble (*ii*). Here, $n_J = 2$, and the linear combination $C^{(\mathrm{SS})} - \alpha C^{(\mathrm{SP})}$ is plotted. The inner shaded bands are the jackknife uncertainties of the fits to the effective energy differences, and the outer bands are the jackknife uncertainty and systematic uncertainty added in quadrature over the indicated window of time slices.

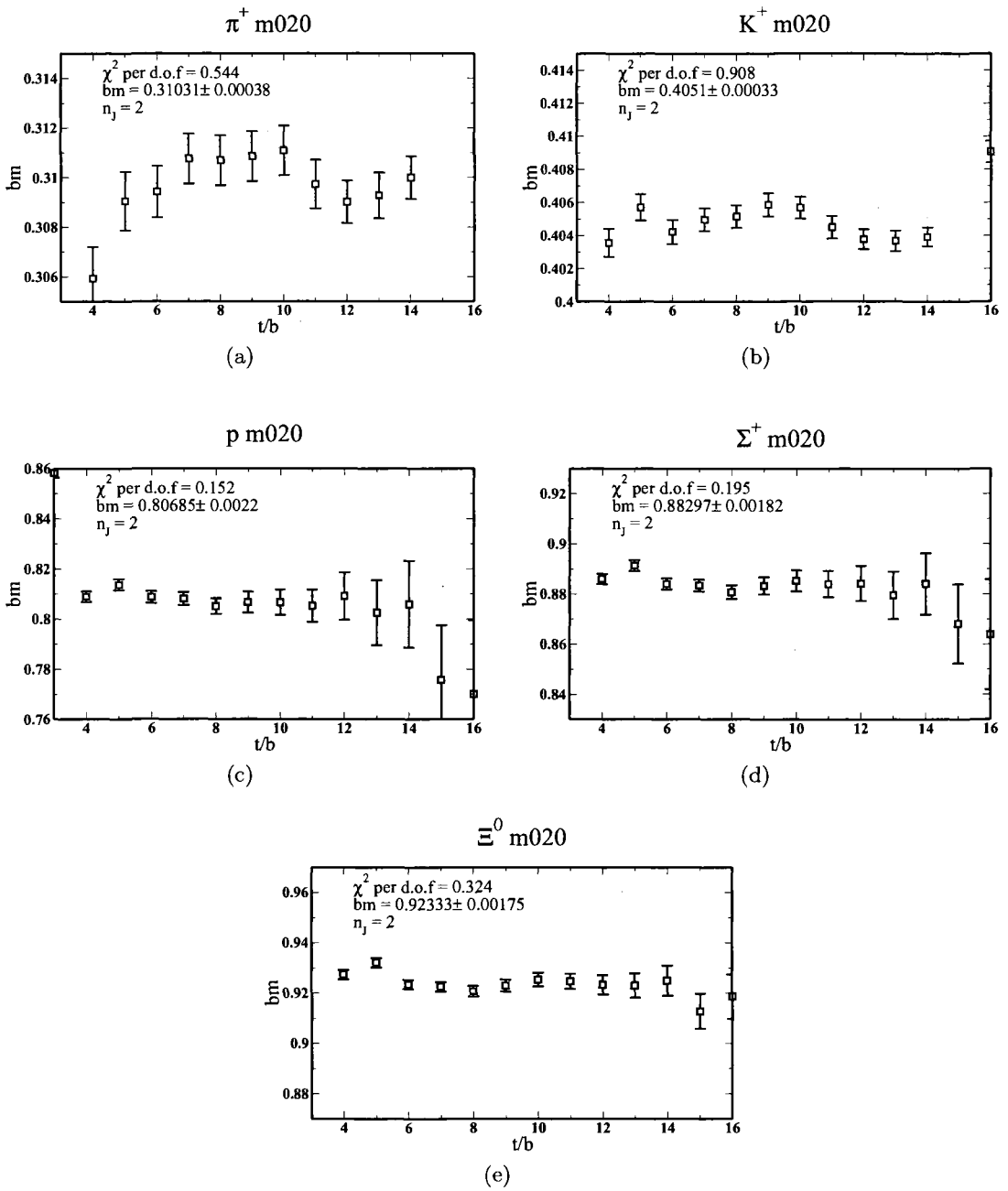

Figure A-5: Single particle effective mass plots for coarse MILC ensemble (*iii*). Here, $n_J = 2$, and the linear combination $C^{(\mathrm{SS})} - \alpha C^{(\mathrm{SP})}$ is plotted. The inner shaded bands are the jackknife uncertainties of the fits to the effective masses, and the outer bands are the jackknife uncertainty and systematic uncertainty added in quadrature over the indicated window of time slices.

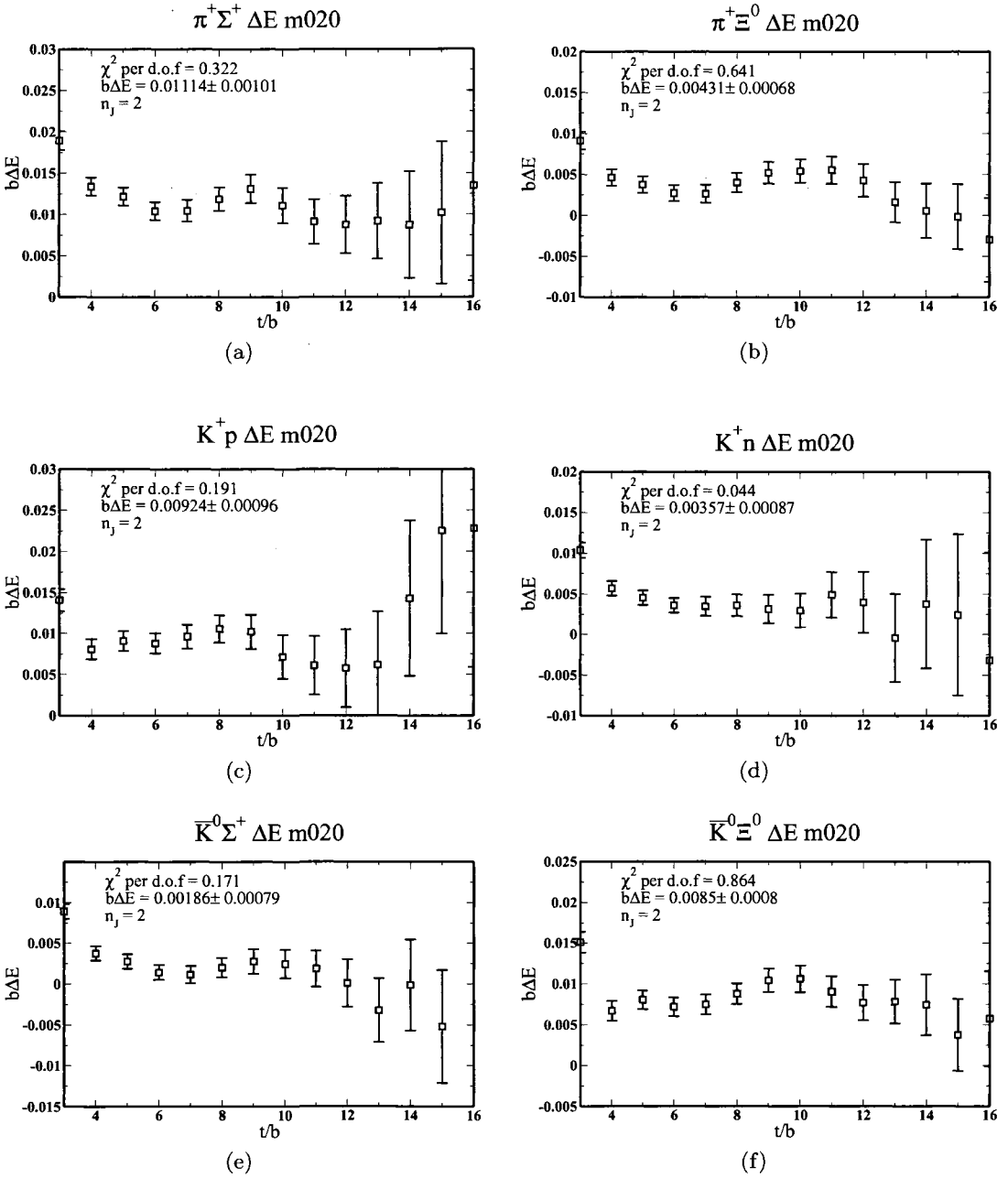

Figure A-6: Meson-baryon effective energy difference plots for coarse MILC ensemble (*iii*). Here, $n_J = 2$, and the linear combination $C^{(\mathrm{SS})} - \alpha C^{(\mathrm{SP})}$ is plotted. The inner shaded bands are the jackknife uncertainties of the fits to the effective energy differences, and the outer bands are the jackknife uncertainty and systematic uncertainty added in quadrature over the indicated window of time slices.

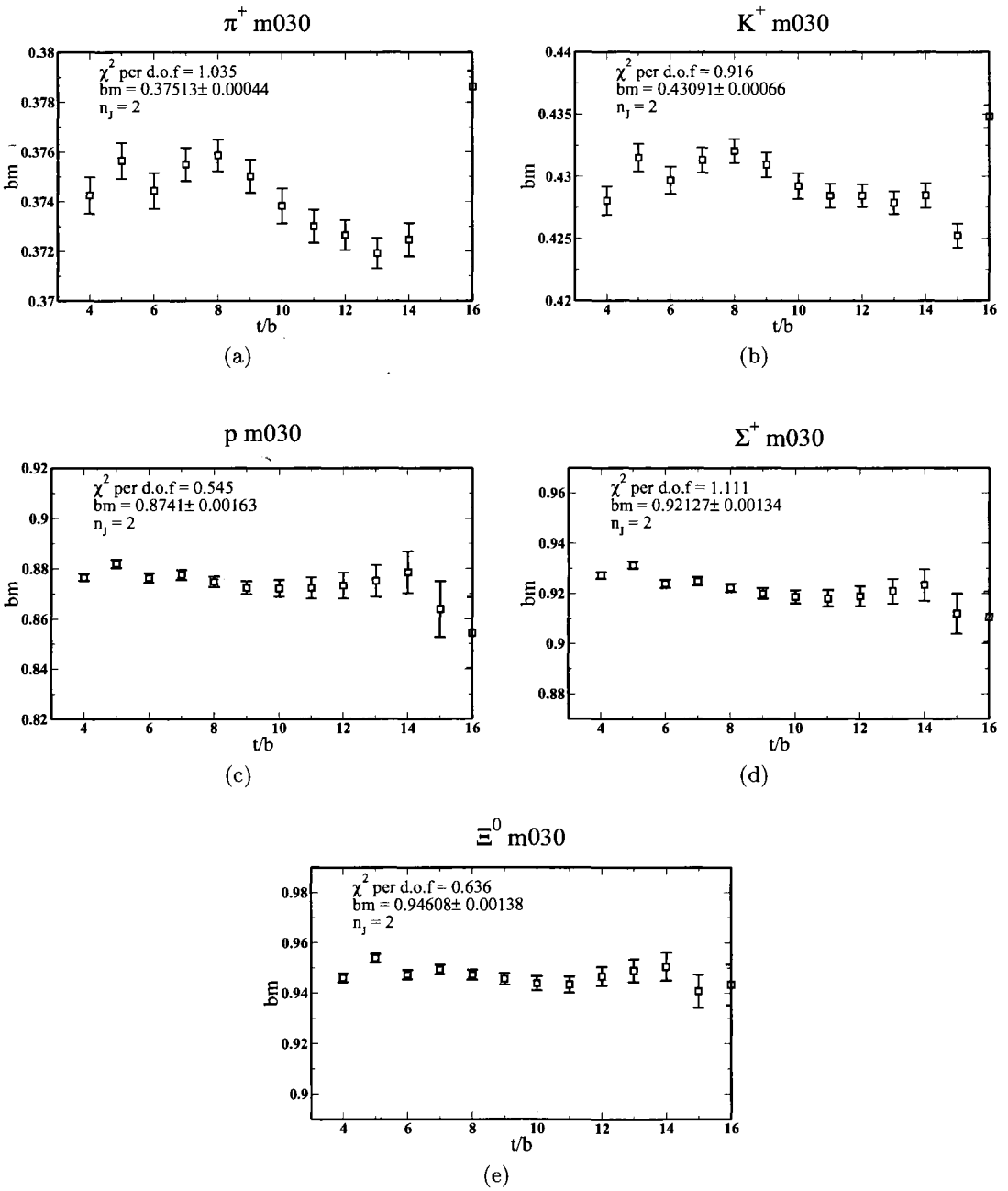

Figure A-7: Single particle effective mass plots for coarse MILC ensemble (*iv*). Here, $n_J = 2$, and the linear combination $C^{(\mathrm{SS})} - \alpha C^{(\mathrm{SP})}$ is plotted. The inner shaded bands are the jackknife uncertainties of the fits to the effective masses, and the outer bands are the jackknife uncertainty and systematic uncertainty added in quadrature over the indicated window of time slices.

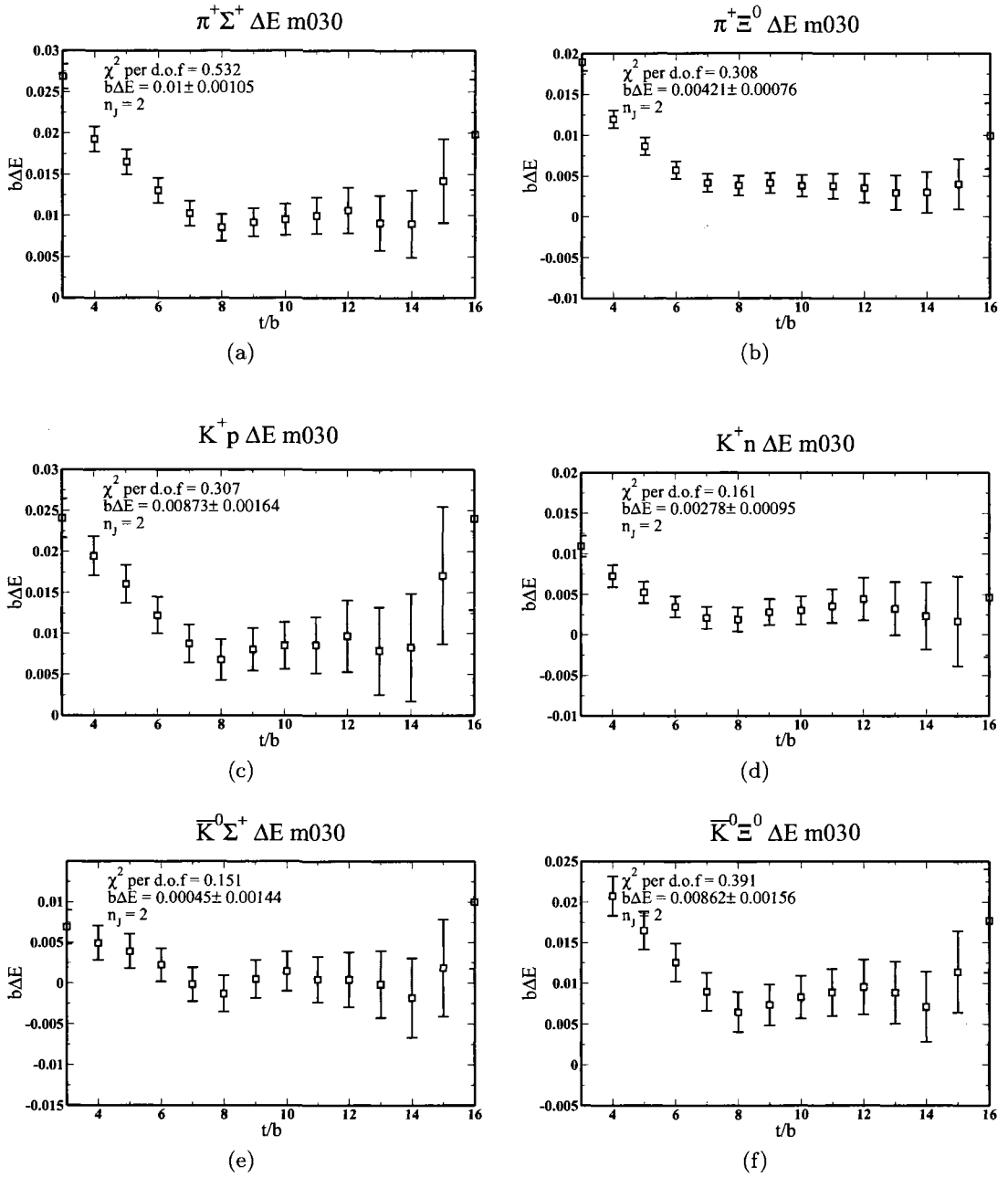

Figure A-8: Meson-baryon effective energy difference plots for coarse MILC ensemble (*iv*). Here, $n_J = 2$, and the linear combination $C^{(\mathrm{SS})} - \alpha C^{(\mathrm{SP})}$ is plotted. The inner shaded bands are the jackknife uncertainties of the fits to the effective energy differences, and the outer bands are the jackknife uncertainty and systematic uncertainty added in quadrature over the indicated window of time slices.